IMPERIAL COLLEGE LONDON

UNIVERSITY OF LONDON

TOWARDS HIGHER RESOLUTION GUIDED WAVE INSPECTION: SCATTERING STUDIES

by

Prabhu Rajagopal

A thesis submitted to the University of London for the degree of
Doctor of Philosophy

Department of Mechanical Engineering

Imperial College London

London SW7 2AZ

December 2007

Abstract

This thesis presents work contributing to the development of ultrasonic guided wave NDE inspection systems with improved resolution. Guided waves today are well established in the rapid inspection of large structures. The approach taken so far has been to develop screening tools to maximize coverage; the methods yield precise information about the exact location of defects but only an approximate estimate of the severity of defects. However there are many applications where the areas of concern are not accessible, and reaching them for a secondary accurate inspection may not be possible or involve considerable cost. Therefore there is much interest in improving the resolution of guided wave NDE towards direct defect sizing. Two possible approaches are being considered to achieve this, using either multiple modes at high frequency-thickness or single mode array imaging at low frequencies. The work reported here concerns the understanding of the interaction of guided waves with defects so that an appropriate approach can be selected and implemented. A review of the basics of elastic wave scattering from defects is first presented in order to introduce methods used and effects encountered later in the work.

A simple implementation of the high-frequency multimodal approach, in which the input consists of a single fundamental mode while the multiple-mode scattered signal permits separation into component modes, is then considered. Finite element simulations and theoretical analysis are used to study the interaction of the fundamental antisymmetric Lamb wave mode A0 and the fundamental torsional pipe mode T(0,1) with long but part-thickness planar cracks, in this context. The results show that the reflection due to both modes is more sensitive to shallow cracks than at lower frequencies. The reflected A0 and A1 modes in plates and T(0,1) mode in pipes emerge as the 'best modes' for discrimination between shallow and deep cracks since their amplitudes have a uniform relation with the crack depth. Also, knowledge of effects such as regions of little or no mode conversion and the extent to which the reflections of the different modes differ, emerge as powerful ways of obtaining useful additional information about defect dimensions.

In view of promising trends from parallel work at the Imperial College NDT Group using low-frequency array imaging methods, the rest of the thesis focuses on the interaction of cylindrical crested low-frequency SH0 waves with finite cracks in thin plates. Finite element simulations are used to obtained trends which are subject to experimental confirmation and analysis. Since guided SH waves in thin plates correspond to torsional modes in pipes, the results obtained help clarify the physics of scattering so that imaging methods may be better formulated and developed. The simpler case of through-thickness cracks is first taken up and the influence of the crack length, monitoring position and the angle of incidence on specular reflection as well as diffraction are studied. The insights obtained are then used to understand the scattering from the more general part-thickness crack case.

The through-thickness crack studies show that low-frequency scattering of the SH0 mode is strongly affected by diffraction phenomena, leading to focusing of energy by the crack in the backscattered direction. The diffracted field itself consists of components arising from primary diffraction from the crack tips (or edges) and multiple reverberations of Rayleigh-like waves traveling along the crack length. The amplitude of the primary diffraction can be estimated from known solutions to canonical bulk SV wave diffraction problems. The angular behaviour of the reflection is highly directional, with strongest fields in the specular direction, while the specular reflection itself is strongest when the central ray of the incident beam bisects the crack face at 90^0. The trend of the scattering as observed from part-thickness crack results is identical to that from through-thickness cracks of the same length; the actual values differ only by a frequency dependent scale factor, provided the cracks are small compared to the radius of the incident wavefront. Thus the understanding obtained for scattering from through-thickness cracks may well be sufficient to deal with the part-thickness case also.

From the guided wave imaging perspective, these results help obtain the far-field values for a given operating frequency-thickness and crack length. The directionality of the reflected field informs the possibilities for imaging, but imposes a limitation on the extent to which the resolution of inspection can be improved by low-frequency methods.

Acknowledgements

I would like to sincerely thank Professors Mike Lowe and Peter Cawley for their excellent guidance and supervision. Hearing me out when I was talking out of uninformed enthusiasm, encouraging me when I was stuck, pointing out the larger picture and patterns with my results, Prof. Lowe has been a constant source of support and inspiration. Invaluable insights from Prof. Cawley at crucial stages of the project helped me give form to this work and set limits.

Credit is due to the members of the NDT Group, for maintaining a great spirit of cooperation and organization. I deeply value what I also received from them: mentorship from seniors and the friendship of current students. I must mention Dr Jimmy Fong who I knew through my placement months in the Lab: in the difficult initial years particularly he was a great support; Dr Daniel Hesse who helped me get started on all sorts of software and patiently endured unending questions; Dr Frederic Cegla who helped me overcome my fear of experiments and Mr Ma Jian (Dr in a few weeks) who helped get started with them; Mr Mickael Drozdz who developed an absorbing boundary tool that helped me immensely in my simulations and Mr Naresh Juluri for lively and useful discussions.

Thanks to Dave Tomlin of the Mechanical Engineering workshop for timely and flawless preparation of my experimental samples.

Finally my thanks to my parents and my brother, who have been 'so far yet so near' through the many 'few months more'. And Sona, whose support through the last two years has meant so much to me.

Contents

Chapter 1 Introduction

Chapter 2 Elastic wave scattering in isotropic materials

Chapter 3 High frequency-thickness regime

Chapter 4 Low frequency SH0 mode interaction with through-thickness cracks: normal incidence

List of Tables

List of figures

Chapter 1

Introduction

1.1 Motivation

Ultrasonic guided waves are today well established in the long range inspection of large structures, following a significant amount of research in recent years. Guided wave based systems are now commercially available for inspection of structures such as pipes [1], and rail [2]. Developments for using them also to inspect plate structures are now advanced [3-6]. But current guided wave inspection techniques are limited by their developmental context. Historically, guided waves emerged as an attractive alternative to conventional point-by-point NDE for rapid inspection of large areas of structure. In applications where tens of meters of structure are to be scanned for defects, guided wave based inspection is far more efficient than the tedious and time-consuming conventional methods. Therefore, such applications use guided waves primarily as a screening tool. Sensitivity and accurate defect information are not as important as increased coverage and defect localization. The idea is that, an approximate estimate of the more severe defects along with information about their location expedites inspection. A subsequent investigation by complementary NDE methods (for example, thickness gauging [7, 8] or time of flight diffraction [9]) can quickly be carried out if more accurate defect information is required.

The NDT Group at Imperial College London (called the 'NDT Group' or the 'Imperial College NDT Group' henceforth in this thesis) pioneered this approach [2, 10-14] and past research into guided waves at the group has been based on this premise. Fundamental guided wave modes occurring at low frequency-thickness have been found to be ideal for such applications [10] [15-18] and therefore they have been the primary focus of past studies. A need to understand the implications of geometric features of waveguides on inspection procedures led to investigations of the interaction of fundamental modes with edges, thickness changes and features like bends, in plates and pipes [18-24]. In order to be able to better interpret the signals received from defects in waveguides as required for inspection purposes, the interaction of modes with cracks, notches and cylindrical holes in plates and pipes have been studied [25-29]. Guided wave propagation in structures with attenuative coatings [30-36] has been studied in order to extend the applicability of this inspection strategy.

However there are many applications where the areas of concern are not directly accessible, for example, regions of pipelines embedded in concrete as shown in Figure 1.1. Reaching them for a secondary accurate inspection may either not be possible or involve considerable cost, rendering this two-step inspection method problematic. Guided wave techniques with higher sensitivity, but which can still be deployed away from the target inspection region would be valuable in such situations. Therefore there is much interest in improving the resolution of guided wave NDE towards single step accurate defect sizing, with a reduction in the range as compared to screening applications being acceptable. This provides the motivation for the project to which the work presented in this thesis contributes. Since this is a significant step forward in guided wave NDE, there are several areas where research is needed. Several possible approaches could be taken to achieve higher resolution. The work reported here concerns the understanding of the interaction of guided waves with defects so that an appropriate approach can be selected and implemented.

In the following sections of this chapter, the theory of guided ultrasonic waves is first introduced and their application in current inspection methods is then discussed in the

light of resolution issues. Finally possible approaches to improving the resolution are considered and the method adopted in this thesis is presented.

1.2 Background: guided ultrasonic waves

Guided ultrasonic waves arise out of small elastic disturbances in bounded media. The theory of their generation and propagation is a topic dealt with in many classical texts [37-39]: here we take an approach which brings physical insights useful for our later studies. In doing so, we closely follow the treatment in the book by Auld [39].

In the bulk of the medium, away from boundaries, only two types of ultrasonic waves can exist, the longitudinal or pressure (P) waves and shear (S) waves, occurring as solutions to the governing wave equations in an infinite domain. We start with the Christoffel equation seeking plane wave solutions to the acoustic field equations, given for linear elasticity by [39]

$$k^2 \Gamma_{ij} u_j = \rho \omega^2 u_i \qquad (1.1)$$

where summation over repeated indices is assumed, k and ω represent the wavenumber and circular frequency such that a plane wave propagating in a direction given by the unit vector $\widehat{l}$ has fields proportional to $\exp[i(\omega t - k\widehat{l} \cdot \vec{r})]$, u is the displacement, ρ the material density and the Christoffel matrix, $\Gamma_{ij} = l_{iK} c_{KL} l_{Lj}$ where

$$l_{iK} = \begin{bmatrix} l_x & 0 & 0 & 0 & l_y & l_z \\ 0 & l_x & 0 & l_y & 0 & l_z \\ 0 & 0 & l_x & l_y & l_z & 0 \end{bmatrix}, \, l_{Lj} = l_{iK}{}^T \qquad (1.2)$$

and c is the general stiffness matrix represented in Auld's abbreviated indicial notation related to the conventional C_{ijkl} notation as $C_{1111} = c_{11}$, $C_{1122} = c_{12}$ etc (see page 65 from Vol. I of Auld's text[39]).

Lossless isotropic materials are of primary interest to the work presented here and deformations are always well within the region of linear elasticity. Isotropy imposes conditions such that there are only two independent elastic constants, the Lamé constants $c_{12} (= \lambda)$ and $c_{44} (= \mu)$ by which the Christoffel matrix is rendered in the simple form:

$$\Gamma_{ij} = \mu + (\lambda + \mu) \begin{bmatrix} l_x^2 & l_x l_y & l_x l_z \\ l_x l_y & l_y^2 & l_y l_z \\ l_x l_z & l_y l_z & l_z^2 \end{bmatrix} \tag{1.3}$$

We can make further use of the direction independence offered by isotropy and quickly arrive at the solutions by assuming a propagation direction which simplifies the analysis. So if we take the wave to be propagating along one of the coordinate axes, say the z axis, we will have $\widehat{l} = \hat{z}$ so that the Christoffel equation (1.1) yields

$$k^2 \begin{bmatrix} \mu & 0 & 0 \\ 0 & \mu & 0 \\ 0 & 0 & \lambda + 2\mu \end{bmatrix} \begin{bmatrix} u_x \\ u_y \\ u_z \end{bmatrix} = \rho \omega^2 \begin{bmatrix} u_x \\ u_y \\ u_z \end{bmatrix} \tag{1.4}$$

which shows that there can be two degenerate shear wave solutions with the same speed $\sqrt{\dfrac{\mu}{\rho}}$ differing only in their polarization: u_x and u_y in this case and a longitudinal wave solution, u_z with a speed $\sqrt{\dfrac{\lambda + 2\mu}{\rho}}$.

In general, for wave propagation along $\widehat{l}$ we will have shear (S) waves with two possible polarizations $\hat{a}$ or $\hat{a} \times \widehat{l}$ such that $\hat{a} \cdot \widehat{l} = 0$ and a compression (P) wave polarized along $\widehat{l}$. The two types of shear waves are called Shear Horizontal (SH) or Shear Vertical (SV) depending on whether their polarization is within or out of the plane of propagation.

In the presence of boundaries though, additional physical conditions apply and these complicate the solution. For instance, at interfaces between media, it is required that

particle velocity and traction force remain continuous at points on the boundary. These conditions cannot be satisfied by the incident waves alone and a certain number of reflected waves in the first medium and transmitted or refracted waves in the second medium need to be considered. Further, the incident and scattered waves must have the same component of the wavevector tangential to the boundary and this is a statement of Snell's law. Because elastic waves in isotropic media can have two wave velocities for each propagation direction, there can be two refraction directions at interfaces between two different media. While SH waves produce only reflected or refracted SH waves, SV and P wave interactions with interfaces are mutually coupled and can each produce the other in reflection and transmission [39]. Of importance is a stress free boundary, where SH waves are reflected totally and SV and P waves reflect partly into each other. In the vicinity of boundaries thus, there is interaction not only by way of reflection and refraction but also by conversion of shear and longitudinal modes into each other. By means of repeated reflections, boundaries have the effect of guiding waves along their surface, and their superposition eventually gives rise to different guided wave modes.

Thus guided ultrasonic waves arise as solutions to the field equations along with some specified boundary conditions. In the free plate problem for instance, the tractions at the plate surfaces must vanish. This causes bulk SH waves to reflect totally from the two plate surfaces and eventually, superimpose to give guided SH modes having particle displacements parallel to the plate surface. The mutually coupled interactions of bulk SV and P waves with the plate surface give rise to Lamb modes whose particle displacements lie entirely along the plate cross section. A look at the simpler case of construction of solutions for the SH guided wave modes can be instructive on how different characteristic features of guided waves come about. This is illustrated in Figure 1.2.

At the free boundaries of a plate, bulk SH waves reflect totally and only into SH waves. Propagation along the plate length requires that the wavevector component remain constant along this direction. Moreover for waveguides with lossless boundaries, mode solutions are travelling waves along the waveguide axis and resonant standing waves in

the transverse direction: this is the 'transverse resonance' condition and this simplifies analysis. Transverse resonance further requires that partial waves returning to the same point on the plate surface, after a round trip through the plate thickness, must experience a phase shift that is an integral multiple of 2π. Thus if h is the plate thickness, the wavenumber component along the thickness is k_h and the constant component along the plate length is $k_l = \beta$ we have:

$$k_h \cdot 2h = n \cdot 2\pi \text{ or } k_h = \frac{n\pi}{h} \text{ where } n = (0,1,2,3...) \tag{1.5}$$

since the shear wave speed $V_s = \dfrac{\omega}{|\vec{k}|}$, here:

$$V_s = \frac{\omega}{\sqrt{\beta^2 + \left(\dfrac{n\pi}{h}\right)^2}} \text{ or } \beta^2 = \left(\frac{\omega}{V_s}\right)^2 - \left(\frac{n\pi}{h}\right)^2 \tag{1.6}$$

Equation (1.6) is the dispersion relation for SH guided waves and reveals some key features of guided waves in general. The characteristic wavenumber β is frequency dependent and thus the group velocity, the velocity of a packet of waves, becomes frequency dependent or 'dispersive' and also differs from the phase velocity, the velocity of individual waves. A graphical representation using the slowness, $1/V_s$ will throw further light on the physical meaning of this important relation. Since incident and reflected partial waves would have transverse wavevector components of $+\dfrac{n\pi}{h}$ and $-\dfrac{n\pi}{h}$ respectively, the slowness curve for an isotropic material, which is just a circle, can be seen, as shown in Figure 1.3, in terms of the incident and reflected partial wave angles. At very high frequencies the angle of incidence increases and the partial waves propagate almost wholly along the plate length. With decreasing frequency, the angle of incidence decreases until it becomes zero at $\omega = \left(\dfrac{n\pi}{h}\right)V_s$ and below this 'cut-off' frequency, there is no propagation along the plate and β becomes imaginary. Thus at each frequency, a number of modes can exist (for $n = (0,1,2,3...)$ etc), the exact number being determined

by the frequency cut-off values for the different modes. And by the transverse resonance principle again, each mode will have a characteristic variation of field quantities like displacement and stress through the waveguide structure, called the 'mode shape'. These features of guided waves are captured by the different representations of the dispersion relation. Figure 1.4 shows the group velocity dispersion curves for Shear Horizontal (SH) modes in a free plate, with the different orders named 0, 1 etc. Figure 1.5 shows the displacement mode shapes for the nondispersive SH0 mode and the SH1 mode.

Figure 1.6 shows the group velocity dispersion curves for Lamb modes in a free plate. The symmetric and antisymmetric Lamb modes are labeled 'S' and 'A' followed by their respective orders.

1.3 Guided wave inspection and resolution issues

Guided waves can travel without attenuation for long distances along lossless waveguides and this fact has been used to employ them as screening tools in structures such as plates and pipes. Typically, fundamental modes at low frequency-thickness are used and defective regions in waveguides are detected from waves scattered by them. The scattered waves also contain signatures of the features of the defects and this helps estimate their severity. At the very low frequencies used for inspection for instance, the strength of the reflection of the fundamental extensional or torsional mode from circumferential cracks is approximately proportional to the cross sectional area removed by them[20, 40].

However, the application of guided waves for defect sizing, as compared to simple screening is a more challenging task. Firstly, the low frequencies of operation lead to long wavelengths for the interrogating signals and this imposes limits on the smallest defects that can be detected and sized. Further, for most industrial applications, the maximum through-wall depth of the defect is the critical parameter to be known. In current guided wave based pipe testing, the extent to which axisymmetric modes convert to non-axisymmetric modes relates to the circumferential extent of the defect [31, 41, 42].

If the defect is known to be a crack, in theory, this can be used in conjunction with the cross section information to arrive at the crack depth. But the low frequency mode conversion of the axisymmetric modes to non-axisymmetric modes is not very sensitive to changes in circumferential extents less than 15% of the pipe circumference. Therefore, given a reflection indicating a certain cross section removal, current screening-oriented systems cannot, for example, distinguish a crack that runs 50% through the pipe wall but spans only 3% of its circumference, from a less critical one which runs only 10% through the pipe but spans 15% of its circumference. More generally, defects may be corrosion patches, whose axial extent impacts the reflection [20] and thus another unknown quantity enters the picture. For screening applications, a strategy for tackling this problem has been developed [20] but though this is helpful, it does not go far enough in improving the sizing accuracy.

1.4 Higher resolution guided wave inspection: possible approaches

The fall in sensitivity due to the long wavelengths used and the inability to discriminate deep defects from shallow ones in current methods is the main stumbling block on the path to improved resolution. Two possible approaches could be taken to improve the sensitivity.

1.4.1 High frequency regime

Working at higher frequency-thickness is an immediate idea. For a given thickness, higher operating frequencies provide shorter wavelengths and also present the possibility of using information from mode conversion. Approaches such as the reflection coefficient matrix method demonstrated for the case of transverse cracks in rail [2] could then be applicable. Different features and defect types would have a characteristic matrix consisting of reflection coefficients for each combination of reflected and transmitted modes, which could be used to identify and size defects. But higher frequencies also allow multiple and dispersive modes with complex mode shapes and dealing with these is the main issue with this approach.

1.4.2 Lower frequencies

Alternatively, current operating frequencies could be retained, but a solution for the problem of resolution sought by other means such as improved array imaging. Even if such methods can just yield information about lateral size of the defect, then they can be readily used with available inspection techniques to obtain the depth information. The obvious advantages are the fewer modes and simpler mode shapes.

1.4.3 Adopted method

The overall project aims to investigate both possible approaches and propose a suitable solution based on the findings. The key to assessing their performance and relative merits is to understand the interaction of the guided wave modes existing at the respective frequency regimes, with defects. The work reported here concerns this part of the project and complements the work of other researchers in the NDT Group who are developing imaging procedures and defect-sizing strategies [43, 44]. In the high frequency approach, this will reveal how the different defect types, configurations and dimensions influence the reflection. This information can then be used to study mode conversion effects, select appropriate modes or develop multiple-mode methods. In the low frequency approach, this will provide data that will be processed by the different imaging algorithms. Further, detailed study of the mode interaction with defects, including effects such as diffraction, will help in enhancing the resolution limits. The method is therefore, first to understand this interaction by means of simulations, followed by confirmation by either analytical or experimental or both means. Finally, the appropriate method and strategy can be used as the basis on which a higher resolution inspection system is constructed.

1.5 Summary and thesis outline

In this chapter, the motivation for improving the resolution of guided wave inspection was stated and elucidated by outlining the concepts underlying current systems and their

limitations. Also two possible approaches to achieving higher resolution were highlighted and the method adopted in this thesis was introduced. The next chapter reviews the theory of guided wave scattering, starting from roots in bulk ultrasonic wave methods. Some of the principles introduced will be used through the rest of the thesis to provide analytical confirmation and gain physical insight into the results.

Chapter 3 examines the high-frequency approach from the point of view of improving the resolution of inspection. Both plates and pipes are considered and only one fundamental mode is assumed in the incident field but a multiple mode scattered response is obtained by operating at relatively high frequencies. Finite Element (FE) analysis is used to study the interaction of the A0 mode in a plate and T(0,1) mode in a pipe with long planar cracks, and 2D models are sufficient because of the simple defect geometry. A simplified analytical treatment is used to understand the physical basis behind the observed reflection behavior. The correspondence between torsional modes in a pipe and shear horizontal modes in a plate is also presented. The implications of the results are then discussed in terms of sensitivity of reflection to smaller defects and differentiation between thickness-wise deep defects from the shallow ones.

The first part of Chapter 4 (Section 4.1) serves as an introduction to the work in the rest of the thesis. This part presents FE simulation studies of the interaction of low-frequency transducer arrays with planar cracks in a thin plate. The fundamental shear horizontal plate mode SH0 is chosen because of its simple properties and its correspondence with the fundamental torsional mode T(0,1) which is used in current pipe inspection systems. Encouraging implications for sizing applications, arising from parallel array imaging work at the NDT Group using these simulation results, are then discussed. In the light of these developments, the next three chapters of the thesis study the low frequency scattering of circular-crested SH0 waves by planar cracks in some detail.

The rest of Chapter 4 considers the simple case of through-thickness cracks in an isotropic plate and the symmetric incidence problem where a line from the wave-source bisects the crack face at 90^0. FE simulations are employed to obtain trends which are

validated by experiments and theoretical analysis. The influence of the crack length and of the location of source and measurement positions on the specular reflection from the crack face is first examined. These studies show that low frequency short range scattering is strongly affected by diffraction phenomena, leading to focusing of energy by the crack in the back-scatter direction. Study of the diffraction from the crack edges reveals contributions due to a direct diffraction at the edges and multiple reverberations across the crack length. A simple diffraction model is shown to adequately represent cracks up to moderate lengths, providing an easy means of estimating the far-field of the waves. The presence of multiple diffraction components is quantitatively established and surface waves on the crack face are identified as equivalent to low-frequency symmetric modes of rectangular ridge waveguides.

Chapter 5 continues with through-thickness cracks, but incorporates the insights from Chapter 4 to study the more general problem of non-normal SH0 mode incidence. FE simulations are used to obtain trends which are then subject to analytical study and experimental confirmation. The influence of the incidence angle on reflection behaviour is first studied in terms of two complementary cases, that of normal incidence and that of specular reflection at various oblique angles. The normal incidence study suggests that for a given incidence angle, the peak reflection is concentrated around the specular direction, while the oblique incidence studies show that maximum specular reflection occurs in the case of normal incidence. The variation of diffraction with angles of incidence and monitoring is then taken up and this shows that when the first diffraction from the crack edges can be separated, its angular dependence can be obtained from bulk wave literature on similar scattering problems.

Chapter 6 further extends the investigation to consider low-frequency SH0 mode scattering by part-thickness cracks and explores its relationship with that from through-cracks. The symmetric incidence case is studied using FE simulations validated by experiments and analysis, and conclusions are inferred for general incidence angles. The influence of the crack length and the monitoring distance on the specular reflection is first examined, followed by a study of the angular profile of the reflected field. With

each crack length considered, the crack depth and operating frequencies are varied. For all crack depths studied, the trend of the results is identical to that for the corresponding through-thickness case and the values differ only by a frequency dependent scale factor. Theoretical analysis is used to interrogate the physical basis for such behaviour and estimates are suggested for the scale factor- exact for the high-frequency scattering regime and empirical for the medium and low-frequency regimes.

Finally Chapter 7 summarizes the findings in the preceding chapters and discusses the bearing on the problem of improving the resolution of guided wave imaging. Directions for future work are also suggested.

Figure 1.1 Example of applications where the areas of concern are not directly accessible: regions of pipelines embedded in concrete.
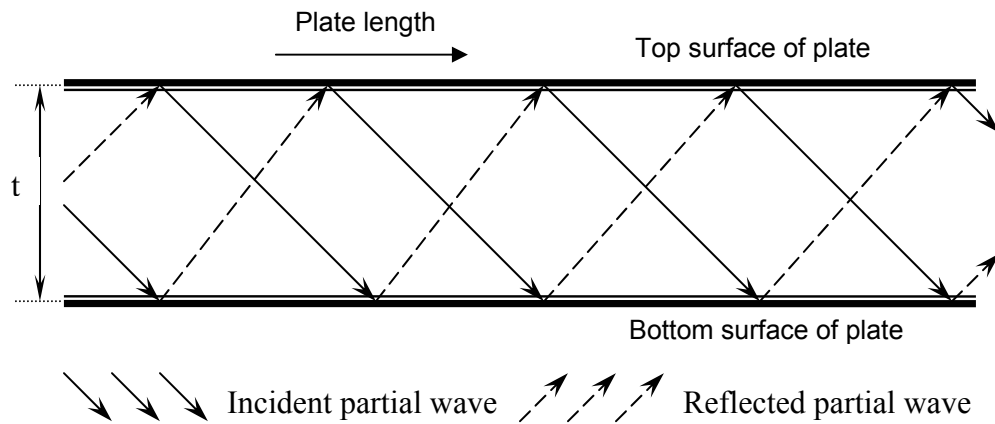
Figure 1.2 The partial wave method in a free plate. The incident and reflected partial waves have the same component of the propagation vector along the propagation direction, in this case, the length direction of the plate.
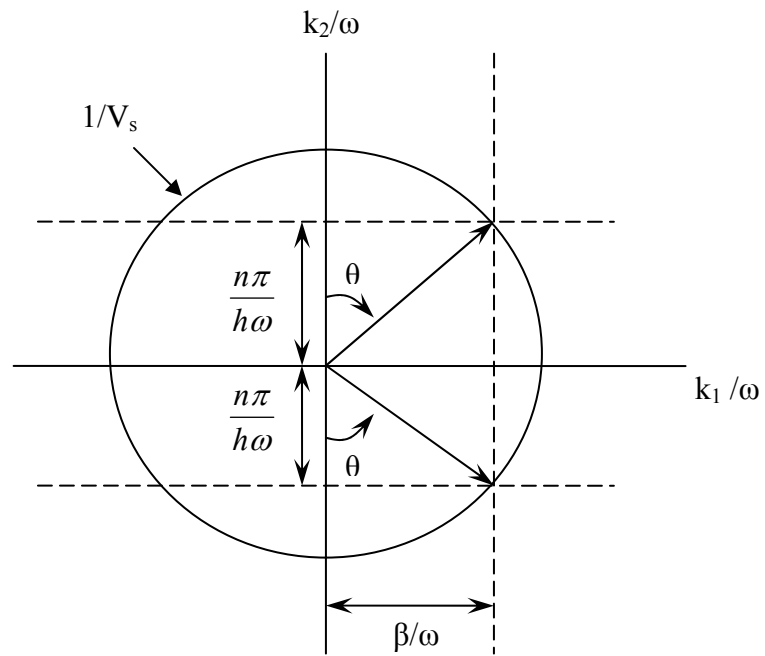
Figure 1.3 Slowness diagram for SH modes in a free isotropic plate of thickness 'h'.
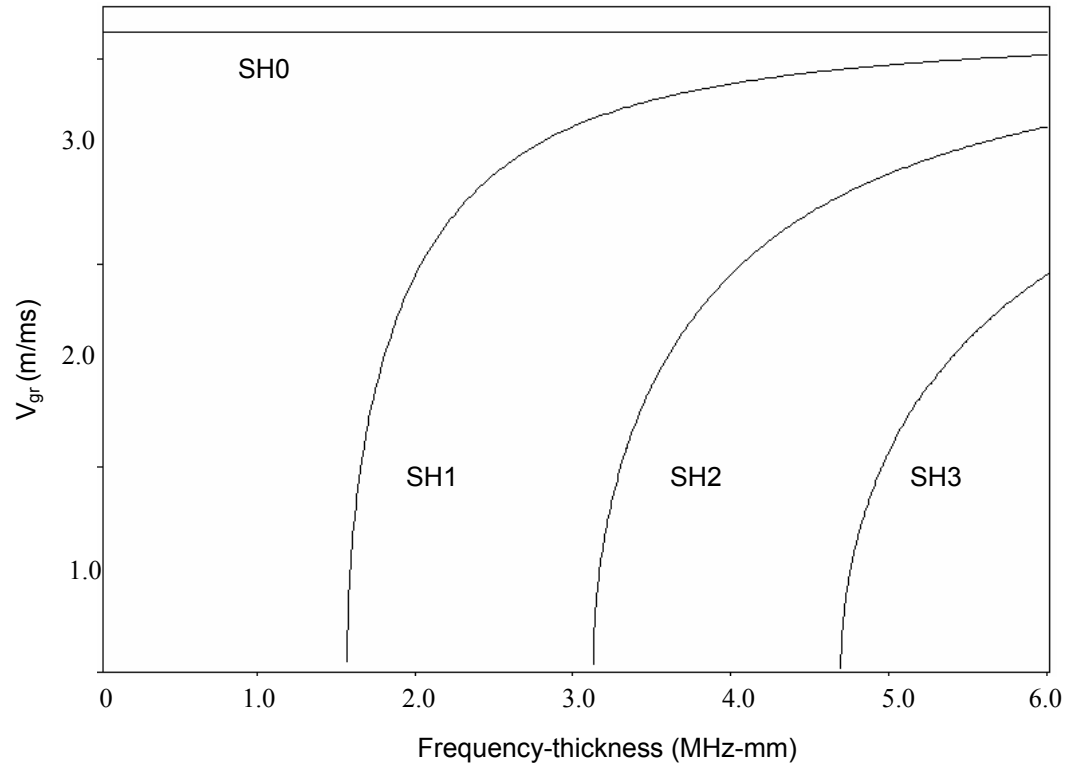
Figure 1.4 Group velocity dispersion curves for SH waves in an Aluminium plate.

(a)

(b)

(c)
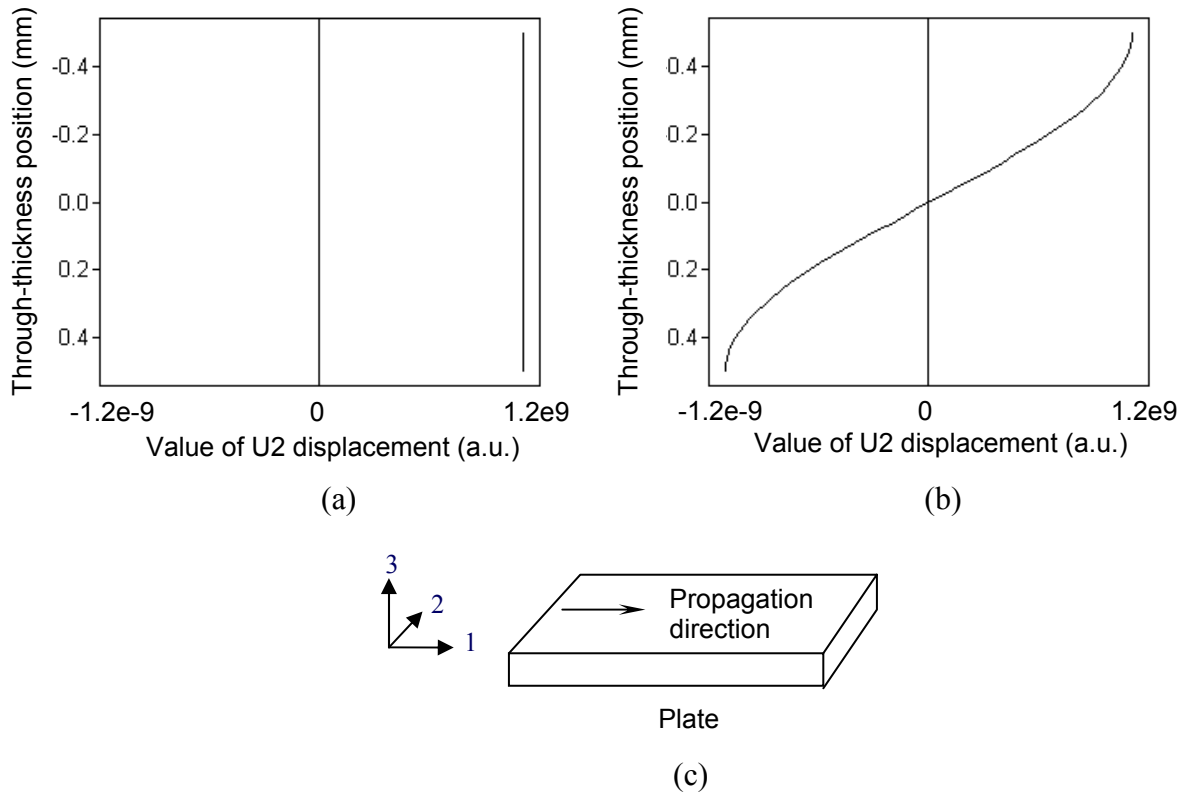
Figure 1.5 Displacement mode shapes obtained from DISPERSE [45] for (a) the nondispersive SH0 mode and (b) the SH1 mode: values for the U2 displacement are shown at the through-thickness positions of the plate; (c) shown the coordinate system. 'a.u.' stands for arbitrary units.
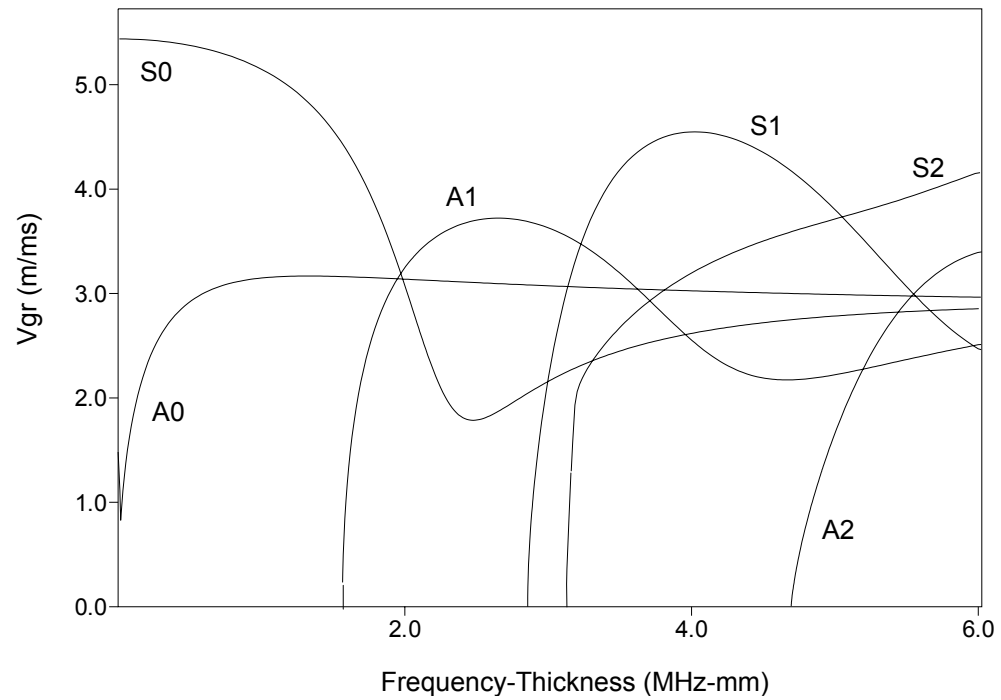
Figure 1.6 Group velocity dispersion curves for Lamb modes in a free aluminium plate. The symmetric and antisymmetric Lamb modes are labeled 'S' and 'A' followed by their respective orders.

Chapter 2

Elastic wave scattering in isotropic materials

2.1 Introduction

Understanding the interaction of wave modes with defects in materials is of crucial importance for the development of ultrasonic guided wave NDE methods. By analogy with light waves we can picture this interaction: obstacles can cause waves to reflect back and also diffract or bend near their boundaries. This is illustrated in Figure 2.1. The direction of mirror-like reflection from an object is called the direction of 'specular reflection'. While scattering is the general term used to designate the wave-defect interaction, specifically, 'diffraction' is the term used to refer to phenomena in the off-specular directions. Study of diffraction effects means that, as well as the specular reflection we also consider the detailed scattering behaviour around the defect.

This chapter reviews the basic theory of elastic wave scattering in order to clarify the physics and introduce analytical tools which we will use in the rest of the thesis. In view of this, purely numerical methods are not considered and only references describing them will be quoted. First the basic governing equations, and the emergence of guided ultrasonic waves as the superposition due to repeated reflections in the presence of boundaries, of elastic waves in unbounded media, are presented. Methods in elastic wave scattering are then reviewed and the guided wave problem is discussed through the ideas introduced. Both the vector notation and the indicial notation for tensors are used.

2.2 Governing equations and their solution

Ultrasonic waves arise out of small elastic disturbances in media, whose motion is described by the Navier equations:

$$\sigma_{ij,j} + f_i = \rho \ddot{u}_i \tag{2.1}$$

where the indicial notation has been used and the comma symbol denotes differentiation, σ_{ij} are the stresses, $f = f_i$ are the components of the body force, ρ is the material density, and $u = u_i$ are the displacements.

Making use of the constitutive relations in linear elasticity $\sigma_{ij} = C_{ijkl}\varepsilon_{kl}$ where $C_{ijkl} = C_{jikl} = C_{klij} = C_{ijlk}$ and the strain-displacement relations $\varepsilon_{ij} = \dfrac{1}{2}(u_{i,j} + u_{j,i})$, so that in general, $\sigma_{ij} = C_{ijkl}u_{k,l}$ equation (2.1) becomes

$$C_{ijkl}u_{k,jl} + f_i = \rho \ddot{u}_i \tag{2.2}$$

In the isotropic problem where only two independent elastic constants λ (= C_{1122}) and μ (= C_{2323}) exist and in the absence of body forces, this reduces to the well known form:

$$(\lambda + \mu)u_{j,ij} + \mu . u_{i,jj} = \rho \ddot{u}_i \tag{2.3}$$

In vector notation, this can be written as

$$(\lambda + \mu)\nabla\nabla \bullet \vec{u} + \mu\nabla^2\vec{u} = \rho\frac{\partial^2\vec{u}}{\partial t^2} \tag{2.4}$$

The solution to equation (2.4) is usually obtained through the Helmholtz decomposition of the displacement $\vec{u}$ in terms of scalar and vector potentials Φ and $\vec{\Psi}$ such that

$$\vec{u} = \nabla\Phi + \nabla \times \vec{\Psi} \quad \text{and} \quad \nabla \bullet \vec{\Psi} = 0 \tag{2.5}$$

Substitution in equation (2.4) leads to two wave equations for the two potentials

$$\nabla^2 \Phi = \frac{\rho}{\lambda + 2\mu} \frac{\partial^2 \Phi}{\partial t^2} \tag{2.6a}$$

$$\nabla^2 \vec{\Psi} = \frac{\rho}{\mu} \frac{\partial^2 \vec{\Psi}}{\partial t^2} \text{ with } \nabla \bullet \vec{\Psi} = 0 \tag{2.6b}$$

This reveals how in the bulk of the medium, away from boundaries, only two types of ultrasonic waves exist, the longitudinal or pressure (P) waves and transverse or shear (S) waves propagating with velocities $c_P^2 = \frac{\lambda + 2\mu}{\rho}$ and $c_S^2 = \frac{\mu}{\rho}$ respectively.

In the presence of boundaries, as described in Chapter 1, additional physical conditions apply which cause reflection and refraction of elastic waves and also the conversion of shear and longitudinal waves into each other. By means of repeated reflections, boundaries have the effect of guiding waves along the structure, and their superposition eventually gives rise to different guided wave modes, as shown in Figure 2.2. Therefore we can expect to develop methods of studying guided wave scattering problems from principles developed for bulk waves. Some significant bulk wave scattering methods are considered in the next section. In each of the subsections, the pertinent methods are first discussed and then the mathematical basis behind them is presented.

2.3 Bulk elastic wave scattering

The scattering of waves from flaws, inhomogeneities or artefacts in media has been a subject of research in many fields over the past hundred years. Specifically, the studies in the fields of acoustics and electromagnetics laid out the foundations of scattering theory. Sound waves in air or non-viscous liquids and two-dimensional electromagnetic wave problems can be studied using a single scalar potential Φ, while general electromagnetic wave problems require a single wave equation involving the vector potential $\vec{\Psi}$. The text by Jones (Clarendon Press, 1986) [46] provides an overview of methods in these areas, while the classical text by Morse and Feshbach [47] sets an excellent rigorous basis of

the various methods of analysis. A comprehensive review of exact and approximate methods in electromagnetics and acoustics can also be found in the book by Bowman et al (North-Holland, 1969) [48]. The more complicated elastic wave scattering involving the propagation of two non-degenerate particle polarizations, is built upon these developments. These in turn, directly set the basis for the more recent development of the theory of guided elastic wave scattering. The terms 'elastic wave' and 'elastodynamic' are used interchangeably in this chapter and through the rest of the thesis.

The standard theory of elastic wave scattering has been discussed in a number of texts (for ex., Graff (Clarendon Press, 1975) [49] Achenbach (North-Holland, 1973) [50]). The structure of this chapter is based on that in Harker (IOP Publishing, 1988) [51], but the content is a broad synthesis from a number of sources, both research papers and texts.

The elastic wave scattering problem shown in Figure 2.3 above is one of finding solutions to the wave equation (2.1), which also satisfy conditions at the boundaries of the artefacts. In NDE applications these are usually of the types:

(i) Rigid boundary: the *Dirichlet* problem- particle displacement vanishes on the boundary. In indicial notation,

$$u_i^{boundary} = 0 \tag{2.7}$$

(ii) Cavity: the *Neumann*-type problem- the normal traction vanishes on the boundary,

$$\left(\sigma_{ij} n_j\right)^{boundary} = 0 \tag{2.8}$$

(iii) Continuous fields: mixed boundary conditions- normal traction and particle displacement are continuous across the boundary,

$$u_i^{mat} = u_i^{art}; \left(\sigma_{ij} n_j\right)^{mat} = \left(\sigma_{ij} n_j\right)^{art} \tag{2.9}$$

In addition, the scattered fields must respect the radiation conditions which usually stipulate that they must be outgoing at infinity and appropriate edge conditions (for example, crack tip conditions) if the obstacles have sharp edges.

2.3.1 Exact solutions

2.3.1.1 Wave function expansion method

The problem of solving partial differential equations can be simplified to one of solving several ordinary differential equations, if solutions which are products of several functions each depending on only one variable can be found [52]. This is the idea behind the wave function expansion method (also called the 'eigenfunction expansion' or the 'variable separation' method), which seeks variable-separable solutions to the wave equations in (2.6). If a defect is bounded by constant coordinate surfaces of a standard coordinate system in which the wave equations permit such separation, this method can be applied. The solutions are obtained as 'expansions' or linear combinations of eigenfunctions of the resulting ordinary differential equations, which are often special functions with known properties. The unknown coefficients in the expansions are then evaluated from the system of linear equations resulting from applying appropriate continuity conditions at the boundaries of defects.

Mathematically, let the total displacement field $\vec{u}^{\,tot}$ in the unbounded medium be considered as the sum of incident and scattered fields, $\vec{u}^{\,inc}$ and $\vec{u}^{\,sc}$,

$$\vec{u}^{\,tot} = \vec{u}^{\,inc} + \vec{u}^{\,sc} \tag{2.10}$$

Through the Helmholtz decomposition of the displacement vector, we will have two differential equations to be satisfied in terms of scalar and vector potentials Φ and $\vec{\Psi}$, as given by equation (2.5).

Let us first consider the relation for the scalar potential, equation (2.6a). If we seek variable separable solutions in the coordinate directions U_i such that

$$\Phi = f_1(U_1)f_2(U_2)f_3(U_3) = \prod_j f_j(U_j) \tag{2.11}$$

Using the well known expression for the Laplacian operator in curvilinear coordinates (see for *ex.*, [53]) and writing in the frequency domain, for (2.6a) to be valid we should have

$$\frac{c_L^2}{h_1 h_2 h_3} \frac{1}{f_j} \frac{\partial}{\partial u_j} \left(\frac{h_k h_l}{h_j} \frac{\partial f_j}{\partial u_j} \right) + \omega^2 = 0 \tag{2.12}$$

where $h_i = \left| \dfrac{\partial \vec{r}}{\partial U_i} \right|$ are scale factors of the coordinate system with a position vector

$\vec{r} = \vec{r}(U_1, U_2, U_3)$ and ω is the circular frequency.

Lumping ω^2 with the term in coordinate direction '3' without loss of generality, we find that equation (2.11) can be separated into ordinary differential equations only when we can find constants λ_i such that

$$\frac{c_L^2}{h_1 h_2 h_3} \frac{\partial}{\partial u_1} \left(\frac{h_2 h_3}{h_1} \frac{\partial f_1}{\partial u_1} \right) = f_1 \lambda_1; \quad \frac{c_L^2}{h_1 h_2 h_3} \frac{\partial}{\partial u_2} \left(\frac{h_1 h_3}{h_2} \frac{\partial f_2}{\partial u_2} \right) = f_2 \lambda_2$$

$$\frac{c_L^2}{h_1 h_2 h_3} \frac{\partial}{\partial u_3} \left(\frac{h_1 h_2}{h_3} \frac{\partial f_3}{\partial u_3} \right) = f_3 (\lambda_3 - \omega^2) \text{ with } \lambda_1 + \lambda_2 + \lambda_3 = 0 \tag{2.13}$$

which will further happen only when f_i are eigenfunctions of the respective differential operators on the left hand side of each equation in (2.13). Such eigenfunctions usually also need to be orthogonal to satisfy the boundary conditions and this happens only for a limited number of coordinate systems. For the scalar wave equation thus, this happens only for 11 coordinate systems, enumerated in the book by Harker (p 67, Ch 3) [51]

Turning to the equation for the vector potential, (2.6b), we see that actually this is a set of three equations for the three components $\Psi_i \hat{e}_i$ of $\vec{\Psi}$:

$$\left[\sum_{i=1}^{3} \frac{c_T^2}{h_1 h_2 h_3} \frac{\partial}{\partial u_i} \left(\frac{h_j h_k}{h_i} \frac{\partial \Psi_i}{\partial u_i} \right) + \omega^2 \Psi_i \right] \hat{e}_i = 0 \tag{2.14}$$

Except for Cartesian coordinates, all three components can occur in all three equations and this coupling makes finding solution to the vector wave equation very difficult. But if the scale factors are such that one of them say h_3 is constant and h_2 / h_1 is independent of U_3, the term $\nabla \times \vec{\Psi}$ with $\nabla \bullet \vec{\Psi} = 0$ in the Helmholtz decomposition can be written in terms of two scalar potentials ψ and χ such that [54]

$$\nabla \times \vec{\Psi} = \nabla \times (\psi \cdot \hat{e}_3) + \nabla \times \nabla \times (\chi \cdot \hat{e}_3) \tag{2.15}$$

The vector wave equations in (2.6b) then yields two scalar wave equations in ψ and χ:

$$c_T^2 \nabla^2 \psi = \frac{\partial^2 \psi}{\partial t^2} \text{ and } c_T^2 \nabla^2 \chi = \frac{\partial^2 \chi}{\partial t^2} \tag{2.16}$$

Of the 11 coordinate systems that allow the separation of the scalar equation as in (2.12), only 6 have scale factors permitting a decomposition of the type (2.15). These are the rectangular, circular, elliptic and parabolic cylindrical, spherical and the conical systems [55]. When cylindrical symmetry is satisfied, parabolic, oblate spheroidal and prolate spheroidal systems also join the list.

When such separation is possible, $\vec{u}^{inc}$ and $\vec{u}^{sc}$ can be written in terms of expansions of eigenfunctions f_j, g_j and w_j of the wave equations in φ, ψ and χ through unknown coefficients A_{jm}, B_{jm} and C_{jm} as

$$u^{inc/sc} = \nabla \left(\prod_j \left(\sum_m A_{jm} f_{jm}(u_j) \right) \right) + \nabla \times \left(\left(\prod_j \left(\sum_m B_{jm} g_{jm}(u_j) \right) \right) \hat{e}_3 \right) + \tag{2.17}$$

$$\nabla \times \nabla \times \left(\left(\prod_j \left(\sum_m C_{jm} w_{jm}(u_j) \right) \right) \hat{e}_3 \right)$$

The stresses can be obtained from these using the constitutive relationships and the strain-displacement relations. Finally, the expansion coefficients are found by applying suitable boundary conditions from equations (2.7) - (2.9) and the radiation conditions.

In theory by this method solutions to any degree of accuracy can be found by extending the truncation limit of the summations in (2.17). But mixing of the eigenfunctions due to the boundary conditions in the general elastodynamic case further restricts the choice of coordinate systems to the rectangular, circular cylinder and spherical coordinate systems [51] [55]. The early literature thus focussed on scattering from simple defects such as circular or cylindrical inclusions or flaws. Scattering problems involving more complicated defect geometries were solved under very specialized conditions of symmetry. The extensive review by Guz' et al. (1978) [56] covers many early studies on scattering while the monograph by Pao and Mow (Crane Russak, 1973) [55] covers the range of problems which are analytically solvable.

2.3.1.2 Integral representations and the integral equation method

As noted in the previous subsection, solutions using the wave function expansion method are hard to obtain for defect geometries other than spherical and circular cylindrical. Even in special cases (for instance, that of a spheroid studied in Oien and Pao (1973) [57] with axisymmetric excitation) where the symmetry allows an exact solution, the convergence deteriorates and the solution for limiting cases cannot be obtained (see Datta and Sangster (1974) [58]). Although the scattering from some types of cracks can be treated by this method by considering them to be limiting cases of elliptical or parabolic systems, the complicated eigenfunctions encountered effectively rule these out. A rare example of the study of scattering from cracks by this method is the work of Harumi (1961, 1962) [59, 60] using elliptically cylindrical coordinates and Mathieu function expansions, but even he was able to present solutions only in the long wave length (Rayleigh) limit. Thus for a large class of elastic wave scattering problems, other methods of solution must be constructed. Such methods often arrive at an integral equation (integro-differential equation to be more precise) as their end result, which can be evaluated either numerically or 'exactly' in terms of a set of expansions.

The earliest routes to arrive at integral equations for solving scattering problems were using transform methods (Laplace, Fourier, Hankel etc). When symmetries in the

configuration – defect and incident wave- are such that the scattering problem is reduced to only two dimensions, transform methods are effective. The scattering of elastic waves from semi-infinite cracks using this method usually requires the application of techniques such as the Wiener-Hopf [61, 62]. Transform methods with finite-width 'strip' cracks or circular or 'penny shaped' cracks lead to simultaneous 'dual integrals'. Mal, (1968, 1970) [63-65], Sih and Loeber (1968, 1969) [66, 67] and others considered such classes of crack problems which allowed simplifications by way of symmetries.

Physically, the scattering of elastic waves comes about from an obstacle excited by the incident waves acting as a secondary source, as described by Huygens' Principle. The mathematical basis for this principle as applicable to acoustic (scalar) waves is given by Helmholtz's integral formulas in the steady state and Kirchhoff's generalization for arbitrary time-dependence [55]. Based on analogous results for elastic waves, it is possible to derive an alternative integral representation for the scattering problem, which is more direct and intuitively closer to the physics. The paper by Pao and Varatharajulu (1976)[68] where Helmholtz and Kirchhoff type formulas are systematically derived for both surface and volume scattering through the application of the divergence (Green's) theorem is notable among the early work. Gubernatis *et al.* (1977) [69] highlighted many important aspects of elastodynamic scattering, arriving independently at an integral representation. Reciprocity theorems in conjunction with the Green's function present another powerful and elegant route in arriving at such relations, becoming the standard conventional method over the years. Tan (1975, 1977) [70, 71], Varatharajulu (1976) [72], Kino (1978) [73], Auld (1979) [74], Kino and Khuri-Yakub (1992) [75], and more recently, Achenbach (Cambridge University Press, 2003) [76] and Achenbach (2006) [77] provide a comprehensive overview and highlight the significance of reciprocity relations in elastodynamics. The book by de Hoop [78] can be consulted for further reference in this regard.

Through the rest of this thesis, an integral representation for the scattered displacement derived from reciprocity relations is used to bring physical insight to the different studies. For this reason, here the key results leading to the representation integrals and integral

equations through this method for time-harmonic waves, are viewed based on the work in [68], [70], [77] and [79]. The difficulties in solving the equations will be highlighted. Integral representations for the scattered field can also be obtained by other approaches: for example through conservation integrals as described by Zhang and Gross (Computational Mechanics, 1998) [80].

Reciprocity theorems relate the displacements, tractions and body forces for two different loading conditions in a given medium. If these two conditions be given by superscripts I and II, the Navier equations for the two 'states' in an elastic body yield,

$$\sigma_{ij,j}^{I} + f_i^{I} = \rho \ddot{u}_i^{I} \tag{2.18a}$$

$$\sigma_{ij,j}^{II} + f_i^{II} = \rho \ddot{u}_i^{II} \tag{2.18b}$$

When all fields are time harmonic, (i.e., they are proportional to $e^{i\omega t}$) we have

$$\sigma_{ij,j}^{I} + f_i^{I} = -\rho \omega^2 u_i^{I} \tag{2.19a}$$

$$\sigma_{ij,j}^{II} + f_i^{II} = -\rho \omega^2 u_i^{II} \tag{2.19b}$$

Combining 2.19a and 2.19b suitably, invoking the symmetry of the stiffness tensor and employing Gauss's divergence theorem we obtain **the global reciprocity theorem for time harmonic fields** for a region V with boundary S and unit outward normal $\vec{n} = n_i \hat{e}_i$:

$$\int_V (f_i^{I} u_i^{II} - f_i^{II} u_i^{I}) dV = \int_S (\sigma_{ij}^{II} u_i^{I} - \sigma_{ij}^{I} u_i^{II}) n_j dS \tag{2.20}$$

We can observe that in the absence of body forces, equation (2.20) becomes apparent as a consequence of the familiar principle of virtual work in static elasticity. In view of the principal result in elastostatics due to Betti and general extension considering elastodynamics due to Rayleigh, it is some times called Rayleigh-Betti reciprocity relation.

Representation Integrals The reciprocity relation in equation (2.20) can readily be used to obtain an integral representation for waves scattered by an obstacle in an otherwise

homogenous medium. Let the obstacle of volume V bounded by a surface S with unit outward normal $\vec{n}$ be wholly located within a large region of volume V_R and outer surface S_R. For simplicity, we assume S_R to be a sphere having a large radius $R \to \infty$ and centred at the observation point, Q. These details are shown in Figure 2.4.

We again let the displacements and stresses $\{u_i^{tot}, \sigma_{ij}^{tot}\}$ giving the total field in the unbounded region V_R to be composed of the incident field $\{u_i^{inc}, \sigma_{ij}^{inc}\}$ and the scattered field $\{u_i^{sc}, \sigma_{ij}^{sc}\}$. The incident field is assumed to be generated by sources in V_R in the absence of any other sources including those caused by the obstacle. In this light, the scattered field is equivalent to $\{u_i^{tot} - u_i^{inc}, \sigma_{ij}^{tot} - \sigma_{ij}^{inc}\}$ and seen to satisfy the wave equation without any body force term.

Let us first consider the domain V bounded by the obstacle surface S and take two auxiliary elastodynamic states: state I is the incident field and state II is the field at any position $\vec{p}$ in the free medium due to the application at position $\vec{r}$ of a unit point force $f_i = \delta(\vec{p} - \vec{r})\hat{e}_i\, e^{i\omega t}$. The three-dimensional delta function $\delta(\vec{p} - \vec{r})$ has the property:

$$\int_{Volume} \left[\left(\delta(\vec{p} - \vec{r})\hat{e}_i\right)u_k(\vec{p})\right]dV = u_k(\vec{r}), \vec{r} \in V_R - V$$

$$= 0 \text{ otherwise}$$

(2.21)

where $V_R - V$ is the unbounded region outside the obstacle.

The response due to such an input is the field $\{G_{k;i}(\vec{p}\,|\,\vec{r}), \Sigma_{kj;i}(\vec{p}\,|\,\vec{r})\}$ where $G_{k;i}(\vec{p}\,|\,\vec{r})$ is the second rank Green's displacement tensor giving the displacement component in the $\hat{e}_k$ direction at position $\vec{p}$ due to the force applied in $\hat{e}_i$ direction at $\vec{r}$ and $\Sigma_{kj;i}(\vec{p}\,|\,\vec{r})$ is the corresponding third rank Green's stress tensor; both G and Σ are symmetric in $\vec{p}$ and $\vec{r}$. In the indicial notation, the displacements and stresses $\{u_k^G(\vec{p}\,|\,\vec{r}), \sigma_{kj}^G(\vec{p}\,|\,\vec{r})\}$ at $\vec{p}$ relate to $\{G_{k;i}(\vec{p}\,|\,\vec{r}), \Sigma_{kj;i}(\vec{p}\,|\,\vec{r})\}$ as $u_k^G(\vec{p}\,|\,\vec{r}) = G_{k;i}(\vec{p}\,|\,\vec{r})\hat{e}_i$ and $\sigma_{kj}^G(\vec{p}\,|\,\vec{r}) = \Sigma_{kj;i}(\vec{p}\,|\,\vec{r})\hat{e}_i$.

Applying these as the values for the two states in the reciprocity relation (2.20), we find:

$$\int_V \left[f_i^I G_{i;k}(\vec{p}\,|\,\vec{r}) - \left(\delta(\vec{p}-\vec{r})\hat{e}_i\right)u_k^{inc}(\vec{p})\right]dV = \int_S \left[\left(\Sigma_{ij;k}(\vec{s}\,|\,\vec{r})n_j\right)u_i^{inc}(\vec{s}) - \left(\sigma_{ij}^{inc}(\vec{s})n_j\right)G_{i;k}(\vec{s}\,|\,\vec{r})\right]\cdot dS$$

$$(2.22)$$

Making use of the definition in (2.21) and noting that the sources that generate the incident field lie outside the obstacle, we obtain for points $\vec{r} \in V$ with $n_j\hat{e}_j$ point outward from V,

$$\int_S \left[\left(\Sigma_{ij;k}(\vec{s}\,|\,\vec{r})n_j\right)u_i^{inc}(\vec{s}) - \left(\sigma_{ij}^{inc}(\vec{s})n_j\right)G_{i;k}(\vec{s}\,|\,\vec{r})\right]\cdot dS = 0 \qquad (2.23)$$

We then turn to the domain $V_R - V$ bounded inside by S and outside by S_R *(shown shaded in Figure 2.4)* and take the two auxiliary states: state I is the scattered field in the medium due to (secondary) sources on the surface of the obstacle and state II again is the response to a point force applied at the required observation point Q. Substitution in the reciprocity relation (2.20) yields:

$$\int_{V_R-V} \left[f_i^I G_{i;k}(\vec{p}\,|\,\vec{r}) - \left(\delta(\vec{p}-\vec{r})\hat{e}_i\right)u_k^{sc}(\vec{p})\right]dV = \int_{S+S_R} \left[\left(\Sigma_{ij;k}(\vec{s}\,|\,\vec{r})n_j\right)u_i^{sc}(\vec{s}) - \left(\sigma_{ij}^{sc}(\vec{s})n_j\right)G_{i;k}(\vec{s}\,|\,\vec{r})\right]\cdot dS$$

$$(2.24)$$

where the normals $n_j\hat{e}_j$ are directed outward from the volume $V_R - V$, meaning that on the surface S of the obstacle, they point into it.

Invoking (2.21) again, dropping the body force term since all secondary sources lie on or inside S and rearranging the terms and letting $R \to \infty$, we have for $\vec{r} \in V_+ (= V_R - V)$:

$$u_k^{sc}(\vec{r}) = \int_S \left[\left(\sigma_{ij}^{sc}(\vec{s})n_j\right)G_{i;k}(\vec{s}\,|\,\vec{r}) - \left(\Sigma_{ij;k}(\vec{s}\,|\,\vec{r})n_j\right)u_i^{sc}(\vec{s})\right]dS + \eta_k(\vec{r}) \qquad (2.25)$$

where

$$\eta_k(\vec{r}) = \int_{S_\infty} \left[\left(\sigma_{ij}^{sc}(\vec{s})n_j\right)G_{i;k}(\vec{s}\,|\,\vec{r}) - \left(\Sigma_{ij;k}(\vec{s}\,|\,\vec{r})n_j\right)u_i^{sc}(\vec{s})\right]dS \qquad (2.26)$$

The term $\eta_k(\vec{r})$ given by (2.26) above vanishes due to Sommerfeld-like radiation conditions for elastic waves which stipulate that when there are no sources at infinity, the energy flux through a sphere at infinity should be in the outward direction.

Employing the $\vec{p}/\vec{r}$ symmetry in G and Σ, we thus obtain the well known **surface integral representation for the scattered displacement**:

$$u_k^{sc}(\vec{r}) = \int_S \left[\sigma_{ij}^{sc}(\vec{s}) G_{i;k}(\vec{r}\,|\,\vec{s}) - \Sigma_{ij;k}(\vec{r}\,|\,\vec{s}) u_i^{sc}(\vec{s}) \right] \cdot n_j \, dS, \vec{r} \in V_+ \qquad (2.27)$$

Equation (2.27) is clearly a mathematical statement of the Huygens' Principle for steady state waves: the scattered field arises due to surface sources at the boundary of the obstacle. We can also combine equations (2.27) and (2.23) choosing a consistent definition for normals as outward-pointing and obtain the **formula for the scattered displacement in terms of the total field**:

$$u_k^{sc}(\vec{r}) = \int_S \left[\Sigma_{ij;k}(\vec{r}\,|\,\vec{s}) u_i^{tot}(\vec{s}) - \sigma_{ij}^{tot}(\vec{s}) G_{i;k}(\vec{r}\,|\,\vec{s}) \right] \cdot n_j \, dS \qquad (2.28)$$

We also obtain for the **total field outside the obstacle the formula**,

$$u_k^{tot}(\vec{r}) = u_k^{inc}(\vec{r}) + \int_S \left[\Sigma_{ij;k}(\vec{r}\,|\,\vec{s}) u_i^{tot}(\vec{s}) - \sigma_{ij}^{tot}(\vec{s}) G_{i;k}(\vec{r}\,|\,\vec{s}) \right] \cdot n_j \, dS, \vec{r} \in V_+ \qquad (2.29)$$

The special situation when the observation point approaches the surface of the obstacle, i.e. in the limit $\vec{r} \to \vec{s}$ is of particular interest when applying the boundary conditions. In this case a slightly different result follows from potential theory, which is not derived here, but stated from literature (See for example, [70]):

$$\frac{1}{2} u_k^{tot}(\vec{r}) = u_k^{inc}(\vec{r}) + \int_S \left[\Sigma_{ij;k}(\vec{r}\,|\,\vec{s}) u_i^{tot}(\vec{s}) - \sigma_{ij}^{tot}(\vec{s}) G_{i;k}(\vec{r}\,|\,\vec{s}) \right] \cdot n_j \, dS, \vec{r} \in S \quad (2.30)$$

In (2.30) above, the surface integral is to be interpreted as a Cauchy principal value.

A volume formulation taking the sources as being distributed within the obstacle rather than on its surface is useful when the treating scattering from bulk inhomogeneities. Following [68] and [69], the **volume integral representation equivalent to equation (2.30)** is written for $\vec{r} \in V_R - V$ and $\vec{v} \in V$ as:

$$u_k^{tot}(\vec{r}) = u_k^{inc}(\vec{r}) + \int_V \left[\Delta\rho(\vec{v})\omega^2 \left(u_i(\vec{v})G_{i;k}(\vec{r}\,|\,\vec{v}) \right) - \Delta C_{ijlm}(\vec{v})\left(\Sigma_{ij;k}(\vec{r}\,|\,\vec{v})u_{l,m}(\vec{v}) \right) \right] \cdot dV \quad (2.31)$$

where ρ and C_{ijlm} are the density and stiffness of the parent medium, $\Delta\rho(\vec{v})$ and $\Delta C_{ijlm}(\vec{v})$ are the differences in material properties between the medium and the obstacle, which can in general depend on the position $\vec{v}$ inside the obstacle, and $u_{l,m}(\vec{v}) = \dfrac{\partial u_l(\vec{v})}{\partial U_m}$ give the strain field within the obstacle.

The integral formulation for scattering incorporates the continuity conditions across boundaries implicitly while assuming the differentiability of displacement and its gradient along them. Analogous relations in the time domain can be obtained by accounting for contributions at each frequency through the Fourier transform [68].

Integral equations Through the conditions prescribed on the boundary of the obstacle, the surface integral representation can be used to derive integral equations for the different field quantities. The standard procedure is to let the observation position approach the boundary of the obstacle and obtain the values in the limit. For example when the displacements at the surface of the scatterer vanish as given by equation (2.7), the scattered displacement is obtained from a limiting process such as that in (2.30). We obtain a Fredholm integral equation of the first kind for the total tractions,

$$-u_k^{inc}(\vec{s}) = \int_S -\sigma_{ij}^{tot}(\vec{s})\left[G_{i;k}(\vec{r}\,|\,\vec{s}) \cdot n_j \right] dS, \vec{r} \to \vec{s} \in S \qquad (2.32)$$

The kernels in equation (2.32) become singular due to the behaviour of Green's tensor when r approaches s.

A more common example of a scatterer is a cavity which is described by Neumann conditions in (2.8). In this case since the total normal traction on the obstacle surface vanishes, equation (2.28) reduces to

$$u_k^{sc}(\vec{r}) = \int_S u_i^{tot}(\vec{s})\Sigma_{ij;k}(\vec{r}\,|\,\vec{s}) \cdot n_j dS, \vec{r} \in V_+ \tag{2.33}$$

The scattered tractions are then obtained from (2.33) using the general form of the constitutive relationships:

$$\sigma_{il}^{sc}(\vec{r})n_i = C_{kwlm} n_w(\vec{r})\frac{\partial}{\partial U_m}\int_S u_i^{tot}(\vec{s})\Sigma_{ij;k}(\vec{r}\,|\,\vec{s}) \cdot n_j dS, \vec{r} \in V_+ \tag{2.34}$$

where $n_w(\vec{r})$ is the normal to a fictitious surface enclosing the obstacle at position $\vec{r}$

Taking the limit $\vec{r} \to \vec{s}$ and recognizing that $\sigma_{ij}^{sc}(\vec{s})n_j = -\sigma_{ij}^{inc}(\vec{s})n_j$, since $\sigma_{ij}^{tot}(\vec{s})n_j = 0$, we again obtain a Fredholm integral equation of the first kind for the total displacement but this time, the kernels are hypersingular, because of the presence of spatial derivatives of the stress Green's function:

$$-\sigma_{il}^{inc}(\vec{s})n_l = C_{kwlm} n_w(\vec{s})\frac{\partial}{\partial U_m}\int_S u_l^{tot}(\vec{s})\Sigma_{ij;k}(\vec{r}\,|\,\vec{s}) \cdot n_j dS, \vec{r} \to \vec{s} \in S \tag{2.35}$$

Integral equations identical in form to (2.35) are obtained for ideal cracks which are often taken to be free of normal tractions:

$$-\sigma_{il}^{inc}(\vec{s})n_l = C_{kwlm} n_w(\vec{s})\frac{\partial}{\partial U_m}\int_{S^+} \Delta u_l^{tot}(\vec{s})\Sigma_{ij;k}(\vec{r}\,|\,\vec{s}) \cdot n_j dS, \vec{r} \to \vec{s} \in S \tag{2.36}$$

where the integral is now on one of the faces of the crack, say the insonified face s^+ and $\Delta u^{tot} = \Delta u^{sc} = (u)^+ - (u)^-$ is jump in displacement across the crack faces, called the 'Crack Opening Displacement' (COD).

Care must be taken in evaluating the singular integral equations (2.32) and hypersingular equations (2.35) and (2.36) and various procedures are known in literature [76], [80]. For

finite cracks, even transform methods (for ex. Krenk and Schmidt (1982), [81] Datta (1979, 1980) [82, 83], Kundu (1990) [84]) yield representations equivalent to the one arrived above in (2.36) – thus there is a large body of literature on evaluating these integrals; apart from purely numerical methods, the method of moments where the COD is expanded in a set of basis functions taking care of edge conditions is widely applied. The comprehensive review paper by Bostrom (2003) [85] describes the hypersingular integral equation method for cracks in detail and discusses this equivalence. Further summaries can be found in the individual works by Martin and Wickham (1983) [54], Lin and Keer (1987) [86], Lewis and Wickham (1992) [87]; Lewis et al (1998) [88] provide a good overview of these developments. Zhang and Gross (p. 65 in [80]) have derived a non- hypersingular traction integral equation for cracks, based on a two-state conservation integral. This method shifts the derivative in equation (2.36) entirely on the COD, thus circumventing the hypersingularities.

To summarize, the key results of this subsection are the reciprocity theorem (2.20), the integral formulas (2.27)-(2.31), and the integral equations (2.32), (2.35) and (2.36).

2.3.2 Approximate analytical methods

In order to solve for scattering problems involving more complex geometries (both inclusions and cracks), several approximate analytical methods were developed, and the integral equation representation of the scattering problem provided a convenient starting point for such methods. Kraut (1976) [89], Datta (1978) [82] and Hackman (1993) [90] review some exact and approximate analytical work on elastic wave and acoustic scattering. Only a significant few of the large class of such approximate methods are discussed here, with the guided wave case in view. The various approximate methods could be thought of as applying to different frequency or wavelength regimes.

2.3.2.1 Low frequencies

In the limit of low frequency or long wavelength, the Born approximation and the quasi-static approximation have been used successfully to solve several scattering problems: see Domany *et al.* (1978) [91], Gubernatis *et al.* (1977, 1979) [92-94], Kino (1978) [73], Coussy (1986)[95]. Jain and Kanwal (1982) [96] have provided some extensions of the two-dimensional Born approximation results to 3 dimensional problems. Though there are a number of ways of arriving at the approximate solutions proposed by these methods, here we will follow Gubernatis *et al.* (1977) [69].

First, an integral representation such as that in (2.30) or (2.31) is obtained for the scattered field. In view of (2.10) and since the scattered displacement, u_i^{sc} is obtained as a function of the displacements and strains within the scatterer as given by (2.31), we write in the indicial notation,

$$u_i^{tot} = u_i^{inc} + u_i^{sc}(u_i^{tot}, \varepsilon_{ij}^{tot})$$

(2.37)

The Born approximation then assumes the displacement field and its gradient inside the scatterers (volume defects) or on their surface (cavities, cracks) to be identical to those that would be present in the same region of the medium in the absence of the scatterer. Therefore in the Born approximation,

$$u_i^{tot} = u_i^{inc} + u_i^{sc}(u_i^{inc}, \varepsilon_{ij}^{inc})$$

(2.38)

The Quasi-static approximation uses the field values that would be due to an applied static load, in the long wavelength limit. If $u_i^{inc} = u_i^0 e^{i\omega \cdot t}$ then in this approximation,

$$u_i^{tot} = u_i^{inc} + u_i^{sc}(u_i^0, \varepsilon_{ij}^{\sigma})$$

(2.39)

where $\varepsilon_{ij}^{\sigma}$ is the strain field inside the scatterer under the action of a uniform applied static strain field.

Since the values inside shapes such as ellipsoids, are known uniform constants and have been well documented in literature (see Eshelby (1957, 1959) [97, 98]), exact results are obtainable for the scattered field. For structures containing cracks or distributions of cracks, results from handbooks such as that by Tada et al. (1973) [99] could be used.

In the limit of small perturbations, the static strain fields approach those of strain fields in the absence of the scatterer and thus these two approximations yield the same result. While the Born approximation gives best results in backscattering, the quasi-static approximation applies in general in the long wavelength limit. The long wavelength approximations, especially the quasistatic approximation, have been used extensively in the past two decades in elastic wave inverse problems (see Rose (1979) [100] Rose (1989) [101] Wu (1985) [102] Yamada (2003) [103]) and have also been extended to pulses and the time domain(see for *ex.*, Rose (1982) [104]).

The quasi-static approximation could also be invoked when solving the scattering problem starting with other formulations. Datta and co-workers (1974, 1979) [58, 83] presented an equivalent approximate solution using the differential equation formulation and a 'matched asymptotic expansion' method. Another line of research follows the work of Baik and Thompson (1984) [105] and Margetan *et al.* (1988) [106] who used the quasi-static approximation to link their representation of imperfect interfaces by interfacial spring models to known static solutions.

2.3.2.2 High frequencies

In the high-frequency limit, elastodynamic ray methods provide an excellent route to approximate solutions for scattering problems. Simple geometrical ray theory involving reflection and refraction often yields sufficiently accurate results close to the specular or near-specular directions. But at other angles diffraction effects can play an important role and the Geometric Theory of Diffraction (GTD) (Karal Jr (1959) [107], Keller (1964) [108]) formulated to include them within the framework of ray theory provides excellent approximations [109], [61].

Approximate solutions to the scattered field can also be obtained through the integral representation formulas, taking the prediction by ray methods as an estimate of the total scattered displacement on the obstacle. Of these the Kirchhoff approximation which takes the result given by simple ray theory for total scattered field on the obstacle is well known (see Auld (1978) [110], Kino (1978)[73], Chapmann (1984) [61] Schmerr *et al.* (1989) [111]); more sophisticated methods which account for diffraction are also reported in literature [109]. The book by Achenbach *et al.* [62] covers ray methods in detail, here they are briefly summarized.

These methods are based on constructing high frequency series solutions to the governing equations involving terms of the type $(i\omega \cdot h / c)^{-n}$ (where h is a characteristic dimension of the defect and c is the wave speed), which would be valid asymptotically as $\omega \cdot h / c \rightarrow \infty$. In practice, they are known to give useful results even at wavelengths comparable to 'h' and the results can be extended to the time-domain. Physically, such expansions have a simple geometric interpretation in terms of rays and the leading term is just what would be predicted by geometrical wave theory, while subsequent terms offer corrections to it.

In what follows, we will first see how asymptotic series expansions to the wave field lead to predictions of ray behaviour. We will then consider the results for the standard ray theory involving reflection and refraction. Finally approximate theories which offer corrections and improve the scope of application of ray theory will be introduced.

Standard Ray Theory In describing the ray method, the analysis presented here is developed using displacement potentials. For a detailed derivation from entirely geometrical considerations and proof of equivalence of these two approaches, the classical paper by Keller [112] can be consulted. Let us consider the wave equation for the scalar potential Φ in the frequency domain,

$$\nabla^2 \Phi + k_P^2 \Phi = 0 \text{ where } k_P = \frac{\omega}{c_P} \tag{2.40}$$

When we seek solutions to (2.40) of the form

$$\Phi = e^{ik_P \varphi_p(\vec{r})} \sum_{n=0}^{\infty} \frac{1}{(ik_P)^{n+1}} A_n^P(\vec{r})$$

(2.41)

where $\varphi_P(\vec{r})$ and $A_n^P(\vec{r})$ are phase and amplitude functions respectively, we obtain:

$$(ik_p)\left\{\left(\left|\nabla \varphi_P\right|^2 - 1\right)A_0^P\right\} + \left\{\left(\left|\nabla \varphi_P\right|^2 - 1\right)A_1^P + 2(\nabla \varphi_P \bullet \nabla)A_0^P + \left(\nabla^2 \varphi_P\right)A_0^P\right\} + \dots$$

$$\dots \sum_{n=2}^{\infty} \frac{1}{(ik_P)^{n-1}}\left\{\left(\left|\nabla \varphi_P\right|^2 - 1\right)A_n^P + \left[2(\nabla \varphi_P \bullet \nabla)A_{n-1}^P + \left(\nabla^2 \varphi_P\right)A_{n-1}^P\right] + \nabla^2 A_{n-2}^P\right\} = 0$$

(2.42)

Since (2.41) must be valid asymptotically as $k_p = \omega \cdot / c \to \infty$, letting $A_0^P \neq 0$, we have

$$\left|\nabla \varphi_P\right|^2 = 1$$

(2.43a)

$$2(\nabla \varphi_P \bullet \nabla)A_0^P + (\nabla^2 \varphi_P)A_0^P = 0 \text{ and}$$

(2.43b)

$$\left[2(\nabla \varphi_P \bullet \nabla)A_n^P + (\nabla^2 \varphi_P)A_n^P\right] = -\nabla^2 A_{n-1}^P, n \geq 1$$

(2.43c)

(where (n-1) has been replaced by (n) for $n \geq 2$)

Through a similar expansion for the vector wave potential $\vec{\Psi}$

$$\vec{\Psi} = e^{ik_P \varphi_S(\vec{r})} \sum_{n=0}^{\infty} \frac{1}{(ik_S)^{n+1}} \vec{A}_n^S(\vec{r})$$

(2.44)

where $\vec{A}_n^S$ are now vector quantities, we would have

$$\left|\nabla \varphi_S\right|^2 = 1$$

(2.45a)

$$2(\nabla \varphi_S \bullet \nabla)\vec{A}_0^S + (\nabla^2 \varphi_S)\vec{A}_0^S = 0 \text{ and}$$

(2.45b)

$$\left[2(\nabla \varphi_S \bullet \nabla)\vec{A}_n^S + (\nabla^2 \varphi_S)\vec{A}_n^S\right] = -\nabla^2 \vec{A}_{n-1}^S, n \geq 1$$

(2.45c)

and since $\nabla \bullet \vec{\Psi} = 0$, we also have

$$\nabla \varphi_S \bullet \vec{A}_0^S = 0 \text{ and} \tag{2.45d}$$

$$\nabla \varphi_S \bullet A_n^S = -\nabla \bullet A_{n-1}^S, n \geq 1 \tag{2.45e}$$

We can now observe from equations (2.41) and (2.44) that the assumed solutions are such that $\varphi_P(\vec{r}) = \text{constant}$ and $\varphi_S(\vec{r}) = \text{constant}$ define wavefronts which are surfaces of constant phase. The spatial behaviour of the wavefronts is then governed by the *eikonal equations* given by (2.43a) and (2.45a). Rays are given by the vectors $\nabla \varphi_P$ and $\nabla \varphi_S$ which are curves normal to these wavefronts. The *transport equations* (2.43b-c) and (2.45b-d) govern the variation of wave amplitude with the position on the rays.

The properties of the phase and amplitude will be clearer when we examine the solutions to the eikonal equations and the lowest order transport equations. Let the parametric definition $\vec{r} = r(\vec{v}, S)$ with $\vec{v} = (v_1, v_2)$ represent a general family of wavefronts, with rays defined by fixed (v_1, v_2) and propagating along the unit normal $\hat{p}(v) = v_1 \times v_2$. Let (v_1, v_2) also be the principal directions of the surfaces $r(\vec{v}, S)$ and $q_k, k = 1,2$ be their principal radii of curvature[†] (see footnote). Then since $|\nabla \varphi|^2 = 1$ from the eikonal equation, we should have $\hat{p} = \nabla \varphi$ and since the directional derivative of φ in the direction of $\hat{p}$ is given by $\dfrac{\partial \varphi}{\partial S} = \hat{p} \bullet \nabla \varphi$, we obtain:

[†] The radii of curvature are intrinsic properties of any two-dimensional surface embedded in three-dimensional space. At any point Q on the surface $r(\vec{v}, S)$, let C_{ns} be the curve obtained from the intersection of the surface with a plane N containing the normal vector $\hat{p}$ and a tangent vector $\vec{w}$. C_{ns} then represents the normal section at Q and its curvature κ gives the normal curvature at that point. κ varies with the choice of the tangent vector, and its maximum and minimum values (κ_1, κ_2) are called the principal curvatures, whose negative reciprocals $(-1/\kappa_1, -1/\kappa_2) = (q_1, q_2)$ are the principal radii of curvature. The tangent lines corresponding to these principal radii are called the principal directions.

$$\frac{\partial \varphi}{\partial S} = 1 \text{ or } \varphi = S \qquad (2.46)$$

where S is the arc length measured on a ray, starting from the wavefront corresponding to the wavefront $\vec{r}_0(\vec{v})$ at $S = 0$.

With the help of the same set of arguments, it can also be shown that

$$\vec{r}(\vec{v}, S) = \vec{r}_0(\vec{v}) + S\hat{p}_0(\vec{v}) \qquad (2.47)$$

which shows that rays defined by fixed $\vec{v} = (v_1, v_2)$ are straight lines, propagating along $\hat{p} = \hat{p}_0(\vec{v})$.

Through Rodrigue's formula for rotation which gives $d\vec{r} = q_k \, d\vec{p}$ and making use of (2.47) we obtain,

$$\frac{\partial \hat{p}}{\partial v_1} = \frac{1}{q_1} \frac{\partial \vec{r}}{\partial v_1} \text{ and } \frac{\partial \hat{p}}{\partial v_2} = \frac{1}{q_2} \frac{\partial \vec{r}}{\partial v_2} \qquad (2.48)$$

with

$$q_k = q_k^0 + S, \, k = 1,2 \qquad (2.49)$$

where q_k^0 are the principal radii of curvature at S=0.

Equation (2.49) shows that the principal radii of curvature remain constant along a ray and increase linearly with distance on it.

Turning to the transport equations, the general lowest order transport equation is given by

$$2(\nabla \varphi \bullet \nabla) A_0 + (\nabla^2 \varphi) A_0 = 0 \qquad (2.50)$$

Using (2.46) and (2.47) we obtain $\nabla^2 \varphi = \dfrac{1}{q_1} + \dfrac{1}{q_2}$ and noting again that

$(\nabla \varphi \bullet \nabla) A_0 = \hat{p} \bullet \nabla A_0 = \dfrac{\partial A_0}{\partial S}$ the above equation (2.50) reduces to:

$$2\frac{\partial A_0}{\partial S} + \left(\frac{1}{q_1} + \frac{1}{q_2}\right)A_0 = 0 \tag{2.51}$$

The variable-separable solution can be written for (2.51) as

$$A_0(\vec{v}, S) = \frac{1}{\sqrt{q_1 q_2}} A(\vec{v}) \tag{2.52}$$

where as given by (2.49), $q_1 = q_1^0 + S$ and $q_2 = q_2^0 + S$

This completes our discussion of the ray theory: we find that wavefronts propagate along straight lines as given by equation (2.47), with the radii of curvature preserved and increasing linearly along them according to (2.49). The amplitude of the waves varies along the rays according to equation (2.52).

The standard ray theory involving reflection and refraction is well developed: the scattered fields are computed on reflected rays by tracing them back to the obstacle and applying the boundary conditions. As stated in chapter 1, these boundary conditions, of the nature of continuity conditions, lead to Snell's law governing the scattering behaviour. Following the analysis in this subsection in the light of equations (2.41) and (2.44) giving the representation of a wave as a ray and equations (2.47) and (2.52) governing its spatial evolution, incident rays of a type A (which can be P, SV or SH) are written as:

$$u^{inc} = \sqrt{\frac{(q_{1A}q_{2A})_S}{q_{1A}q_{2A}}} F_A(\vec{v}) \, \hat{P}_A \, e^{i\,k_A\,\varphi_A} \tag{2.53}$$

where the product $(q_{1A}q_{2A})_S$ has been evaluated on the plane S from which reflection or refraction is happening and $F(\vec{v})$ denotes the constant definition of the wavefront in the (v_1, v_2) plane; The unit vector $\hat{P}$ gives the polarization of the wave type, with $\hat{P}_A = \nabla \varphi_p$ for incident longitudinal waves and for shear waves, if $\hat{h}$ denotes a unit vector in the 'horizontal' direction, $\hat{P}_A = \hat{h}$ for SH waves and $\hat{P}_A = \hat{h} \times \nabla \varphi_p$ for SV waves.

Reflected and refracted rays of type B (which can again be P, SV or SH) are written in general as

$$u^r = u^{rP} + u^{rSV} + u^{rSH} \qquad (2.54a)$$

$$u^{rB} = \sqrt{\frac{(q_{1B}q_{2B})_S}{q_{1B}q_{2B}}} F_B(\vec{v})\, \hat{P}_B\, e^{i\, k_B\, \varphi_B} \qquad (2.54b)$$

$$F_B = R_A^B F_A \qquad (2.54c)$$

where R_A^B are the simple 'plane-wave' reflection and refraction coefficients, well known in literature (the reflection coefficients are summarized for example on p. 50 in [62] and Ch5 in [50]]

The other quantities on the reflected ray are related to those on the incident ray (which are assumed to be fully known) through the boundary conditions. If 'd_M' is the distance along a reflected ray from the point of reflection to the point of observation, by virtue of the Snell's law,

$$\varphi_B = d_M + \frac{c_B}{c_A}\left(\varphi_A\right)^S \qquad (2.55)$$

$\hat{P}_B$ are related to $\hat{P}_A$ again through Snell's law, and the radii of curvature on the reflected rays obtained by invoking the rotation formula (2.48). Further, on the plane S, the principal radii of curvature of the reflected/refracted rays are the same as those of incident rays.

For two-dimensional problems only one finite radius of curvature of the wavefront exists, which we call q: then (2.53) and (2.54b) further simplify to

$$u^{inc} = \sqrt{\frac{(q_A)_S}{q_A}} F_A(\vec{v})\, \hat{P}_A\, e^{i\, k_A\, \varphi_A} \quad ; A = P,\ SV\ or\ SH \qquad (2.56a)$$

$$u^{rB} = \sqrt{\frac{(q_B)_S}{q_B}} R_A^B F_A(\vec{v})\, \hat{P}_B\, e^{i\, k_B\, \varphi_B}; B = P,\ SV\ or\ SH \qquad (2.56b)$$

Kirchhoff approximation This standard geometrical ray theory can be used directly to solve elastodynamic scattering problems when the obstacles considered do not have sharp edges. By analogy to the well known geometrical optics, the results obtained this way are said to constitute the geometrical elastodynamics (GE) field. The GE field is quite accurate in describing certain problems such as backscattering from smoothly curved objects with a curvature larger than then incident wavelength. But when the edges of the object begin to have a strong influence leading to a sharply defined 'shadow', edge diffraction becomes important and standard ray theory becomes inadequate. A simple way to improve the accuracy is to use the GE field as an approximation for the total scattered field on the obstacle in the representation integral (2.28), yielding the elastodynamic version of the famous Kirchhoff approximation.

In the Kirchhoff approximation thus $\vec{u}^{tot} = \vec{u}^{ge}$: dividing the surface of obstacle into 'insonified' and 'shadow' regions, denoted by say S^{+} and S^{-} we will then have

$$\left(\vec{u}^{tot}\right)^{+} = \vec{u}^{inc} + \vec{u}^{r}; \ \left(\vec{u}^{tot}\right)^{-} = 0 \tag{2.57}$$

Equation (2.28) then yields for the scattered field,

$$u_k^{sc}(\vec{r}) = \int_{S^+}\left[\Sigma_{ij;k}(\vec{r}\mid\vec{s})u_i^{tot}(s) - \sigma_{ij}^{tot}(\vec{s})G_{i;k}(\vec{r}\mid\vec{s})\right]\cdot n_j dS \tag{2.58}$$

For stress-free cracks,

$$u_k^{sc}(\vec{r}) = \int_{S^+}\Delta u_i^{tot}(s)\left[\Sigma_{ij;k}(\vec{r}\mid\vec{s})\cdot n_j\right]dS \tag{2.59}$$

If the incident wave is given by (2.53), the reflected fields can be computed according to (2.54) noting that the radii of curvature of the scattered and incident rays on the scattering surface are the same in the GE theory. It will be useful to write the results for incident plane waves:

$$u^{inc} = I_o\,\hat{P}_A\,e^{i\,k_A\,\varphi_A} \ \ ; A = P, \ SV \ or \ SH \tag{2.60}$$

$$u^{r} = I_o R_A^P\,\hat{P}_P\,e^{i\,k_P\,\varphi_P} + I_o R_A^{SH}\,\hat{P}_{SH}\,e^{i\,k_S\,\varphi_S} + I_o R_A^{SV}\,\hat{P}_{SV}\,e^{i\,k_S\,\varphi_S} \tag{2.61}$$

From the general form of these results, we can see that mode-conversion effects and those of phase changes on the obstacle can be included in this method. This way, the Kirchhoff approximation models the scattering behaviour as if at each element of the scattering surface, incident plane waves interact with unbounded interfaces having the same normal. Like the Born approximation with which it shares a number of features, the Kirchhoff approximation has been used widely in scattering and inverse problems Achenbach (1979)[113] Chapman (1981, 1984) [61, 114] Schmerr (2002) [115]. The last quoted work [115] contrasts the Born and the Kirchoff approximations and comments on their limitations. Schmerr et al, 1989 [111] presented a framework unifying these two approximate methods.

The Geometrical Theory of Diffraction (GTD) The GE field has its limitations- it is discontinuous at the boundaries of shadows (defined by Snell's law) and vanishes totally in the shadow region. In reality, energy is continuously radiated into the geometrical shadow of the obstacle by waves which travel around its surface, causing 'diffraction'. The Kirchhoff approximation recovers the first singly diffracted field, but even this becomes incorrect in the presence of sharp edges. The Geometrical Theory of Diffraction (GTD) has been formulated to include the full effects of diffraction within the general framework of ray theory. Keller first developed the method rigorously for scalar waves and the method was later extended to elastodynamics by Resende (2D case) and in general by Achenbach and co-workers.

The GTD presents a correction to the total scattered field of the form:

$$\vec{u}^{tot} = \vec{u}^{ge} + \vec{u}^{d} \qquad (2.62)$$

The term $\vec{u}^{d}$ representing the diffracted field, offers only an insignificant correction to the GE field in the backscatter and specular directions, but contributes strongly in the forward direction; $\vec{u}^{d}$ itself is further constructed from components consisting of 'primary' or the first edge diffraction and 'secondary' or multiple diffraction:

$$\vec{u}^{d} = \vec{u}^{d}_{primary} + \vec{u}^{d}_{\sec ondary} \qquad (2.63)$$

These diffracted fields are constructed analogously to the reflected fields described in equations (2.53)-(2.56), with the scattered amplitudes related to the incident ones through 'Diffraction coefficients'. Appropriate 'canonical' problems (for example, for crack problems, the canonical problem is that of elastic wave scattering from a semi-infinite straight-edge crack; for scattering from convex surfaces, the canonical problem is that from infinite cylinders see [116]) whose solutions are known are selected and the Diffraction coefficients are obtained by comparing the ray solution with them. In the usual ray manner, the geometry and the curvature of the wave front as well as the defect are then incorporated through the edge conditions, which lead to the generalized Snells Law for diffraction.

2.3.3 Numerical methods

In the intermediate frequency regime, several numerical methods, including Finite Difference (FD) [117] [118] Finite element (FEM) [119-121] and t-matrix (see [79] for an excellent description of the t-matrix method) [122] [123-125] methods have been used. The Finite element method scores over the t-matrix method in that it can treat pulses in general and is not a single frequency method like the latter. Harumi and Uchida (1990) [126] provide a good review of various numerical studies, mainly the FEM. Numerical methods are very versatile in that they solve the scattering problem for any frequency regime and geometry and in this sense, can be seen more as experimental simulations than analytical solutions. A key issue though, is that they often don't provide generic results as they tend to be constructed for specific cases.

2.4 Guided elastic wave scattering

2.4.1 Exact solutions

Much of the development in guided wave scattering applications can be viewed as advancements based on the bulk wave methods. Guided elastic wave scattering problems

pose more challenges in their treatment because of the possibility of existence of several propagating modes even at low frequencies with increasingly complex, frequency dependent mode shapes and their mutual inter-conversion on interactions with flaws.

2.4.1.1 Wave function expansion method

If the defect boundaries lie along constant-coordinate surfaces of the rectangular, circular cylinder or spherical systems, it is still possible to use the method of eigenfunction expansion. One possible method is to express the guided wave modes directly in terms of eigenfunction expansions of the scalar and vector potentials. Alternatively, closer to the location of the defect, the scattered field could be expanded in the eigenfunctions of the wave equation in a suitable coordinate system, while away from the defect region, the field may be thought of as a sum of the possible guided wave modes. The different coefficients of expansion could then be determined from the boundary conditions and by considering continuity of fields throughout the medium.

Both these methods have been used in solving guided wave scattering problems occurring in different contexts. Grahn (2003) [127], Diligent (2002, 2003) [25, 26] have used the former method in studying the plate wave scattering from part and through cylindrical holes, in the context of NDE of corrosion defects. Castaings et al (2002) [128] have also used this method to study the interaction of low frequency Lamb modes with cracks. The latter method, sometimes called the 'mode matching' technique, has been used to study the interaction of Lamb and guided SH waves with long cylindrical defects axially perpendicular to the plane of propagation in the context of NDE of fibre-reinforced materials, building upon earlier work with bulk elastic waves [129, 130].

2.4.1.2 Integral equation method

Again, the reciprocity theorem along with the Green's function method could be an alternative route to guided wave scattering solutions. Auld and co-workers [74], [131] first sensed this and developed a normal mode theory (incorporating the orthogonality

relations) and proposed a variational solution in terms of the stress Green's function for an elastic plate. This method was subsequently used for a number of guided SH-wave scattering problems[120, 132-134] .

In his classical text, Auld [39] derived a generalized formula for scattering in plates from both volumetric defects and cracks using the S-parameter formalism and reciprocity arguments. As illustrated in Figure 2.5, if a time harmonic incident wave carrying power P is incident upon a scatterer inside in which the displacement (u) and stress (T) fields are indicated by subscript 2, and if the fields in the same region of the waveguide, had there been no scatterer be indicated by subscripts 1, then the S-parameter formalism yields **the scattering coefficients for a mode I to be reflected or transmitted into a mode R** as

$$\delta S_{I,R} = \frac{i\omega}{4P} \int_{S_F} (u_{1R} \cdot T_{2I} - u_{2I} \cdot T_{1R}) \cdot \vec{n} dS \tag{2.64}$$

For crack-like defects, because the normal traction vanishes, this yields:

$$\delta S_{I,R} = \frac{i\omega}{4P} \int_{S_C} \Delta u_{2I} \cdot T_{1R} \cdot \vec{n} dS \tag{2.65}$$

where Δu again is the usual crack opening displacement (COD).

It is possible to convert the above equation into a volume integral formulation:

$$\delta S_{I,R} = \frac{i\omega}{4P} \int_{V_F} \nabla \cdot (u_{1R} \cdot T_{2I} - u_{2I} \cdot T_{1R}) dV = \frac{i\omega}{4P} \int_{V_F} (\Delta\rho\omega^2 u_{1R} \cdot u_{2I} + T_{2I} : \Delta s : T_{1R}) dV$$

$$\tag{2.66}$$

It is not difficult to see that these results are similar to the results for the bulk waves presented in equations (2.27)-(2.31). Ditri (1994) [135] later extended this derivation for the more complex case of guided wave scattering from circumferential cracks in hollow cylinders.

2.4.2 Approximate analytical methods

Because of the limited number of problems that can be solved exactly and the larger difficulties posed by the guided wave case, approximate methods have played a large part in the analysis of guided wave scattering problems.

2.4.2.1 Approximations following from the Integral Equation method

Even at an early stage of development of guided wave methods, Auld and co-workers proposed the usage of the quasi-static approximation (described earlier for the bulk elastic wave case), valid in the low-frequency limit. Therefore most of the works quoted using the reciprocity approach (including Tan and Auld [131] Fortunko [132] and Ditri [135]) arrived at a quasi-static solution to the problems they considered. Tien et al [136] applied this method to scattering of surface waves from cracks and flaws.

Following the work of Ditri (1994) [135], Lowe and co-workers applied the method to a number of guided elastic wave crack scattering problems and provided important insights. In Alleyne et al (1998) [42], they clarified the validity of the quasi-static application in the light of an incorrect derivation by Ditri for the variation of the reflection coefficient of the L (0, 2) mode with the circumferential extent of a crack. In Lowe et al (1998) [40], they constructed the reflection coefficient variation with the assumption of a simple profile for the Crack opening displacement (COD), that agreed very well with their experimental and FE predictions.

In Lowe and Diligent (2001) [27, 28], they used arguments based on the low-frequency quasi-static approximation and the high-frequency Kirchhoff approximation to conclude that the Lamb wave scattering problems at frequencies used for inspection purposes are in a regime where neither of these are strictly valid. But the transition from Low-frequency to high-frequency behaviour could be observed extremely well in terms of the limiting values provided by the two approximations. It is interesting to note that in estimating the static COD, they considered a long crack case and used the results from

fracture mechanics literature and interpolations. In the light of the discussion of the equivalent approximation in the bulk wave case, their analysis could be extended to elliptical, circular and needle cracks as well, and fruitful conclusions be drawn. Also, in the off-specular directions, the Geometric theory could provide useful approximations.

Additionally, Rokhlin (1980) [137] also proposed the use of a modified Wiener-Hopf technique on the lines of that of Maue (as quoted in [114]) for the bulk elastic wave case to study of the diffraction of Lamb modes from a class of cracks parallel to the plate surface.

2.4.2.2 Approximations using the Wave function expansion method

Other approximate methods suitable to the wave function expansion method have also been proposed in the literature. Typically, they seek to reduce the complexity of the problem by using some of the available higher order plate theories [127]. Norris and Vemula (1995, 1997) [138, 139] studied the scattering of antisymmetric (flexural) modes from circular inclusions in plates using the Mindlin and the Kirchoff plate theories. Andronov and Belinskii (1993) [140] used the Kirchoff theory to study the diffraction of flexural waves by a crack in an elastic plate. McKeon and Hinders (1999) [141] used the Kane-Mindlin extensional theory to study the scattering of low frequency S0 waves from circular inclusions in plates. Fromme and Sayir (2002) [142] provided experimental confirmation for the validity of Mindlin plate theory in this regime. Chun and Chang (2004) [143] provide a good review of literature in this regard. Recently, Wang and Rose (2003) [144] have proposed to use the Mindlin plate theory as an effective model for damage detection in tomographic applications.

2.4.3 Numerical methods

In addition to the above methods, numerical methods (FEM, BEM) too have played a vital role in the study of guided wave scattering problems and the work of Cawley and co-workers [25] [22, 27-29, 40, 145, 146] and Rose and co-workers has led to the

understanding of the fundamentals of low-frequency guided wave interactions with defects. Rose (2002) [147] provides an excellent review of guided wave scattering studies. Again though they serve as versatile simulation tools applicable to different frequency regimes and geometries, an issue with numerical methods is that they tend to be primarily concerned with specific rather than generic results.

2.5 Conclusions

This chapter reviewed the basics of the theory of guided elastic wave scattering in order to identify methods which can be used to illuminate the physics behind the results obtained through the rest of the thesis. First the well-known link between bulk and guided elastic wave scattering was pointed out, and this helped see how techniques in treating the latter originate in and developed from the former. Differential- and integral-equation based methods in bulk wave scattering were then introduced: the integral equation formulation is more intuitive as it gives a direct mathematical representation of the Huygens's principle.

An important route to integral representations is through the elastodynamic reciprocity theorem which yields integral formulas for scattering. This formulation also provides a convenient starting point for a number of approximate analytical methods: the Born, quasi-static and extended quasi-static approximations at low frequencies and the Geometric Theory of Diffraction (GTD), Kirchhoff and uniform COD approximations at high frequencies are widely used. The Kirchhoff approximation is among the simplest, yet it is quite accurate at high frequencies and in the backscattering direction - especially close to the specular direction [61] and recent research [148] shows a much wider applicability- and can form the basis for a simple analytical treatment of the scattering of guided waves. Examples of such treatment can be found in the following chapters of this thesis.
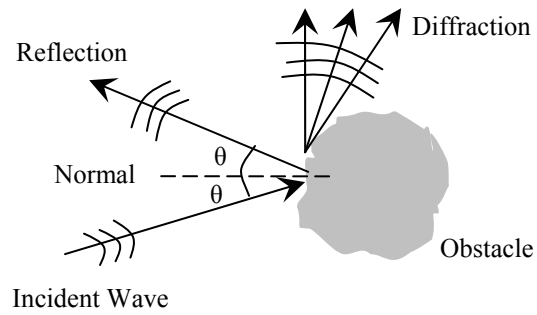
Figure 2.1 Waves reflect back from obstacles and also diffract near their boundaries.
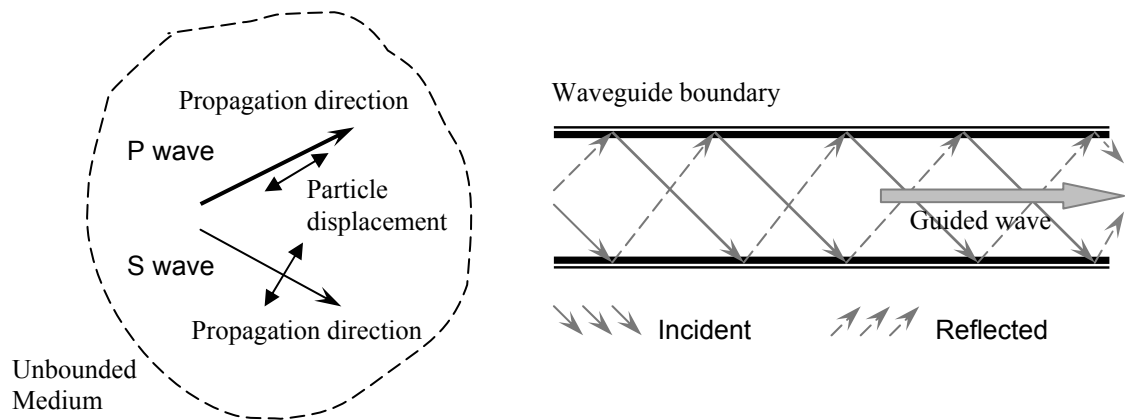
Figure 2.2 By means of repeated reflections boundaries have the effect of guiding waves along the structure, and their superposition eventually gives rise to different guided wave modes.
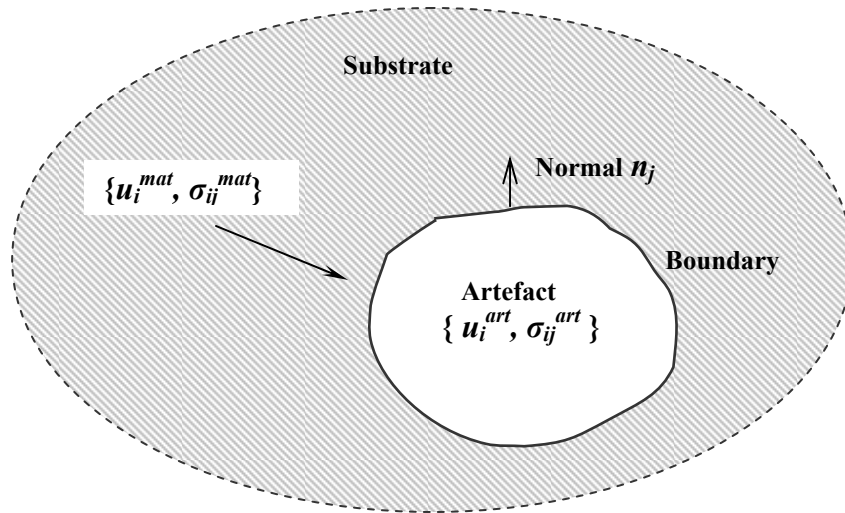
Figure 2.3 The elastic wave scattering problem
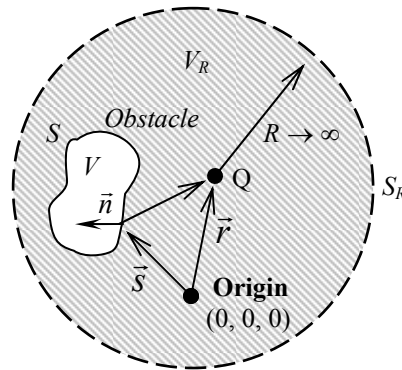
Figure 2.4. An obstacle by a surface S with unit outward normal $\vec{n}$ is enclosed by a large region of outer surface S_R.
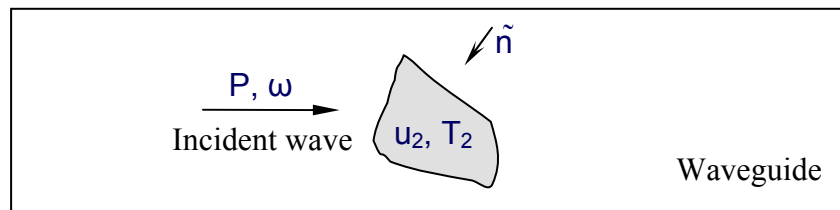
Figure 2.5 Time harmonic incident wave carrying power P is incident upon a scatterer in a waveguide inside which the displacement (u) and stress (T) fields are indicated by subscript 2

Chapter 3

High frequency-thickness regime

3.1 Introduction

The discussion in Chapter 1 showed that the fall in sensitivity due to the long wavelengths used and the inability to discriminate deep defects from shallow ones is an important problem affecting the resolution achievable by current inspection techniques. This chapter examines the high frequency multimode approach from this perspective. Specifically, it seeks to answer whether the shorter wavelengths lead to higher reflections for small defects and if a scattered field consisting of many modes provides more information about the defect than a single mode response. For simplicity the defect type of a planar crack is taken up and only one fundamental mode is assumed in the incident field but relatively high frequencies are used to excite a multiple mode scattered response. The interaction of the fundamental antisymmetric Lamb mode A0 with long surface cracks in plates and that of the axially propagating fundamental Torsional mode T(0,1) with full-circumference surface cracks in thin pipes are considered separately. The interaction is studied in terms of the influence of the crack depth on the reflection amplitude. In the following sections, first the configuration studied is introduced and then the procedure for Finite Element (FE) simulations is described. The results are validated by comparison with those from similar problems in literature and theoretical analysis and then discussed in the light of resolution issues.

3.2 Configuration studied

Figures 3.1 (a) and 3.1 (b) show the configurations studied in the plate and the pipe studies respectively. Treating a plate as an unwrapped pipe, an ideal circumferential crack of vanishing axial extent is located in the cross-sectional plane of an isotropic plate or thin pipe, breaking the outer surface and running through part of the thickness. Plane waves of the incident mode reflect into all possible propagating modes that can exist at the operating frequency. The frequency domain ratio RC of the displacement amplitude of each reflected mode measured in a given direction, to that of the incident mode in the same direction is calculated, and the influence of the crack depth on the modulus of this ratio is examined at particular frequencies. The energy carried by a reflected mode whose modal amplitude in the direction chosen for the calculation of RC differs from that of the incident mode by a ratio ξ will be given by $(\xi \cdot RC)^2$ (see for *e.x.*, [128]).

With plates, the relatively low dispersion of Lamb modes around the peaks or dips of the group velocity dispersion curves makes them ideal for choice of the operating frequency. As shown in shown in Figure 3.2, suitable regions could for instance be around 2.5 MHz-mm, coinciding with the peak for the A1 mode, and a dip for the S0 mode, or 4.0 MHz-mm coinciding with the group velocity peak for the S1 mode. In the present work, the plate studies were carried out at two frequency-thickness values: at 2 MHz-mm just after the A1 cut off frequency and at 2.5 MHz-mm coinciding with a group velocity peak and dip for the A1 and S0 modes respectively.

The torsional modes in a thin pipe correspond to shear horizontal modes (SH) in a plate and this point will be referred to again, in a later section of the chapter. Figure 3.3 shows the group velocity dispersion curves for axially-propagating torsional modes in a 1 mm thick Aluminium pipe of 20 mm inner radius. They can be seen to be almost identical to those of the SH modes in an Aluminium plate shown in Figure 1.4. Figure 3.4 further illustrates this identity by comparing the displacement mode shapes of the first three Torsional and Shear Horizontal modes in these two structures.

As there are no peaks or dips in the dispersion curves of torsional modes, the pipe study was simply carried out at 4.0 MHz-mm, above the cut-off frequency of the T(0,3) mode.

3.3 Procedure for Finite Element simulations

3.3.1 A0 mode at high frequency-thickness

Figure 3.5 depicts the procedure for the FE simulations for the plate studies along with the coordinate axes. The long cracks mean that fields in the plate vary only along U1-U3 cross-sectional plane perpendicular to the crack and Lamb modes have particle displacement solely along this plane. This allowed the plate to be modelled in a two-dimensional domain, with the assumption of plane strain, using standard elements available in the Finite Element package ABAQUS [149]. This means that in effect, a section perpendicular to the surface of the plate and along the propagation direction is modelled**.**

Properties of aluminium were used for the model plate which was 1 mm thick and 450 mm long. A vertical, surface breaking crack was located at 300 mm from one end of the plate. These values were selected to minimise the run time for the simulations. The mesh consisted of perfectly square elements with 20 of them through the plate thickness so that the different crack depths could be accurately described. This allowed around 24 elements per wavelength at the highest frequencies used, well above the lower limit of spatial discretization required for accurate modelling [42, 146]. Cracks were created by disconnecting elements along the line defining them. A large number of models were set up to obtain cracks of different depths.

With the time domain excitation given by a Hanning windowed toneburst of a certain number of cycles and centred at the required frequency, the input displacement histories could potentially be obtained from either the 'Pure Mode Shape' or the 'Centre Mode Shape' method [150]. The Pure Mode Shape method imposes the exact mode shape at all frequencies in the bandwidth of the signal. The Centre Mode Shape method on the other

hand, imposes the mode shape only at the centre frequency of the signal and if required, a toneburst with large number of cycles is used to confine the bandwidth around the centre frequency. The mode shape of the incident A0 mode varies only a small amount and very gradually between 2-3 MHz-mm. Thus a narrow bandwidth signal given by a 50-cycle Hanning windowed toneburst along with the Centre Mode Shape method was enough to provide the time domain excitation. The large numbers of cycles also helped to lessen the effect of dispersion in the reflected S0 and the A1 modes. This was applied as a displacement boundary condition at all nodes on one end of the plate, in both the U1 and U3 directions, with the amplitude scaled suitably to match the mode shape at the centre frequency. The two in-plane displacement components of the A0 mode differ in phase by $\pi/2$ (see for *e.x.*, [27]). Without loss of generality, the U1 displacement component was assumed to have zero phase. Therefore the toneburst for the U3 direction was defined to lag behind that for the in-plane U1 direction by $\pi/2$. Explicit time integration was used, with a constant time increment given by the stability limit of 0.8 *L/C*, where *L* is the element length and *C* is the speed of the fastest wave present [27]. This simulates the propagation of a straight-crested (plane) wave along the plate. The default condition on the faces of the disconnected elements representing the crack is that of zero stress. Thus the scattering from an ideal open crack is simulated.

The reflected wave packet contains the reflected A0 mode, as well as the other plane strain modes existing at the operating frequency-thickness, generated by mode conversion of the A0 mode incident at the crack. In principle, long models can be used to separate out the different modes in time, using differences in their group velocity, but this makes the models large and increases the time for completion of each simulation run. Therefore a two-dimensional FFT [151] was used to achieve the separation of modes differing in wave number. The out-of-plane U3 displacement was monitored at 128 locations along the top surface of the plate, starting from a point 150 mm from the left end. The large number of monitoring points was required to obtain clear separation of the different modes in the wavenumber domain. A typical monitored signal for the case of incidence of the A0 mode at 2.5 MHz-mm is shown in Figure 3.6: we see the incident A0 wave and the reflected packet containing, A0, A1 and S0, the three plane strain modes

which can exist at 2.5 MHz-mm. Because of the small difference in the group velocities of A0 and A1 modes at this frequency, they arrive almost together. Figure 3.7 shows the two-dimensional FFT of the reflected signals for the 2.5 MHz-mm case and the different modes in Figure 3.6 can now be seen well separated.

The signals were processed in the frequency domain to obtain the reflection coefficients. Since the study was carried out using signals with very narrow bandwidth, the results are valid only around the centre-frequency of the incident mode. Therefore different sets of simulations were necessary to obtain the predictions for the 2 MHz-mm and 2.5 MHz-mm cases.

3.3.2 T(0,1) mode at high frequency-thickness

Figure 3.8 illustrates the procedure for the FE simulations for the pipe study along with the coordinate system. The torsional modes have particle displacements perpendicular to an axial section of the pipe, so a 2D model describing them would require axisymmetric elements with out-of-plate motion (twist) which ABAQUS/Explicit does not offer. In order to avoid a fully three-dimensional model at this stage, the Finite Element package FINEL [152] which offers such elements and with which the NDT Group has extensive experience, was used for the calculations.

A 1 mm thick, 240 mm long Aluminium pipe with an inner radius of 20 mm was modelled to obtain the FE predictions of reflections. A surface breaking crack spanning the pipe's entire circumference was located at 140 mm from one end of the model pipe. As with the plane strain studies, these values were selected to minimise the run time for the simulations. The symmetry in the system allowed the pipe to be modelled in the radial-axial two-dimensional domain, by using linear axisymmetric elements with twist. The mesh consisted of 20 perfectly square elements through the pipe thickness, allowing around 16 elements per wavelength at 4 MHz-mm, respecting the spatial discretization limit for accurate modelling. Cracks were again created by simply disconnecting the nodes common to elements on their adjacent faces.

A 50-cycle Hanning windowed toneburst was used to provide the time domain excitation, applied as a displacement boundary condition at all nodes on one end of the pipe wall, in the out-of-plane U_θ direction, with the amplitude matching the mode shape of the T(0,1) mode at the centre frequency. Since the T(0,1) mode is nondispersive, this launches a pure mode into the pipe. Explicit time integration with a constant time increment given by the stability limit simulates the propagation of a plane wave along the axis of the pipe and its scattering from the crack.

Since the geometry and loading are axially symmetric, there is no mode conversion between modes of different circumferential orders, and only modes of the same order as the excitation signal can propagate. Therefore the reflected wave packet contains only torsional modes, the T(0,1) mode, and the T(0,2) and T(0,3) modes generated by mode conversion at the crack. Processing by two-dimensional FFT was again used to achieve the separation of modes differing in wave number. The reflection coefficient was obtained by the same procedure as for the A0 case, as the frequency domain ratio of the peak amplitude of the respective reflected signal to that of the incident signal.

3.4 Results and discussion

3.4.1 A0 mode reflection studies

First the modelling procedure was sought to be verified: for this purpose, the interaction of the A0 mode at 1.5 MHz-mm with normal cracks in a steel plate was studied, so that the results could be compared with those from earlier work at the NDT Group [27, 28]. Figure 3.9 shows the variation of the A0/A0 reflection coefficient with crack depth at 1.5 MHz-mm, obtained from the present procedure as well as that reported in [27]. Very good agreement is observed between the two sets of results.

The variation of reflection coefficient with crack depth was then obtained separately at 2 MHz-mm and 2.5 MHz-mm. Figures 3.10 and 3.11 show the graphs for these two cases respectively.

These trends are known to come about from the way the crack opens in response to the incident mode and the stress distribution of the respective reflected modes. A simplistic treatment will not fully capture this complex phenomenon: in what follows, a simple theoretical analysis is presented to gain physical insight rather than an accurate solution. Following earlier studies at the NDT Group [27, 41, 153] based on the S-parameter technique [39], the reflection coefficient (RC) of a mode of interest from an ideal crack can be expressed in terms of a parameter capturing how the crack opens in response to the incident mode, the Crack Opening Displacement (COD), and the significant stress components of the reflected mode. For the plane-strain problem studied here, the reflection coefficient can be expressed as

$$RC = \frac{i\omega}{4}\int_S [COD_{axial} \cdot \sigma_{11} + COD_{shear} \cdot \sigma_{13}]dS \qquad (3.1)$$

where the amplitude of both the incident and the reflected modes is defined to be such that they transmit unit power flow per unit cross-sectional area of the wave guide, ω is the circular frequency, COD_{axial} and COD_{shear} stand for the displacement jump across the crack faces in the axial and in-plane shear directions respectively due to the incident A0 mode, the axial stress σ_{11} and the in-plane shear stress σ_{13} are the significant stress components of the reflected Lamb mode of interest- A0, S0 or A1, and the integral is calculated over the whole of the surface area of both sides of the crack.

We then invoke the Kirchhoff approximation, which assumes that the faces of the crack do not interact and therefore the COD is just the displacement on the insonified face, which is twice the incident displacement. Such an assumption is known to be accurate at high frequencies and particularly at near-specular reflection directions [61] and recent research [148] shows a much wider applicability. From equation (3.1) then the modulus of the reflection coefficient would be

$$|RC| \approx \left| \frac{i\omega}{4} \int_{S^+} [2u_1 \cdot \sigma_{11} + 2u_3 \cdot \sigma_{13}] dS \right| = \frac{\omega}{2} \left| \int_{S^+} [u_1 \cdot \sigma_{11} + u_3 \cdot \sigma_{13}] d\ell dz \right| \quad (3.2)$$

where u_1 and u_3 are incident displacements in the U1 and U3 directions on the insonified face of the crack S^+, and ℓ and z are dummy elements along its length and depth.

We can then observe the vital role of the displacement mode shapes of the incident A0 mode and the stress mode shapes of the reflected modes in shaping the reflection behaviour. Figure 3.12 shows the displacement mode shapes for the A0 mode and the stress mode shapes for A0, A1 and S0 modes at 2 MHz-mm and 2.5 MHz-mm. The stress mode shapes of both the antisymmetric modes are similar at the two frequencies, but with the A0 mode, the σ_{13} stress quickly reaches a constant value starting from a zero value at the plate surfaces, while with the A1 mode it only gradually reaches a peak value at the mid-plane, tapering off on either side. The displacement mode shapes of the incident A0 mode are again similar at the two frequency-thickness values, with the U1 displacement strong near the plate surfaces but vanishing near its centre, while the U3 displacement is nearly constant through the plate thickness. We can see from equation 3.2 that the U1 mode shape of the incident mode modifies the reflected mode's σ_{11} modeshape and U3 modifies σ_{13}. We can thus note that for these two modes, both σ_{11} and σ_{13} mode shapes are important for very short and very deep cracks, but in general the reflection is dominated by the latter.

We conclude that the reflections of the A0 and A1 modes display similar trends at 2.0 MHz-mm and 2.5 MHz-mm and are mutually different from each other, because of the likewise behaviour of their σ_{13} modeshapes. The σ_{11} mode shape of both modes become more complex and fall more quickly to zero from the surface to mid of the plate, at 2.5 MHz-mm than at 2 MHz-mm. The smoother variation of the A0 reflection coefficient with depth and the flatter rise in the A1 reflection coefficient at 2.5 MHz-mm against the 2 MHz-mm case as observed from Figures 3.10 and 3.11 seem to bear these changes out.

The situation with the S0 mode is much more complicated but we note that while the trend of its σ_{13} mode shape is almost unchanged, the σ_{11} mode shape at 2.5 MHz-mm has zero-crossings and is therefore very different from the simple convex form at 2 MHz-mm. This strongly contributes to changing the shape of S0 reflection coefficient from the simple convex form at 2 MHz-mm to the cyclical pattern exhibited at 2.5 MHz-mm.

In terms of expected reflection behaviour, there should be no conversion to the S0 mode at the trivial case of a zero-depth crack, and also at through-cracks because of the thickness-wise symmetry. We see from Figure 3.11 that at 2.5 MHz-mm, additional regions where there is minimum mode conversion to the S0 mode are also revealed in the shallow and deep crack regimes. Such findings are important for characterization studies, as we will discuss in Section 3.4.3.

3.4.2 T(0,1) mode reflection studies

For the pipe case, as noted in Section 3.2, the problem studied here is identical to that of high frequency SH0 mode interaction with long cracks in plates. This latter problem has been studied in the past [121, 154] and results are compared for a qualitative validation of the modeling procedure. Figure 3.13 presents the reflection coefficient results at 4 MHz-mm from the present FE simulations. Figure 3.14, reproduces a sample result from Abduljabbar *et al.* (Figure 7 in [121]) for the case $k_s h = 9.0$ corresponding approximately to a frequency-thickness of 4.5 MHz-mm. We observe that the trends in Figure 3.13 for the reflection coefficients of T(0,1) , T(0,2) and T(0,3) modes for T(0,1) incidence at 4 MHz-mm agree very well with those of SH0, SH1 and SH2 modes for SH0 incidence presented in Figure 3.14 at similar frequencies. The reflection of both T(0,1) and SH0 increases almost monotonically with crack depth, that of both T(0,2) and SH1 displays a convex increase-decrease with a peak occurring for a 50% deep crack and that of both T(0,3) and SH2 displays a more complex cyclical behaviour, with a dip occurring again for a 50% deep crack.

The explanation for this kind of reflection behaviour is again linked with the mode shapes of the displacement and significant stress components of the incident and reflected modes. Using the S-parameter formalism, the modulus of the reflection coefficient in this case can be written with similar notation as in Section 3.4.1, as:

$$|RC| = \left| \frac{i\omega}{4} \int_S [COD_{shear} \cdot \sigma_{z\theta}] dS \right| \tag{3.3}$$

where COD_{shear} now stands for the displacement jump across the crack faces in the out-of-plane shear direction due to the incident T(0,1) mode and $\sigma_{z\theta}$, the out-of-plane shear stress is the only significant stress components of the reflected torsional modes. Again, the amplitude of the fields in both the incident and the reflected modes are defined to be 'power normalized' [135].

The Kirchhoff approximation yields a simplified expression

$$|RC| \approx \left| \frac{i\omega}{4} \int_{S^+} [2u_\theta \cdot \sigma_{z\theta}] dS \right| = \frac{\omega}{2} \left| \int_{S^+} [u_\theta \cdot \sigma_{z\theta}] d\ell dz \right| \tag{3.4}$$

where ℓ and z are dummy elements along the crack's circumferential extent and depth or radial extent in the pipe cross-section and S^+ is insonified face of the crack.

Figure 3.15 shows the U_θ modeshape for the incident T(0,1) mode and the $\sigma_{z\theta}$ modeshape for the T(0,1), T(0,2) and T(0,3) modes at 4 MHz-mm. Noting that U_θ for T(0,1) mode is nearly constant along the pipe thickness, it is easy to see that nearly linear increase of the T(0,1) reflection coefficient comes from its nearly constant $\sigma_{z\theta}$ mode shape. Similarly the convex shape of the T(0,2) reflection coefficient and the more complex cyclical variation in that of the T(0,3) mode can be seen to originate from the similar behaviour of their $\sigma_{z\theta}$ mode shape, whose integral over the crack depth determines the reflection, as observed from equation (3.4).

From the trend of reflections in Figure 3.14 we infer that there will be no mode conversion to the higher order modes at through-thickness cracks – this is confirmed from an examination of Figure 3.15 also. This is an important observation and its significance is discussed in more detail in the next section. Further, the three torsional modes considered do not change their mode shape at different frequencies, only their relative magnitudes are scaled. This means that this same reflection-crack depth behaviour can be expected at all frequency-thickness values up to the cut-off frequency of T(0,4) mode at around 4.7 MHz-mm, although the energy partition between the 3 modes will not be the same.

3.4.3 Implications for improving resolution of guided wave NDE

We will now examine these findings from the perspective of resolution issues with practical inspection. Firstly as we noted in Section 1 of this chapter, we ask whether the scattering at higher frequencies is more sensitive to the crack depth for shallow cracks than at low frequency thickness. Figure 3.16 compares the A0 reflection coefficient variation with crack depth at 1.5, 2 and 2.5 MHz-mm respectively, together with the average reflection coefficient for all modes occurring at 2 and 2.5 MHz-mm. We observe that while the reflection values at both the higher frequencies are higher than at 1.5 MHz-mm, the reflection rises much more quickly with the crack depth in the shallow crack region only at 2.5 MHz-mm. From the point of view of discrimination, the A0 and A1 modes appear to be the 'best modes' with a uniform relation of reflection amplitude with the crack depth. For the pipe study, an examination of the reflection coefficient values from Figure 3.13 and those from earlier low-frequency studies from Demma *et al.* [19], reproduced in Figure 3.17 shows that in this case, the rise is even stronger in the shallow crack region. The T(0,1) mode is clearly the 'best mode', with a nearly linear increase of its reflection with the crack depth and scoring better than the average reflection.

The other question we set out to answer was whether the mode-conversion patterns offers any additional information regarding the crack depths, so that we can distinguish deeper cracks from shallow ones. As discussed in Chapter 1, planar cracks in practical situations

would have a finite crack depth as well as length or circumferential extent and sometimes it becomes difficult to distinguish between shallow and deep cracks based just on reflection coefficient measurements. Thus it would be useful if we can obtain an additional parameter which varies monotonically with the crack depth over all the depth regimes. But even parameters which can give strong information in chosen regimes could prove valuable. As we can see from Figures 3.10, 3.11 and 3.13, the amplitude of the different modes in the reflected packet vary very differently with crack depths. In Figure 3.10, while A0 and A1 mode reflection continually increases, the S0 reflection tends to flatten out with the crack depth. In Figure 3.11, again while the A0 and A1 mode reflection is quite similar, the S0 mode has cyclical variation with the crack depth. Finally in Figure 3.13 we see that the reflection behaviour of all the three torsional modes is mutually different.

Thus a measure of the scatter between the reflection coefficients of the different modes could be the parameter we are seeking; the standard deviation between them is taken as this measure. (Studies of other variations for example, the standard deviation normalized to the average values did not yield better results). Figures 3.18 (a) and (b) show the standard deviation between the reflection coefficients of A0, S0 and A1 modes at 2 and 2.5 MHz-mm respectively, plotted with crack depth and 3.18 (c), shows the same for T(0,1) , T(0,2) and T(0,3) modes at 4 MHz-mm. From figures 3.18 (a) and (b) we note that the uniformly rising scatter at 2 MHz-mm, is more useful in obtaining depth information for most cracks, whereas the cyclical variations at 2.5 MHz-mm mean that the scatter is useful only in parts. This also suggests that with Lamb modes, an increase in the frequency of operation does not naturally lead to better discrimination between different crack depth regimes. On the other hand from Figure 3.18 (c) we see that the scatter between the amplitudes of different torsional modes increases uniformly with the crack depth. Considering that similar reflection behaviour is expected with these torsional modes at all frequencies below the T(0,4) cut-off, operating at higher frequencies is in general beneficial with this family of modes.

Another way of distinguishing different crack depth regimes would be to make use of the information about regions of little or no mode-conversion. With torsional modes, this could be a straightforward way to distinguish middle-sized cracks where all three modes are present, from shallow and very deep ones, where T(0,2) and T(0,3) modes tend to vanish. Similarly the different crack depth regimes in a plate can be separated from S0 mode-conversion information.

3.5 Conclusions

FE analysis has been used to study the interaction of the A0 and T(0,1) modes with simple defects in flat plates and hollow cylinders at higher frequencies. A simplified analytical treatment was used to gain insight into the influence of the mode shapes of the dominant stress components on the reflection behavior. The correspondence of the torsional modes in pipes with shear horizontal modes in plates was discussed, and results from the T(0,1) case seem to be valid for the identical SH0 problem. The key objectives in shifting to higher operating frequencies are the desire to increase the sensitivity of reflection to smaller defects and to better distinguish thickness-wise deep defects from the shallow ones.

From the former perspective, the reflection behaviour due to A0 and T(0,1) mode incidence at long cracks is beneficial, although for the A0 mode the frequency must be carefully chosen. Again mode conversion effects at higher frequencies do not seem to naturally lead to better discrimination with the A0 mode case as compared to the T(0,1) case. Here we have not considered the effects of dispersion and that of similar velocities for multiple modes- this could mean that in practice, the different modes cannot be separated as we have assumed in this chapter. Further the behaviour with smaller, fully 3 dimensional cracks, will present more complications and it has to be verified if similar reflection behaviour is retained. These issues have to be considered when assessing the merits of this approach vis-à-vis the low frequency approach.
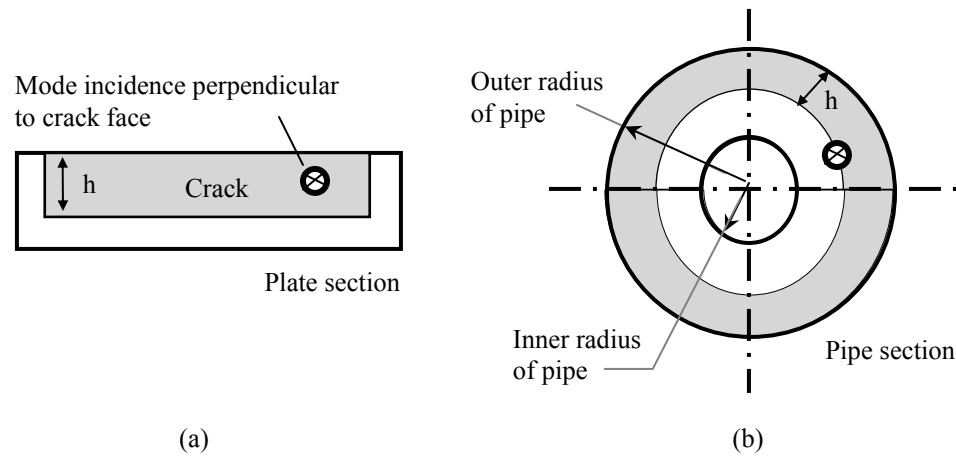
Figure 3.1 Configuration studied: (a) Plate cross-section, A0 mode is incident normally on a long surface-breaking part-depth crack (b) Pipe cross-section, T(0,1) mode is incident normally on a surface-breaking full-circumference part-depth crack; the pipe thickness (= Outer radius - inner radius) is shown exaggerated.
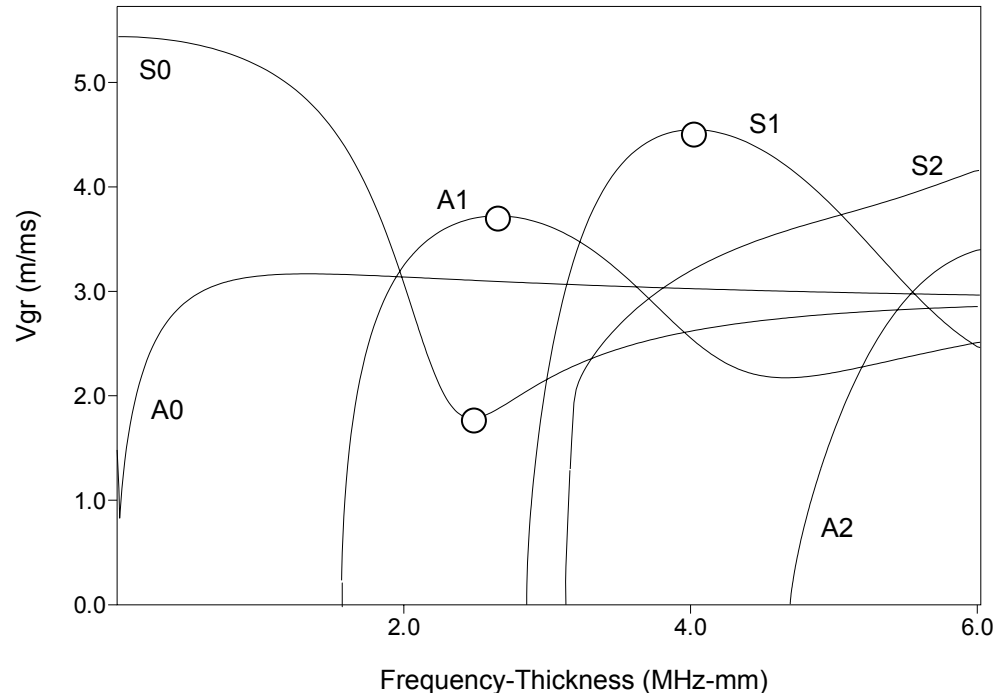
Figure 3.2 Peaks and dips of the Lamb wave group velocity dispersion curves (shown here for an aluminium plate) where dispersion is relatively low.
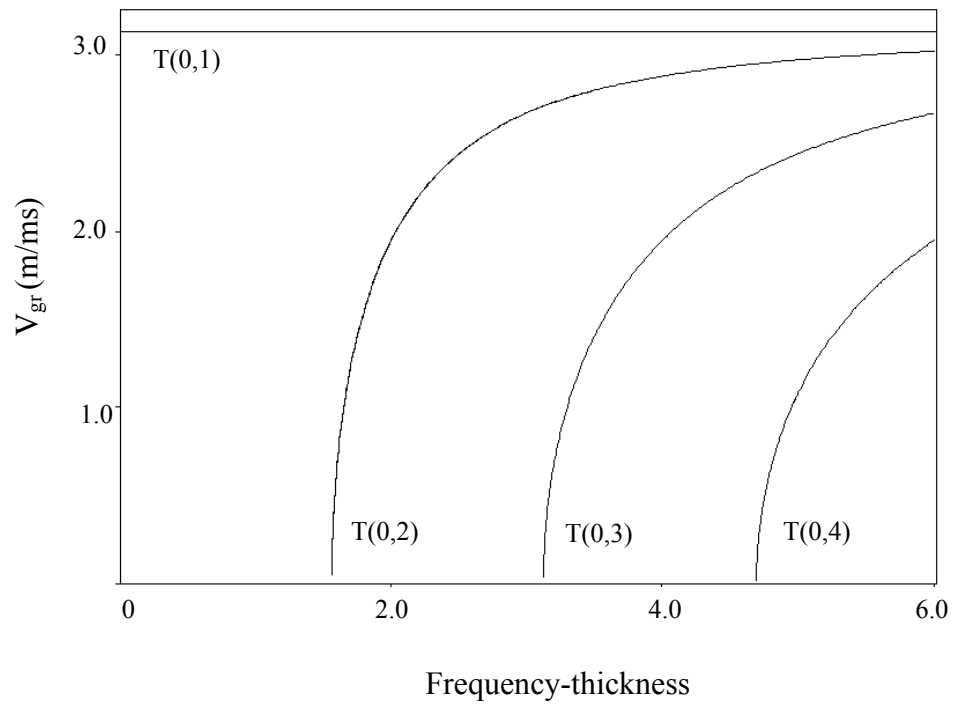
Figure 3.3 Group velocity dispersion curves for axially-propagating torsional modes in a 1 mm thick Aluminium pipe of 20 mm inner radius.
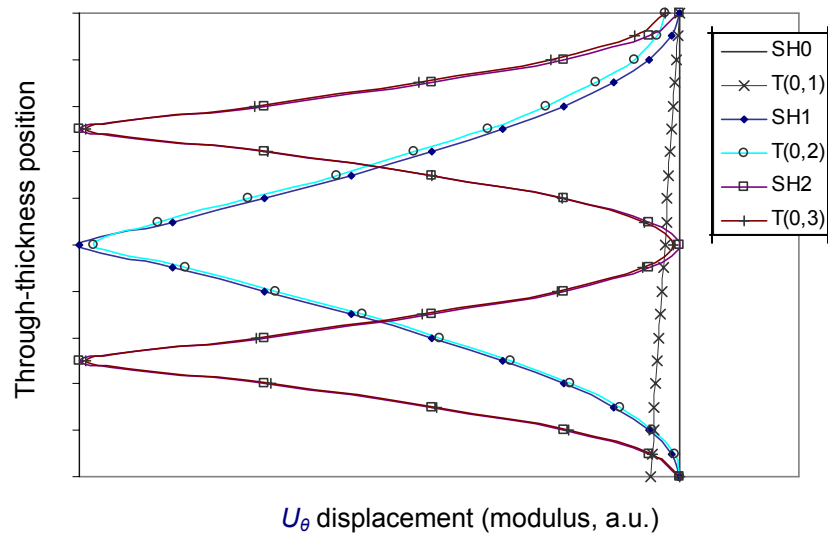
Figure 3.4 Absolute values of the displacement mode shapes of the first three Shear Horizontal (SH) modes at 4 MHz-mm in a 1mm thick aluminium plate and those of the first three axially propagating Torsional (T(0,n)) modes at 4MHz in a 1mm thick Aluminium pipe of 20 mm inner radius; the U_θ direction is indicated in Figure 3.8.
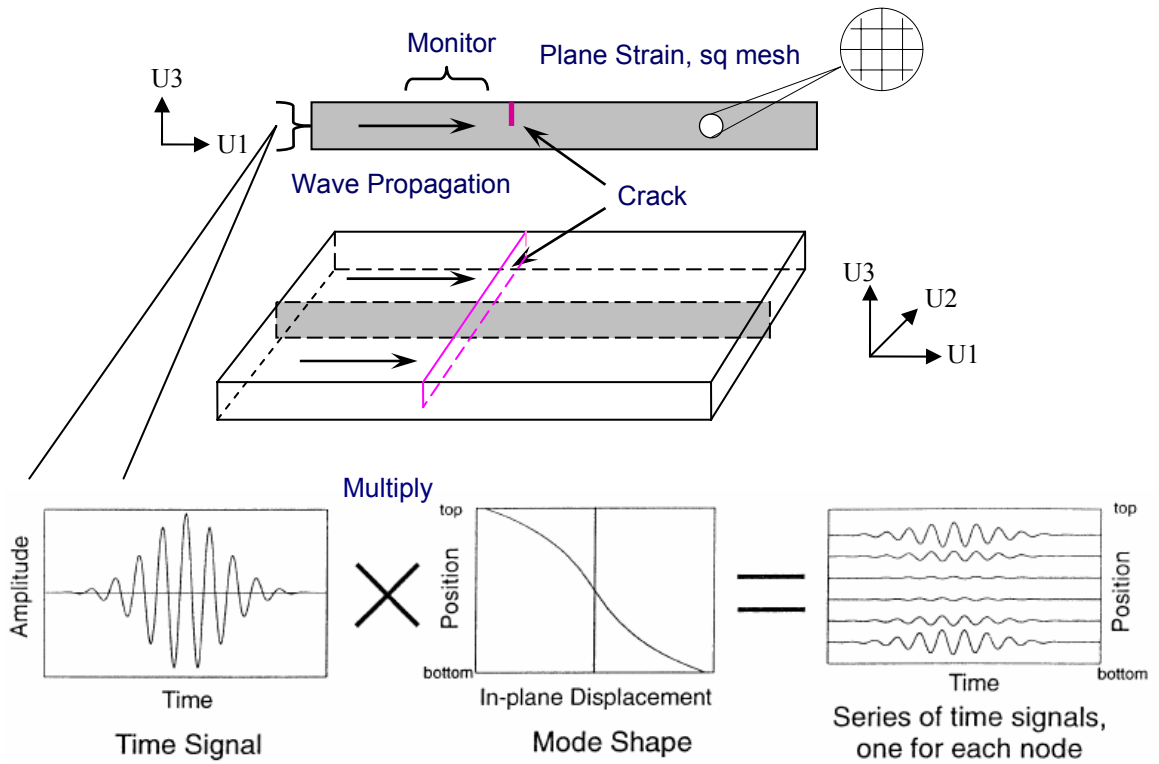
Figure 3.5 A schematic illustration of the spatial domains for the FE models generated to study the interaction of the A0 mode with long surface breaking cracks in a plate. A cross section of the plate is modelled using plane strain elements and the mode shape is used to apply appropriate time domain excitation at the through-thickness points. A part of the figure is taken from [150].
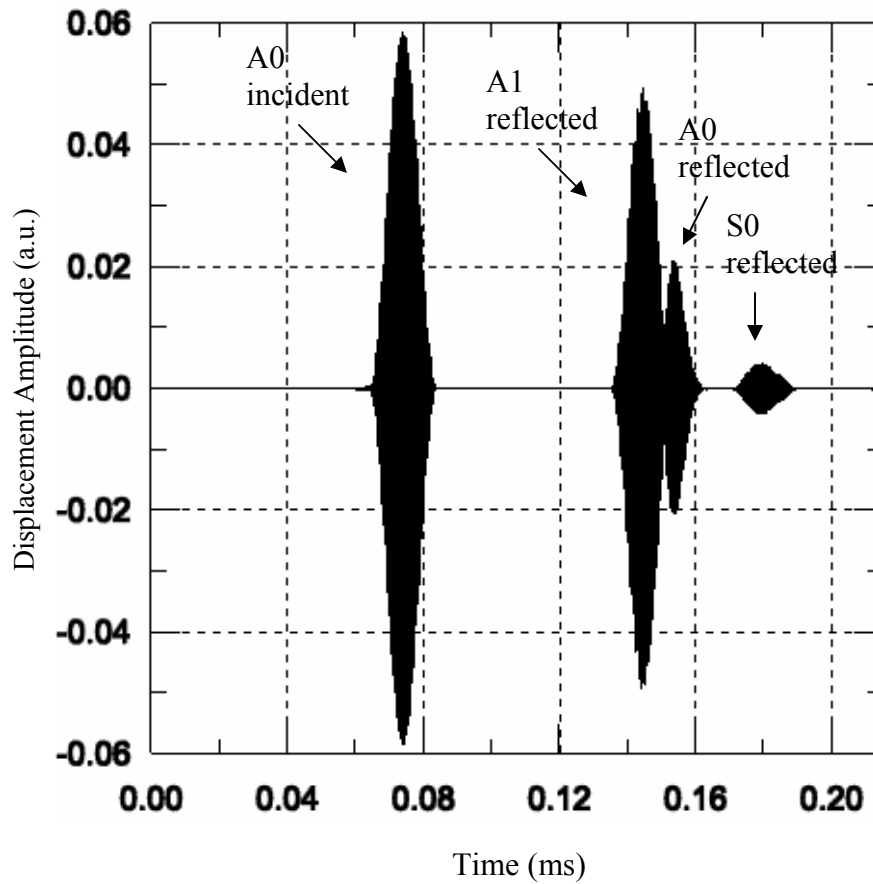
Figure 3.6 Typical monitored signal showing the incident A0 wave and the reflected packet, which consists of all the modes that are reflected from the crack.
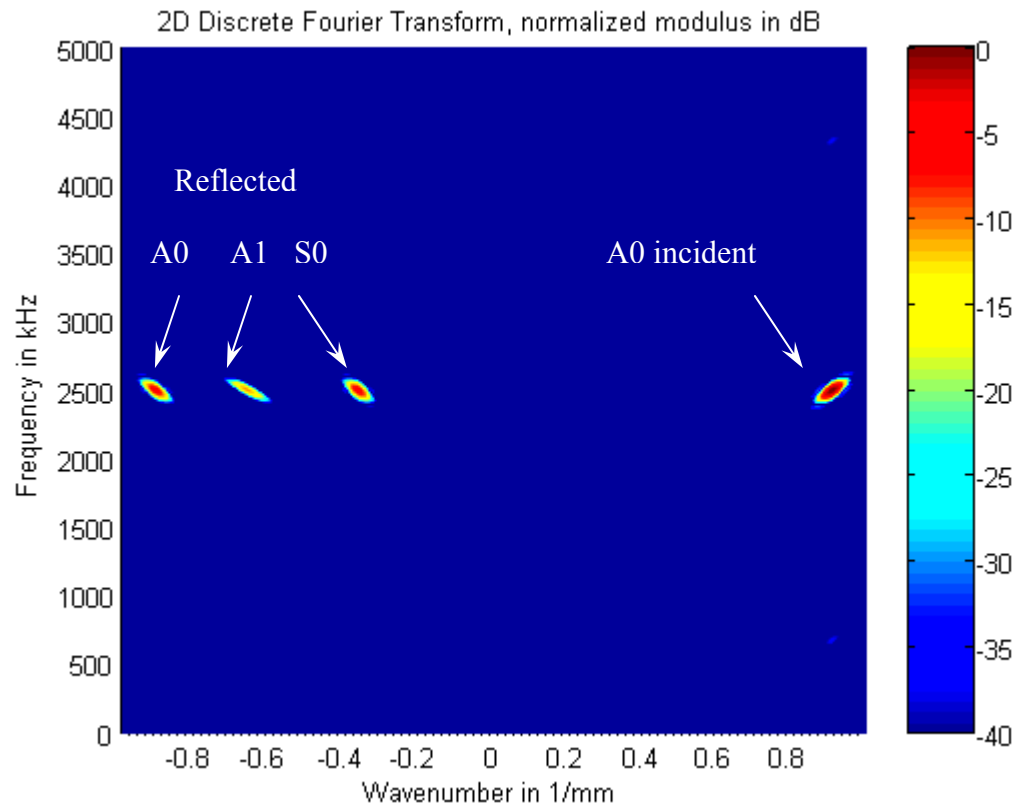
Figure 3.7 Separation of signals achieved by 2D FFT: positive wavenumber indicates the direction of propagation of the incident A0 wave and thus the reflected wave packet is seen on the negative wavenumber axis.
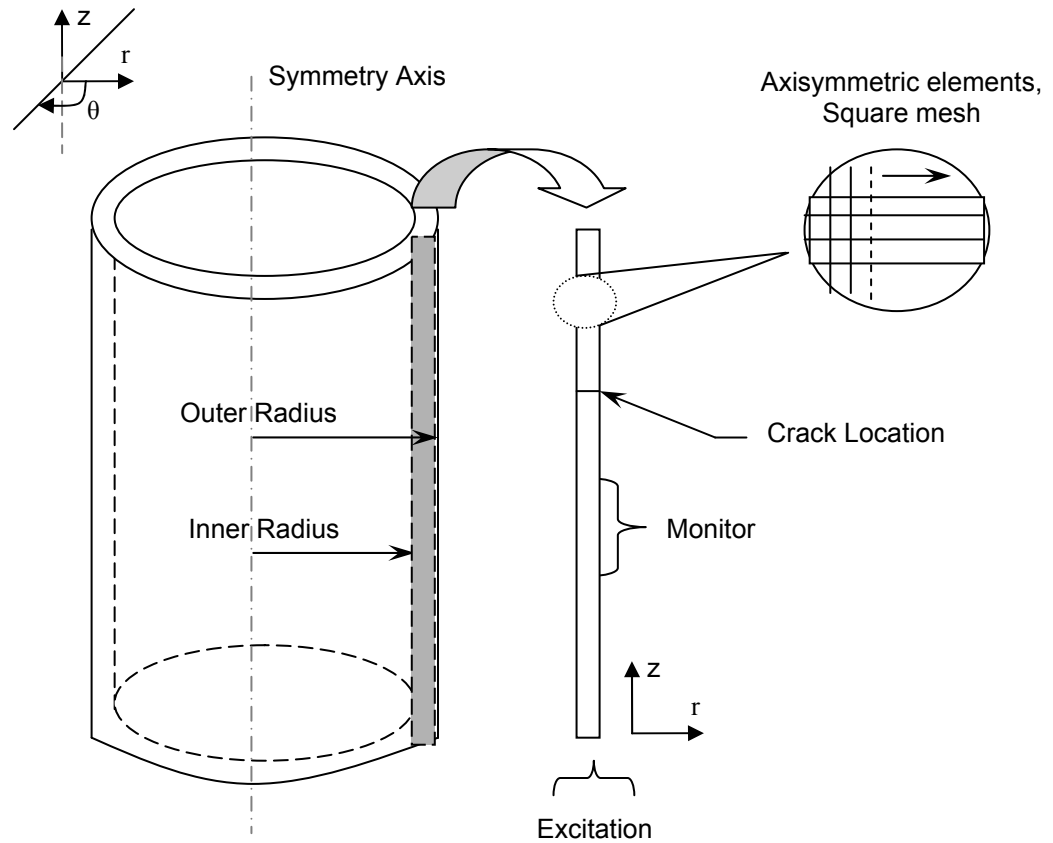
Figure 3.8 Schematic illustration of the axisymmetric models used to study the high frequency reflection behaviour of the T(0,1) mode.
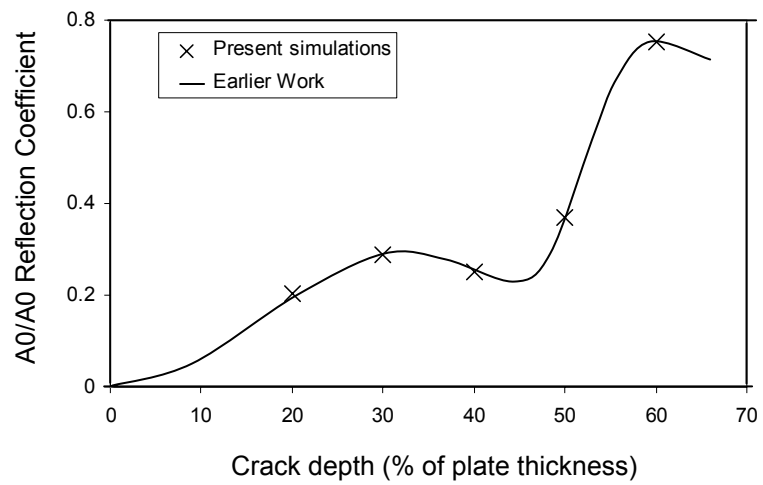
Figure 3.9 Comparison of the A0/A0 Reflection coefficient for incident A0 mode centred at 1.5 MHz-mm, with values from earlier FE modelling work at the NDT Group [27]
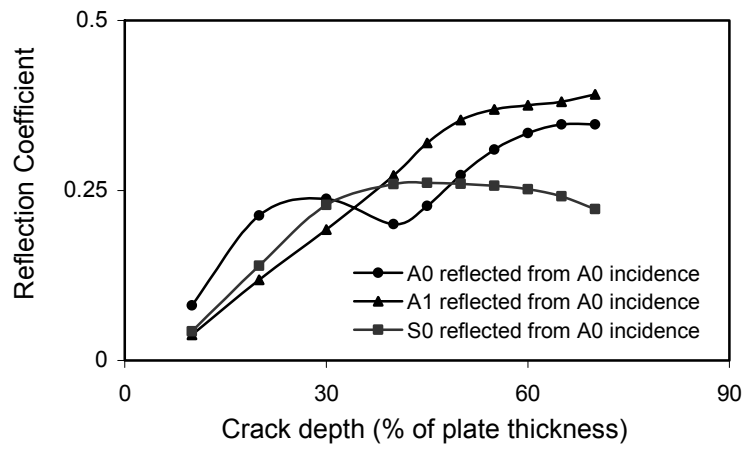
Figure 3.10 FE results at 2 MHz: variation of reflection coefficient with crack depth when A0 mode is incident on a long normal crack in a 1mm thick aluminium plate.
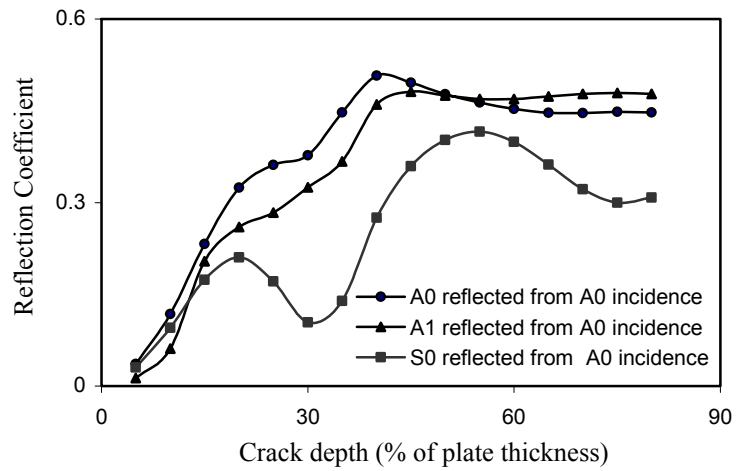
Figure 3.11 FE results at 2.5 MHz: variation of reflection coefficient with crack depth when A0 mode is incident on a long normal crack in a 1mm thick aluminium plate.
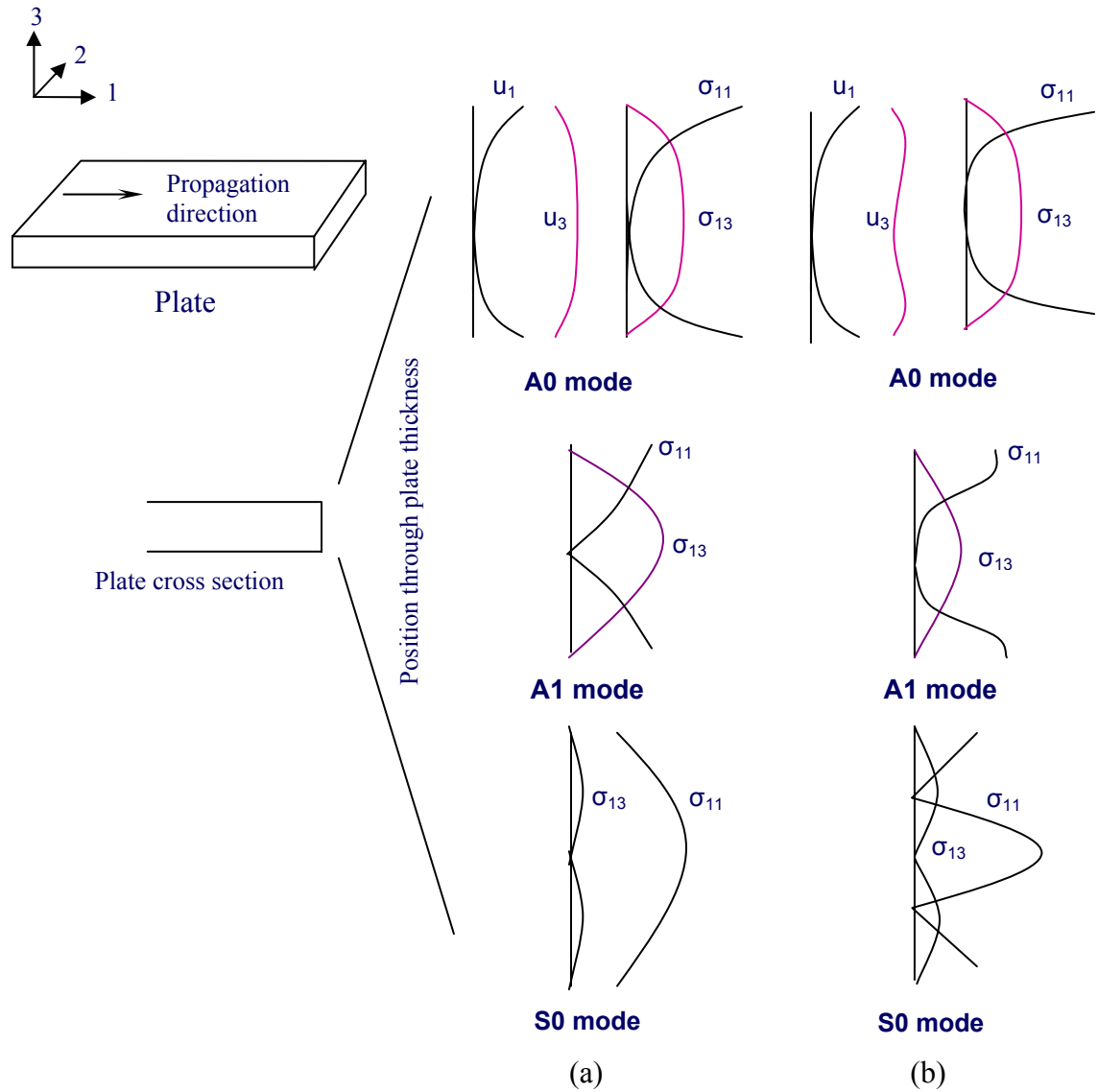
Figure 3.12 Stress mode shapes for the A0, A1 and S0 modes in an isotropic plate. (a) at 2 MHz-mm (b) at 2.5 MHz-mm. There is a phase difference between the components about the mid-plane of the plate, so the modulus of actual values is shown.
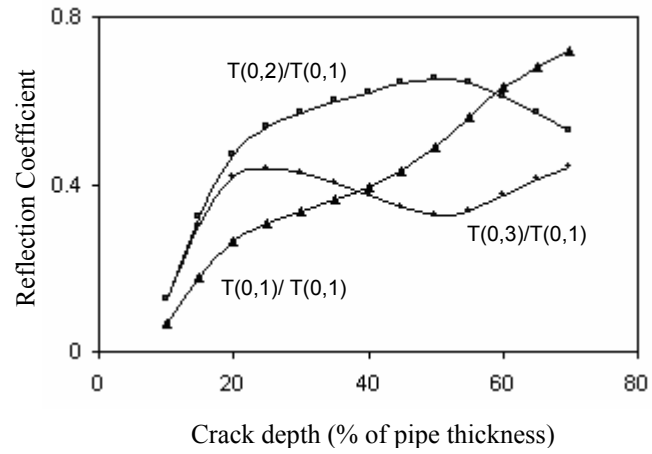
Figure 3.13 The variation of the reflection coefficient of the T(0,1), T(0,2) and T(0,3) modes with increasing depth of the crack through the pipe thickness.
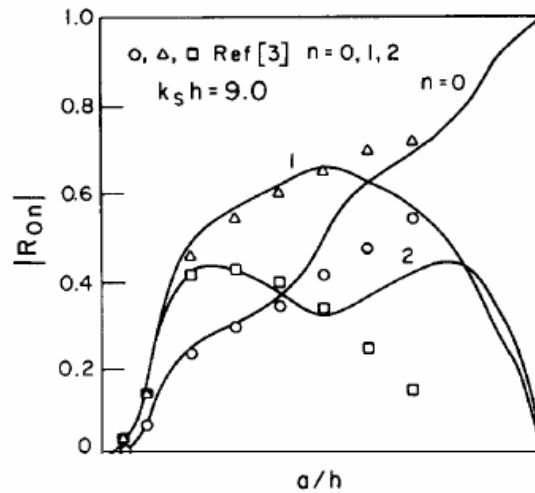
Figure 3.14 Figure 7 from Abduljabbar *et al.* [121] showing the modulus of reflection coefficient R_{0n} for the case $k_s b = 9.0$ which corresponds approximately to 4.5 MHz-mm with *n* referring to the order of the guided Shear Horizontal modes and *b* and *h* are the crack depth and plate thickness respectively.
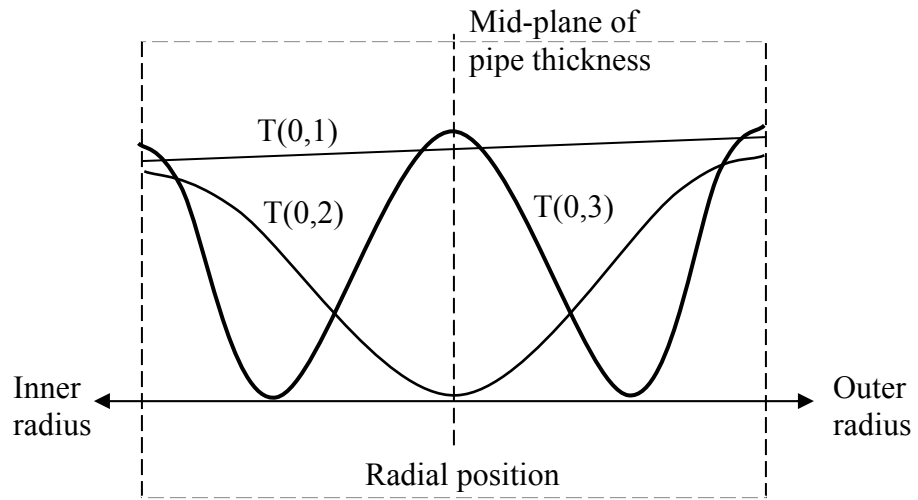
Figure 3.15 $\sigma_{z\theta}$ mode shape for the T(0,1) , T(0,2) and T(0,3) modes at 4 MHz-mm. The dashed line at the centre represents the mid-plane of the pipe thickness. The U_θ modeshape for the incident T(0,1) mode is directly proportional to its $\sigma_{z\theta}$ modeshape
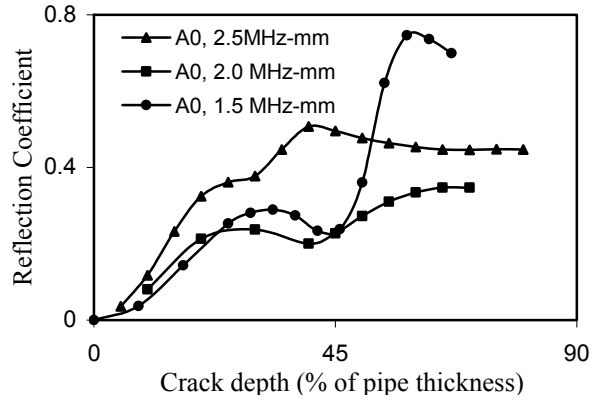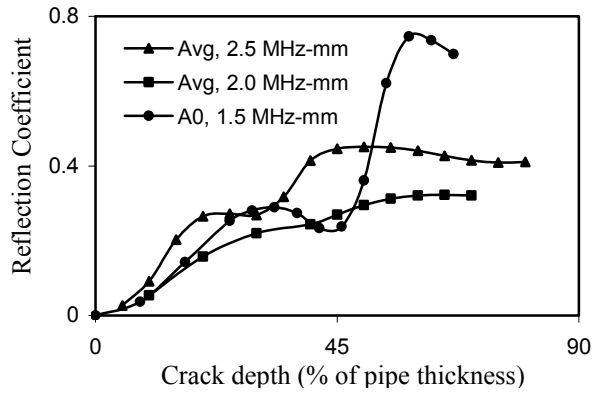
Figure 3.16 (a) Comparison of A0/A0 reflection coefficient variation with crack depth at 1.5, 2 and 2.5 MHz-mm respectively; (b) The average reflection coefficient for all modes at 2 and 2.5 MHz-mm compared with A0/A0 reflection coefficient at 1.5 MHz-mm.
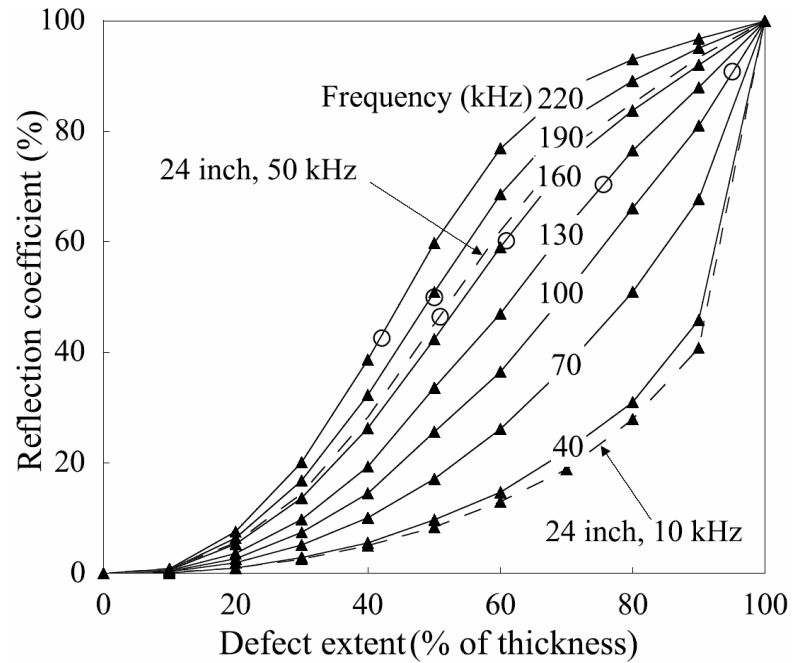
Figure 3.17 Results from Demma *et al.* [29] for the T(0,1) reflection coefficient behaviour with the depth of axisymmetric cracks, obtained at various frequency values in the low frequency regime. Solid and dashed lines stand for pipes of thicknesses of 5.5 mm and 20 mm respectively. The empty circles indicate the crack depth *b* for which the product $k \cdot b = 1$ at each frequency, where k is the wave number.
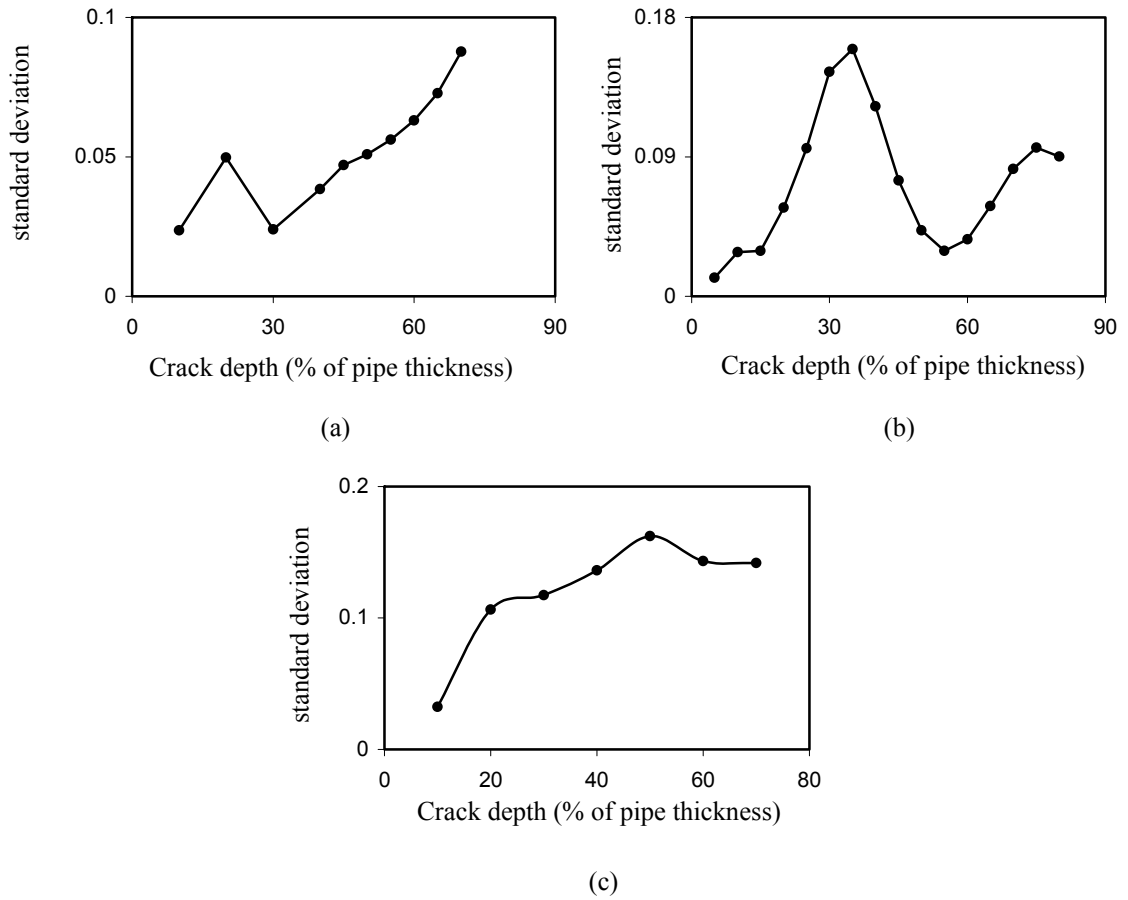
Figure 3.18 (a) and (b) show the standard deviation between the reflection coefficients of A0, S0 and A1 modes at 2 and 2.5 MHz-mm respectively, plotted with crack depth; (c) shows the same for T(0,1) , T(0,2) and T(0,3) modes at 4 MHz-mm.

Chapter 4

Low frequency SH0 mode interaction with through-thickness cracks: normal incidence

4.1 Introduction

In the low frequency-thickness regime, the resolution achievable for defect dimensions in the sagittal plane (or the 'in-plane' dimensions) is lower because of the longer wavelengths. But operation here is simpler, because of the fewer and relatively less dispersive guided wave modes present. Current transduction methods can be applied without much modification. Therefore it would be advantageous to work in this regime, provided we can devise ways to improve the discrimination capability. One way of achieving this, currently being investigated at the NDT Group, is to use array imaging methods. Even if this can just yield information about lateral size of the defect, it can be readily used with currently available inspection techniques to estimate its depth.

The practical implementation will consist of an array of transducer elements, which will probe the defective region as illustrated for a plate structure in figure 4.1. A particular chosen mode will be generated at each transducer and the signal scattered back received at all the elements in the array. The matrix formed out of the signals from different send/receive combinations will then be processed by imaging algorithms and a flaw outline obtained.

Researchers at the NDT Group are currently working on general imaging ideas and array methods [43, 44, 155]. The T(0,1) mode is of interest for such studies since it is the mode of choice in current low-frequency pipe inspection methods, but the initial work was performed using the corresponding SH0 waves in thin plates.

4.1.1 Array imaging with the SH0 mode

The interaction of an SH0 mode array with through-thickness cracks in thin plates was simulated using Finite Element (FE) analysis: the procedure for these simulations is described later on in this chapter. A series of FE models was set up for different combinations of crack length, array aperture and array to crack distance. The array itself consisted of 33 'elements' or source positions spaced at two per SH0 wavelength at the centre-frequency of the incident signal (denoted by λ_{SH0}). The transducers in a practical array are expected to behave as point sources and so their behaviour was simulated by applying point forces vibrating parallel to the crack length at each element of the array. For each source position, the signals scattered back by the crack were monitored at all the elements of the array. The theory behind the generation of modes due to such 'in-plane' excitation and the different components in the scattered signal are discussed in section 4.2 of this chapter. Figure 4.2 shows a snapshot of the contour of magnitude of resultant displacement from an FE simulation, illustrating the typical interaction of the modes generated from a single point, with the crack; the result presented is for forcing applied at a point which is 2 λ_{SH0} from the central array element. Figure 4.3 shows a time-trace recorded at the array element directly perpendicular to the crack, for forcing applied again at a point 2 λ_{SH0} from the central element. It is the matrix consisting of such time-traces from the different possible send-receive combinations which serve as the input for array imaging algorithms.

Figure 4.4 shows an example of the results that researchers using low frequency array imaging methods are interested in arriving at and improving. Generated by synthetic post-processing of pulse-echo data [43], the input for this image was obtained from the simulated interaction of a transducer of aperture 8 λ_{SH0} with a 2 λ_{SH0} long through-

thickness crack located 10 λ_{SH0} away. Though in this particular case the crack was fairly long, the image captures its position and dimensions quite well and this is an encouraging result.

For a more complete idea of the efficacy of these methods, a single set of 3D FE simulations was also performed, studying the interaction of an SH0 mode array with part-a thickness crack. These were carried out with the help of Mr Sumeet Kale, a final year undergraduate student from the Indian Institute of Technology - Kanpur who worked at the NDT Group during summer 2007. The procedure for these 3D simulations is described in Chapter 6 which focuses on part-thickness cracks. Figure 4.5 shows the image obtained from this data, generated again by methods [155] similar to those used for Figure 4.4. The simulated aperture and the transducer-crack distance in this case were the same as for Fig. 4.4 but the crack was 1 λ_{SH0} long and ran only 50% through the plate thickness; also the excitation now consisted of in-plane line sources uniform through the plate thickness The length of the crack as well as its position is again captured very well by the image.

Following such leads, the work on imaging has since been extended to and focussed on the T(0,1) mode in pipes, where the 'common source method' (or CSM) has been found to be effective [155].

4.1.2 Low-frequency SH0 mode interaction with finite cracks

In the light of these developments, there is a need to understand the performance of the individual elements that contribute to the total array, some key questions being how the transducer, defect location and defect extent impact the accuracy of such methods. Since as noted as noted above, the elements of the array are expected to behave as point sources, this involves understanding the interaction of cylindrical crested guided waves with defects. Also, the direction of specular or mirror-like reflection from a defect alone cannot account for the scattered fields captured by all the array elements: thus off-specular and local effects, edge or tip diffraction, would need to be considered. In view

of the positive results from the plate array studies described above using the SH0 mode and its relation to torsional modes in pipes, it is ideal for such studies.

General scattering studies have been carried out extensively for bulk elastic waves: analytical methods using eigenfunction expansion for simple defect geometries (see the monograph by Pao and Mow [55] for an extensive review) and approximate and numerical methods using the integral equation representation for cracks and complex defects [62, 82, 92, 94, 109, 113, 156, 157]. Studies in the guided elastic wave case have followed these developments, but have been more restricted because of the greater challenges involved: the possibility of existence of several propagating modes even at low frequencies, frequency dependent mode shapes and their mutual inter-conversion on interactions with flaws. Thus plane waves and specular reflection have mainly been studied [74, 120, 121, 127-129, 135, 138, 139, 143, 158-160] and numerical methods such as Finite and Boundary Elements have played an important role [19, 26, 27, 41, 42, 161, 162]. Investigation of circular- (or cylindrical-) crested waves [163] or the near field [164-166] and diffraction effects [137, 167] are rare, especially for finite defects. Therefore the following chapters of this thesis focus on the general shorter range scattering of the cylindrical crested[163] SH0 mode by ideal (fully open and flat) but finite cracks in isotropic plates. The present chapter and the next study the case of through-thickness cracks, while Chapter 6 makes use of insights from these results to tackle the more general and difficult case of part-thickness cracks.

4.1.3 The problem studied in this chapter: normal incidence at through-thickness cracks

This chapter considers the simple case of a through-thickness crack or slit and the symmetric incidence problem such that a line from the wave-source bisects the crack face at 90^0. This case is called 'normal incidence' in recognition of the path of the central 'ray' of the incident beam. The nature of scattering is studied in terms of the specular reflection from the crack face as well as the diffraction at its tips. We will begin by examining the influence on specular reflection, of the crack length, and also of the

location of source and measurement positions in view of our interest in the short range. These then lead to the study of the diffraction phenomena. The Finite Element (FE) method is the tool used for this purpose, and the results for the reflection studies are compared with experiments. Though this is taken as general validation for our FE simulations, for the case of diffraction, known results from similar problems in literature are used to further assure us of our modeling procedure. For clarity, the term crack is used when describing FE simulations and the term slit, in the context of experiments.

The sections of this chapter are organized as follows. First the problem studied and the general procedure for the FE simulations and experiments are described in Section 4.2. The particular strategies for the different sets of studies and the results are presented in Section 4.3. Section 4.4 discusses the results in the light of some qualitative and quantitative considerations and finally Section 4.5 presents conclusions and the implications of the findings for guided wave imaging.

4.2 General methods

4.2.1 Studied configuration

Figure 4.6 shows the details of the configuration studied and also of the procedure for FE simulations described next in this section. A finite, fully open through-crack of vanishing width (shown as 'w' in Figure 4.6) is located in a thin isotropic plate, its length ℓ aligned with the U2 coordinate axis. A low-frequency excitation is applied in the U2 direction, at a point 'P' on a line bisecting the crack at 90^0. The excitation is assumed to be uniform through the plate thickness. This generates [168] circular waves of the SH0 mode principally in the U1 direction and those of the S0 mode, principally in the U2 direction. Figure 4.7 shows the group velocity dispersion curves for modes which can exist in a free aluminium plate at low frequencies: apart from the SH0 mode only the fundamental antisymmetric (A0) and symmetric (S0) Lamb modes occur. The A0 mode is not considered in the present problem, as the thickness-wise uniform excitation vibrating

parallel to the plate surface is expected to generate very little of it, and the through-thickness symmetry of the crack ensures that it is not generated by the scattering. The SH0 mode is nondispersive throughout and has constant particle vibration through the plate thickness which is entirely perpendicular to the direction of propagation and parallel to the plate surface (the U1-U2 plane in Figure 4.6). At low frequencies, the S0 mode is also nondispersive with its particle vibration predominantly parallel to the direction of propagation and constant through the plate thickness. The excitation is such that the principal direction of the incident SH0 waves bisects the crack face at 90^0, lending symmetry to the problem. Away from their principal directions both modes exhibit a characteristic cosine angular decay of the displacement amplitude. Thus although in general, the S0 mode is also excited, we are able to study the scattering from the SH0 mode in isolation as the former does not propagate strongly towards the crack. Further, as can be seen from Figure 4.7, in the low frequency-thickness regime the S0 mode travels much faster so that its effects can be time-gated out.

We will then study the SH0 specular reflection from the crack face and the SH0 diffraction from the crack edges. Thus we are essentially interested in the SH0 scattering phenomena happening in the U1-U2 plane parallel to the plate surface and assume uniformity through the plate thickness. If instead we could consider this plane to be the cross section of a solid body, this problem would be equivalent to that of bulk Shear Vertical (SV) wave scattering by internal cracks: along their sagittal planes, these two problems would share the same boundary conditions. We will touch more on this equivalence in Section 4.3.3.

4.2.2 General procedure for Finite Element simulations

A two-dimensional domain with the assumption of plane stress was used for the FE simulations, implemented using the programme ABAQUS [149]. The models so generated are representative of an arbitrarily thin plate or a section of a plate parallel to its surface and lying at its mid-plane; they do not support plate bending or part-through defects. Since the SH0 mode is nondispersive and its mode shape is constant through the

plate thickness, such a model will represent it accurately at any given frequency-thickness value. But the S0 mode has similar properties only in the low frequency-thickness region, so the model provides reasonably accurate results for values up to 0.5 MHz-mm for this mode; the FE studies were carried out at 0.1 MHz-mm. For simplicity, we will assume the plate thickness to be 1 mm in the following parts of this chapter, so the frequency-thickness at an input frequency of say f_0 MHz would simply be f_0 MHz-mm. Further, the results obtained at f_0 would be valid at any other frequency f_1 provided the dimensions are appropriately scaled by a factor of f_1/f_0 by which the wavelength is scaled: experimental verification studies have been based on this understanding and simulation results showing favourable agreement to this idea are also presented in Section 4.3.1. The models do not support the A0 mode but as observed above, this mode is not expected, so this does not pose a problem.

Much of the past work in the two-dimensional domain has been done in the U1-U3 plane and consequently, focused on part-depth but infinite length defects. In contrast, the present study is performed in the U1-U2 plane and helps understand the impact of the length of a finite defect on the interaction of the incident mode with the defect.

Figure 4.6 again shows the temporal and in-plane spatial details of the models and the coordinate system; the out-of-plane dimension (containing the U3 direction), is the direction of the plate thickness. Two strategies were used to prevent S0 reflections from the edges from arriving together with the SH0 scattering from the crack at the monitored locations. For simple scattering studies, the in-plane dimensions of the model were chosen to be large, so that the edge-reflections arrive much later and can be time-gated out. The model size was restricted in such cases by simulating only half the domain and specifying one edge of the model to be a plane of anti-symmetry. But for the studies requiring a complete isolation of only the scattered SH0 mode, absorbing layers with increasing damping (or *ALID*, see Drozdz *et al.* [169]; see Castaings *et al.* [170, 171] for more details on the use of absorbing boundaries in FE analysis) were used around the edges of the plate. The mesh consisted of perfectly square 2 mm long elements, allowing for around 16 elements per SH0 wavelength, respecting the spatial discretization limit

required for accurate modelling [146]. Cracks were created by disconnecting elements at the nodes defining the crack and were thus of zero width. Material properties of aluminium were used in all cases except for the validation of diffraction modeling (Section 4.3.3), where the properties of steel were chosen to match those in the literature consulted.

A 5 cycle Hanning windowed toneburst centred at 0.1 MHz was applied as a force in the U2 direction, at a single point. This generates the S0 and SH0 modes, with their principal directions parallel and perpendicular respectively to the applied force. Explicit time integration with a constant time step respecting the stability limit simulates the propagation of the modes. The default condition on the faces of the disconnected elements representing the crack is that of zero stress. Thus the scattering from an ideal open crack is simulated.

The reflection behaviour was studied in terms of a frequency domain ratio of the resultant displacement of the reflected signal to that of the signal incident at the centre of the crack face. The waves in the model decay cylindrically away from the source so the signals were compensated accordingly for beam-spreading such that the ratio from a straight edge would be unity. Thus

$$\text{Reflection ratio} \quad = \quad \frac{|R(\omega)| \cdot \sqrt{D + d_M}}{|I(\omega)| \cdot \sqrt{d_I}} \tag{4.1}$$

where $R(\omega)$ and $I(\omega)$ are the frequency spectra of the resultant displacement obtained from reflected and incident signals respectively, D is the distance between the source and the centre of the crack, d_M is the distance from the crack centre to the point where the reflection is monitored and d_I is the distance from the source to the point where the incident signal is monitored.

Here it must be mentioned that the compensation for beam-spreading was chosen to be based on a straight edge rather than say a point source, because the former is commonly realized in practice. Due to this choice, although the reflection ratio will ultimately reach

unity if the specular reflection for symmetric normal incidence is monitored at a single point while the crack length is increased, it will not remain constant if we vary the distance of measurement while maintaining a constant finite crack length. However since our interest is in understanding the physical principles rather than obtaining a rigorous quantitative parameter that would hold under different conditions, the convenient definition in equation (4.1) is sufficient.

The nature of diffraction was studied in terms of a diffraction ratio, defined as the ratio of the spectrum of the resultant displacement of the monitored diffracted signal to that of the signal incident at the centre of the crack face, both compensated for beam-spreading:

$$\text{Diffraction ratio} \quad = \quad \frac{|D(\omega)| \cdot \sqrt{r_M}}{|I(\omega)| \cdot \sqrt{d_I}} \tag{4.2}$$

where $D(\omega)$ and $I(\omega)$ are the frequency spectra of the resultant displacement obtained from the monitored diffracted and incident signals respectively, r_M is the distance from the tip of the crack to the point where the diffracted signal is monitored and d_I is the distance between the source and the position where the incident SH0 wave is monitored.

Figure 4.8 presents typical time snapshots of the contour of the magnitude of resultant displacement from FE simulations. Figure 4.8a shows an instant soon after excitation: the S0 mode travels faster and can be seen propagating mainly in the U2 direction away from the crack, while the SH0 mode travels primarily towards the crack. Figure 4.8b shows the mode interaction with the crack: the S0 mode has little energy in this direction so it causes little scattering, while the SH0 mode reflects from the crack face and is diffracted by the crack edges. In addition to the SH0 mode, we observe that the scattered field also consists of mode-converted S0. Although in general the scattered energy is distributed between these two modes, overall it is largely and in some directions entirely, concentrated in the SH0 mode. Figure 4.9 highlights this through the angular profile of the SH0-S0 and SH0-SH0 reflection and diffraction ratios calculated from FE simulations, for two special cases respectively: 4.9a presents the reflection ratios according to equation (4.1) for scattering of SH0 waves by a straight edge while 4.9b

shows the angular profile of the diffraction ratios according to equation (4.2) for scattering by a semi-infinite crack. This chapter studies the reflection along the specular direction (90^0 to the crack face) and the diffraction along the crack-line (180^0 to the crack face), where only the SH0 mode is present.

4.2.3 General procedure for experiments

A photograph of the experimental set-up is shown in Figure 4.10. A point-like source excitation was achieved by means of a plane wide-band piezoelectric shear transducer (Panametrics V301, 0.5 MHz center frequency) coupled to the plate through a thin (0.2 mm thickness) and small (3mm diameter, roughly 1/3 that of typical wavelength) brass disc. The excited signal amplitude was measured around and away from this excitation apparatus to confirm the expected angular behaviour of the excited SH0 mode amplitude and its inverse square root decay with radial distance. The excitation signal consisting of a 5 cycle Hanning windowed toneburst was generated by a Wavemaker (Macro Design Ltd., UK) instrument and centered at the required frequency.

The detection was achieved using a laser interferometer with dual differential fiber optic lines (Polytec OFV 2700). The laser beams from the two fibers are each aligned at an angle of 30^0 to the surface of the plate, so that the difference between their signals gives the in-plane surface displacement. The aligner holding the two optical fiber leads is attached to a translatable rotary arm. This way the interferometer reads in-plane displacements perpendicular to the direction in which the arm points, and thus picks up the SH0 mode propagating along that direction. In the studies in this Chapter, the rotary feature of the arm is not used and it is fixed to point along the symmetric normal to the slit face, but it facilitates measurements in the oblique-incidence studies and is therefore described in more detail in Chapter 5. A thin reflective tape was attached to the surface of the plate to enhance the optical backscatter from the laser beam. The measured signals were in general quite weak and so the quality of each displacement measurement was enhanced by applying a band-pass filter and taking an average over 500 acquisitions.

Measurements were carried out on 0.5 mm wide slits of lengths 8 mm, 16 mm, 36 mm, and 65 mm cut in 1250 mm square standard aluminium (commercial purity, AA1050) plates of 1mm thickness. These slits were made using a milling machine with specially procured 0.5 mm diameter cutters. Since the wavelength was at least 15 times that of the slit width for most of the frequencies used, these slits approximate well, the cracks defined in FE. The transducer was positioned on the symmetric normal to the slit face such that the SH0 mode had its principal axis along this line; the detection was also along this line. For each slit length, the center frequency of excitation was swept from 200 kHz to 400 kHz in order to obtain results for increasing ratios of the slit-length to the wavelength. The excitation and detection positions were varied at each center frequency value, so that they were located at a certain constant number of wavelengths away from the slit.

4.3 Specific studies and results

4.3.1 Nature of specular reflection

A number of simple FE models with long in-plane dimensions were set up to understand the dependence of the SH0 specular reflection over the length of the crack. The excitation was located at a distance of 16 λ_{SH0} (SH0 wavelengths at the centre frequency of the toneburst). Nodal displacements in the U2 direction were monitored 5 λ_{SH0} from the crack and along its symmetric normal. The generated S0 mode has nearly zero displacement along this line, so only the incident and reflected SH0 signals are recorded at the monitored points, directly giving the magnitude of I and R for substitution into equation (4.1). Experimental measurements were taken at the appropriate excitation and monitoring distances for each frequency spanning the required slit lengths. In order to confirm that these results are equivalent to those obtained by FE at a constant frequency but for varying crack lengths, we also simulated the experimental situation in FE, sweeping the frequency from 200 to 400 kHz in steps of 50 kHz with cracks of lengths 5mm, 10mm, 36 mm and 65mm to obtain various crack lengths in terms of λ_{SH0}.

Figures 4.11 and 4.12 show typical time plots of monitored displacement including reflection from the crack or slit in FE and experiments respectively. The reflection ratio was calculated for each crack length from these monitored signals using the same procedure according to equation (4.1). Figure 4.13 shows measured and FE predicted values (for both single and swept frequency studies) of the reflection ratio for this monitoring location, plotted with increasing crack lengths. The crack lengths are expressed in terms of λ_{SH0}. We find very good agreement between FE and experiments. In this context and in the rest of the thesis where such comparison with experiments is made, it is pertinent to mention that we do not have sufficient results for each case to enable a statistical analysis and systematic estimation of errors. Thus since error bounds cannot be reliably calculated, features such as error bars are not presented and this is usual in these kinds of studies (see for example, [27, 172, 173]). Therefore we only enumerate a set of the significant ones among the possible sources of error and these include (a) the differences between material properties used in the FE and the actual properties of the experimental plate (b) misalignment of the laser from the intended direction (c) misalignment in the positioning of the transducer (d) limitations on the conditions in which the experimental notches can accurately represent zero-width cracks-this is relevant to the oblique-incidence study in the next chapter .

Coming to the reflection behaviour, initially, for a short crack, the reflection ratio rises linearly with the crack length. Although we would expect the ratio to gradually approach unity as the crack grows large, the observed anomalous overshoot is characteristic of diffraction effects in the short range studied; this can be seen by examining the detailed behaviour at the crack. Figure 4.14 shows the interaction of the SH0 mode with cracks of two different lengths: again, the contour of the magnitude of resultant displacement is plotted, along with simplified line diagrams. We observe that for smaller cracks, the strength of the diffraction field is significant and it arrives together with the reflection, enhancing the received field**.** The interference between these different waves arriving together is borne out in the undulations seen in the reflection trend. These effects may be regarded as focusing of energy by the crack and we will comment further on this further in Section 4.4.1.

4.3.2 Influence of the distance of source and measurement location on reflection behaviour

We then need to find out how the reflection behaviour evolves as we vary the source and measurement positions with reference to the crack and this issue is examined next. There are four possible combinations of source and measurement positions, depending on whether each is close to or far from the crack. Here two complementary cases are considered, to bring insight into the problem: (i) that of a measurement point close to the crack while the source position varies and (ii) that of source position far from the crack while the measurement position varies.

The FE models set-up for this purpose made use of absorbing layers with increasing damping [169] around the edges of the plate. This ensured that only the SH0 reflection from the crack could be observed in preference to other unwanted reflections. For study (i), the measurement position was fixed at $5\lambda_{SH0}$ from the crack while the source position was located successively at 16 λ_{SH0}, 20 λ_{SH0} and 32 λ_{SH0}. For study (ii), the source was fixed at 32 λ_{SH0} and the reflection was monitored at distances of 5, 10, 15, 20 and 25 λ_{SH0} from the crack face. Monitoring in the U2 direction directly gives the values of I and R. The crack length was again varied using a number of simulations and the reflection ratio was calculated according to equation (4.1).

Figures 4.15 (a) and (b) show the plot of reflection ratio versus crack length, obtained at different source and monitoring positions from studies (i) and (ii). Figure 4.16 (a) and (b) show the same information as in Figure 4.15 (b), but with the reflection ratio plotted with the monitoring distance instead of crack length, and 4.16 (c) shows a comparison of these FE results with experiments for three slit length values; we see that the predictions and measurements agree very well.

From 4.15 (a), we see that though the there is a slight variation, the reflection ratio trend is nearly maintained: thus we can say, provided the source is far from the crack and

beam-spreading is compensated for, its position has a weak influence on specular reflection.

From 4.15 (b) we learn that Figure 4.13 represents a general trend which reflections from finite cracks follow in the short range. The reflection ratio rises sharply with the crack length to an overshoot above unity and then gradually approaches unity with undulations due to interference phenomena. Though this behaviour is different for different monitoring positions, the values converge at large monitoring distances (approximately above 15 λ_{SH0}) for even fairly long cracks. In understanding this, it would be useful to think of the crack as a secondary source and look at the similar effects observed with a piston source transducer. If we take the near-field of a compressive piston source as an approximation for the near-field of a crack given by the Fresnel parameter $F = \ell^2/4\lambda$ (where ℓ the length of the crack will be taken as the diameter of the piston and λ is the wavelength λ_{SH0}) we would observe that as long as the crack length is such that the monitoring distance is approximately greater than F, the reflection ratio increases linearly with the crack length. This can be seen in Figure 4.17 (a) and (b) where the reflection ratio is plotted with respect to the monitoring distance normalized to the Fresnel parameter for small and long cracks respectively. We observe that as the monitoring distance begins to fall within what can be called the near-field for the crack ($F \approx 1$) the reflection values tend to oscillate rapidly. But away from this region, the reflection values gradually assume smooth profiles. We will consider this 'crack as a source' suggestion in more detail in Section 4.4.1 to understand more about why the source and measurement positions have the kind of influence on reflection as observed in this section.

4.3.3 Diffraction: validation

A number of researchers have worked on the problem of diffraction of bulk elastic waves by planar cracks [61, 62, 114, 174]. One validation of the modelling procedure is comparison of the present FE results with those from similar problems in literature. Here the theoretical calculations presented by Scruby *et al.* [175] (based on earlier work [61,

176] and confirmed with experiments by Ravenscroft *et al.* [177]) are used. For the case of a long or 'semi-infinite' crack, Scruby *et al.* obtained the amplitude of a diffracted bulk Shear Vertical (SV) wave for incident continuous SV waves, in terms of a diffraction coefficient $F_s(\theta, \beta)$:

$$\frac{\psi_d}{\psi_{inc}} = F_s(\theta, \beta) \sqrt{\frac{\lambda_S}{r_M}} \, e^{ik_S r_M} \tag{4.4}$$

where ψ_d is the frequency-domain amplitude of the monitored diffracted signal and ψ_{inc}, that of the wave incident at the crack tip, λ_S and k_S are the wavelength and wavevector of the bulk shear wave, r_M is the distance from the crack tip to the observation point, and θ, β are the angles of incidence and diffraction at the crack tip measured in a counter-clockwise sense from the crack face.

These results were obtained using a plane-strain assumption but they are valid for the guided SH0 wave with a plane-stress assumption: the latter is concerned with sections parallel to the plate surface while the former deals with the plate's cross-section and as we noted in Section 4.2.1, these problems are equivalent. Examined with suitable coordinates in their appropriate plane, the same condition on in-plane shear stresses governs the propagation of both bulk SV and SH0 waves:

$$\sigma_{12} = G\varepsilon_{12} \tag{4.3}$$

where σ and ε represent the stress and strain tensor respectively and G is the shear modulus. Such equivalence would not hold for compression waves, for which the plane stress and plane strain behaviour would be different.

Moreover, since the formula for $F_s(\theta, \beta)$ is determined using the geometric theory of diffraction (GTD) it is frequency-independent [178] and it could be used for the present comparison. The FE model generated for this purpose is illustrated in Figure 4.18 (a). The tip or edge of a long or 'semi-infinite' crack was exposed to waves of the SH0 mode incident at angles 90^0, 105^0, 120^0, 130^0 and 135^0. The amplitude of the U2 displacement of incident SH0 waves was monitored along their principal axis, and this directly gives

the magnitude of ψ_{inc}. The U1 amplitude of the diffracted SH0 waves D_{UI} is monitored at a range of angles θ_D around the crack tip and the resultant amplitude obtained as $\psi_D = D_{U1} / \cos(\theta_D)$. Equation (4.3) is then used to calculate the diffraction coefficient $\left| F_s(\theta, \beta) \right|$. The steps were repeated for the first three incidence angle cases, with a finer mesh of 1 mm square elements allowing around 32 elements per wavelength at 0.1 MHz-mm.

Figures 4.18 (b) - (d) show the modulus of $F_s(\theta, \beta)$ obtained from FE simulation results for different incidence angles and mesh sizes of 2mm and 1mm, compared with the theoretical predictions from Scruby *et al.* Because of the convergence of the results at the two mesh sizes, simulations for the incidence angles of 130^0 and 135^0 were performed with the 2mm mesh alone and these are shown in Figures 18 (e) and (f). In all cases we find a very good agreement between results from FE simulations and the theoretical method. This lends confidence to the diffraction modeling.

4.3.4 Nature of diffraction

A number of simple FE models were set up to isolate the diffraction due to SH0 mode normal incidence on cracks of increasing lengths. The details of the models are shown in Figure 4.19 (a). The diffraction is monitored along the crack line where the S0 diffraction vanishes and the diffracted SH0 has only the U1 component. The U2 component of the incident SH0 was also monitored along a line perpendicular to the crack. The diffraction ratio was then calculated according to equation (4.2).

Figure 4.19 (b) shows the diffraction ratio plotted with crack length, again expressed in λ_{SH0}. The observed pattern of variation of the diffraction ratio can be explained by a closer examination of the diffracted field. Figure 4.20 (a) and (b) show diffraction at cracks 4 and 2 λ_{SH0} long respectively. We observe that the diffraction field is complex and contains contributions from two interfering components: a 'primary' diffraction from the crack tips or edges and a 'secondary' diffraction due to Rayleigh-like waves

travelling along the crack faces and radiating into the plate at the crack tip. This will be clearer from the analysis later in chapter, in Section 4.4.2.

4.4 Discussion

4.4.1 Understanding reflection behaviour

In section 4.3.2 a suggestion was offered that the crack be thought of as a secondary source when the source is far away from it. As described in Chapter 2, this is a well known idea following from the integral representation of Huygen's principle for the scattered displacement in terms of sources on the surface of a scatterer. Re-stating equation (2.28), and dropping the superscript 'tot' for fields on the scatterer, we have

$$u_k^{sc}(\vec{p},\omega) = \int_S \left[u_i(\vec{s},\omega)[\Sigma_{ij;k}^0(\vec{p}\,|\,\vec{s},\omega)n_j] - [\sigma_{ij}(\vec{s},\omega)n_j]G_{i;k}^0(\vec{p}\,|\,\vec{s},\omega) \right] dS \qquad (4.5)$$

where $u_k^{sc}(\vec{p})$ is the component in the $\hat{e}_k$ direction of the scattered displacement observed at a position $\vec{p}$ in the medium due to a flaw of surface S and outward normal n_j, $u_i(\vec{s})$ and $\sigma_{ij}(\vec{s})n_j$ are the displacement and traction induced at a position $\vec{s}$ on the flaw surface due to the incident wave, $G_{i;k}^0(\vec{p}\,|\,\vec{s},\omega)$ is the Green's displacement tensor giving the displacement component in the $\hat{e}_k$ direction at $\vec{p}$ due to a point force applied at $\vec{s}$ in the $\hat{e}_i$ direction in *the free medium in the absence of a flaw* and $\Sigma_{ij;k}^0(\vec{p}\,|\,\vec{s},\omega)n_j$ is the traction due to the corresponding Green's stress tensor; steady state fields with circular frequency ω such that the displacements and stresses at time t are given by $f(\vec{p},t) = f(\vec{p},\omega)\exp(-i\omega t)$ have been assumed. The time factor $\exp(-i\omega t)$ is omitted throughout.

Thus the scattered displacement arises due to a superposition of secondary sources, $u_i(\vec{s})$ and $\sigma_{ij}(\vec{s})n_j$ placed on the surface of the flaw. In the case of an ideal crack with

traction-free surfaces $\sigma_{ij}(\vec{s})n_j = 0$ and (4.5) reduces in terms of the displacement jump $\Delta u_i(\vec{s}) = u_i(\vec{s} \in s^+) - u_i(\vec{s} \in s^-)$ across the crack faces s^+ and s^-, to

$$u_k^{sc}(\vec{r},\omega) = \int_{s^+} \Delta u_i(\vec{s},\omega)[\Sigma_{ij;k}^0(\vec{p} \mid \vec{s},\omega)n_j] dS \tag{4.6}$$

where the integral is now only on the insonified face s^+ of the crack.

For an exact solution to the scattering problem, Δu_i must be accurately known along the crack face. But here we make use of a Kirchhoff-like approximation for the crack opening displacement and FE simulations, to understand how the different parameters affect scattering. Let a harmonic point excitation parallel to the crack face be located at the mid-plane of a thin plate at a distance R_0 from a crack of length ℓ.

Making use of cylindrical coordinates and placing the origin at the excitation point, the crack is located along the line $r\cos(\theta) = R_0$ and has an outward normal $\hat{n} = \cos(\phi)\hat{e}_r + \sin(\phi)\hat{e}_\theta + z\hat{e}_z$ while the excitation is applied at $(0,0,0)$ along the line $\theta = \pi/2$. For points (r,ϕ) on the mid-plane far from the source, this generates [168],

$$u_\theta((r,\phi),\omega) = \frac{A}{\sqrt{r}}\cos(\phi)\exp(-ik_{SH0}r) \tag{4.7}$$

where k_{SH0} is the wavenumber of the SH0 wave.

If ℓ is small compared to R_0, we can assume that a uniform displacement $u = u_\theta((R_0,0),\omega)\hat{e}_\theta$ impinges upon the crack face. Further, for cracks of lengths such that $k_{SH0}\ell \gg 1$ i.e. $\ell \gg \lambda_{SH0}/2\pi$ we can argue that the two faces of the crack do not interact very much because of which we can simply take $\Delta u_i(\vec{s}) = u_i(\vec{s} \in s^+) = 2u_\theta((R_0,0),\omega)$ and $\Delta u_i(\vec{s},\omega)[\Sigma_{ij;k}^0(\vec{p} \mid \vec{s},\omega)n_j] = 2u_\theta((R_0,0),\omega)\Sigma_{r\theta;k}^0(\vec{p} \mid \vec{s},\omega)\cos(\phi)$. Taking $\cos(\phi) \approx 1$, equation (4.5) now yields,

$$u_k^{sc}(\vec{p},\omega) = 2u_\theta((R_0,0),\omega)\int_{S^+} \Sigma_{r\theta;k}^0(\vec{p} \mid \vec{s},\omega)dS \tag{4.8}$$

Equation (4.8) means that if the length of the crack is small compared to distance from the excitation, it should behave as if point shear sources of uniform strength are placed all along its insonified face: in other words, it would behave as if one face of it were a simple ideal shear transducer.

In order to test the limits of such a model, the behaviour of a crack with one face loaded with parallel point forces was studied using FE simulations. Figure 4.21 shows the U2 amplitude monitored along the symmetric normal to the crack obtained from these simulations, for different crack lengths. For each crack length case, the amplitudes are normalized to the maximum value and compared with similarly normalized results from the earlier full-FE studies of Figure 4.16. We observe that the results from the partial FE simulations assuming Kirchhoff behaviour and the full simulations agree very well for crack lengths up to 5 λ_{SH0}. This means that for small cracks, the response is indeed as if a secondary source were placed on the insonified side, but cracks that are longer than 7 λ_{SH0} cannot be represented using this simple model. However the accuracy of the model will be improved for such longer cracks, if either the source of the incident waves is placed farther away, or the sources assumed along the crack also included the correct phase information.

4.4.2 Understanding diffraction behaviour

In the section 4.3.4 it was opined that the undulations observed in the diffraction ratio-crack length plot (Figure 4.19b) were due to the interference between the primary and secondary diffraction. Here we will take a quantitative look at this idea, using FE simulations again. When the incident waves impinge on the crack, a direct diffraction occurs at the crack edges and surface waves are introduced along the crack faces. These surface waves radiate some energy into the medium upon reaching the crack edges and in turn are reflected back and in this way undergo multiple reverberations across the crack length before dying out. For cracks which are not too small, the radiation from the first train of surface waves is the most important and it is this that trails behind the primary diffraction. We can assume that these surface waves are in phase with the primary

diffraction, but their phase changes as they travel along the crack face and also at the crack tip. If ϕ_P and ϕ_S represent the phase of the primary and secondary diffraction with respect to the excitation point, we can thus write at the crack tip:

$$\phi_S^{edge} = \phi_P^{edge} - k_{surf}\ell + \Delta\phi_{P-S}^{edge} \tag{4.9}$$

where k_{surf} is the wavenumber of the surface wave which propagates along the crack face, ℓ is the length of the crack and $\Delta\phi_{P-S}^{edge}$ is the phase change at the edge. The phase difference between primary and secondary diffraction at the crack edge should hence be

$$\phi_P^{edge} - \phi_S^{edge} = \delta\phi_{P-S}^{edge} = k_{surf}\ell - \Delta\phi_{P-S}^{edge} \tag{4.10}$$

We should therefore expect a plot of $\delta\phi_{P-S}^{edge}$ with ℓ to be linear with the wavenumber of the surface waves as its slope and the phase change at the crack edge as its intercept.

FE models of SH0 wave interaction with long cracks (7-10 λ_{SH0} long) were set up so that the primary and secondary diffraction could be separated from each other along the crack line. Absorbing boundaries using *ALID* were applied in order to study the scattering from the cracks in isolation.

For each crack length case, the U1 component of displacement was monitored at 5 locations along the crack line. Figure 4.22 shows a typical time trace: from such a signal, the primary and secondary components are extracted by time gating. The phase of the waves is then obtained as the value at centre frequency of the imaginary part of the Fourier transform of the respective signal. For each location at a distance 'Y' from the crack edge, the phase of the signal at the crack edge is given by:

$$\phi_P^Y = \phi_P^{edge} - k_{SH0}Y \text{ and } \phi_S^Y = \phi_S^{edge} - k_{SH0}Y \tag{4.11}$$

where k_{SH0} is the wavenumber of the SH0 wave.

Thus $\phi_P^Y - \phi_S^Y$ at any location directly gives $\delta\phi_{P-S}^{edge}$ for a given crack length and the values at the different positions will act as a cross-check. $\delta\phi_{P-S}^{edge}$ obtained this way matched well for all the monitored locations and Figure 4.23 shows these values plotted with crack length. We observe the expected linear variation, in this case given by $\delta\phi_{P-S}^{edge} = 7\ell + 1$ if ℓ is expressed in λ_{SH0}, or equivalently, $\delta\phi_{P-S}^{edge} = 223.64l + 1$ if ℓ is in SI units where the value 223.64 directly gives the wavenumber of surface waves on the crack face in radians/m.

For destructive interference between primary and secondary diffraction, $\delta\phi_{P-S}^{edge} = 2n\pi + \pi$, (n =0, 1, 2...), and for constructive interference, $\delta\phi_{P-S}^{edge} = 2n\pi + 2\pi$. Thus the dips in an interference pattern must occur at $\frac{(2n+1)\pi - 1}{7}\lambda_{SH0}$ or $0.3\,\lambda_{SH0}$, $1.2\,\lambda_{SH0}$, $2.1\,\lambda_{SH0}$ ... and the peaks, at $\frac{2(n+1)\pi - 1}{7}\lambda_{SH0}$ or $0.75\,\lambda_{SH0}$, $1.65\,\lambda_{SH0}$ .... These peak and dip positions are marked using solid and dashed lines respectively for comparison with FE results in Figure 4.19b: we find excellent agreement except for very small cracks whose behaviour cannot be captured by our simple models. Further, for the corresponding wavenumber value of 223.64 radians/m for surface waves traveling along the crack face the phase velocity at 0.1 MHz comes out to be 2809.5 m/s. Surface waves on the edges of thin plates have been studied in the literature on rectangular ridge waveguides [179, 180] and both symmetric and antisymmetric modes are known. The symmetric surface waves on the edges of thin ridges correspond closely to Rayleigh waves (see Oliner's review [179] for instance, for a description of the properties of these waves) and since only symmetric modes can exist in our plane stress FE models, they appear to be equivalent to the surface waves traveling on the crack face. Sinha [181] has shown that the velocity of these waves must be 0.985 times that of Rayleigh waves. For the material properties used in the FE simulations here, the Rayleigh wave velocity is 2925 m/s and therefore the velocity of the symmetric surface waves must be around 2881 m/s: the value of 2809.5 m/s calculated above is within 3% of this value.

4.5 Conclusions

A need to understand the interaction of cylindrical crested guided waves with defects was felt in view of encouraging results from low-frequency array imaging methods. Because of the potential of the SH0 mode for application in plate arrays and its relation to torsional modes in pipes, it is ideal for such studies. The present chapter studied the problem of low frequency waves of the SH0 mode incident at through-thickness cracks or slits such that a line from the wave source bisects the crack face at 90^0.

Finite element studies confirmed by experiments show that in this frequency regime, short range scattering is strongly affected by diffraction phenomena. Studies on the influence of the crack length and source and measurement position on the measured reflection revealed the focussing of energy by the crack in the backscattered direction. A study of the influence of the crack length on the diffracted field shows that it consists of components arising from diffraction from the crack tips and radiation from Rayleigh-like waves travelling along the crack faces. Theoretical analysis of the scattering phenomenon shows that a simple diffraction model of assuming uniform shear sources on the insonified face can yield very good results for cracks as long as seven times the wavelength considered. Investigation of the diffracted field revealed systematically the interference between the primary and secondary diffraction and showed that the waves travelling along the crack face are indeed the symmetric surface waves of rectangular ridge waveguides, which correspond closely to Rayleigh waves.

From the guided wave imaging perspective, these results provide a simple estimate for the far-field values for a given operating frequency-thickness and crack length. The strong presence of diffraction means that more information may be received by a transducer array than would be contributed by specular reflection alone. An understanding of the physics of the scattering such as the reverberation along the crack face, will aid development of imaging procedures. The next chapter continues with through-thickness cracks but considers the non-symmetric or oblique incidence problem.
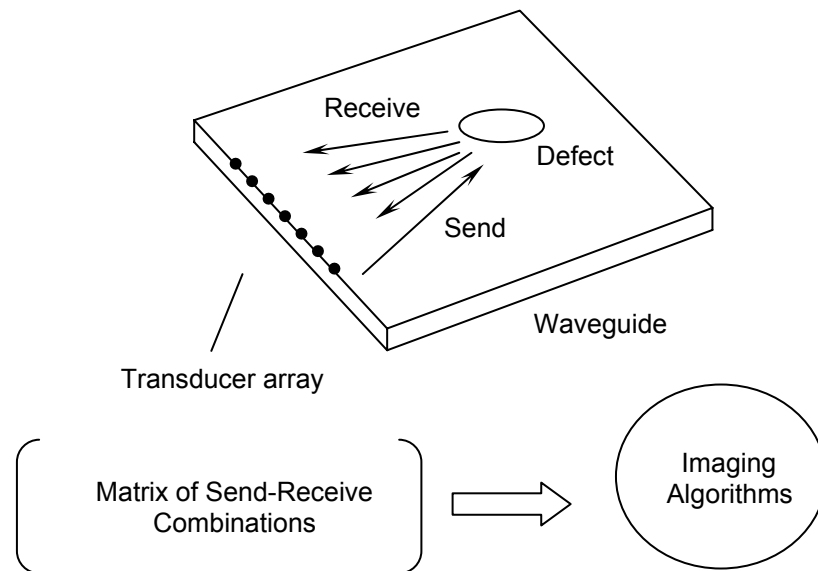
Figure 4.1 The matrix of signals from the send-receive configurations from elements of a transducer array could be used in imaging algorithms to obtain information about the dimensions of the defect.

(a)   (b)
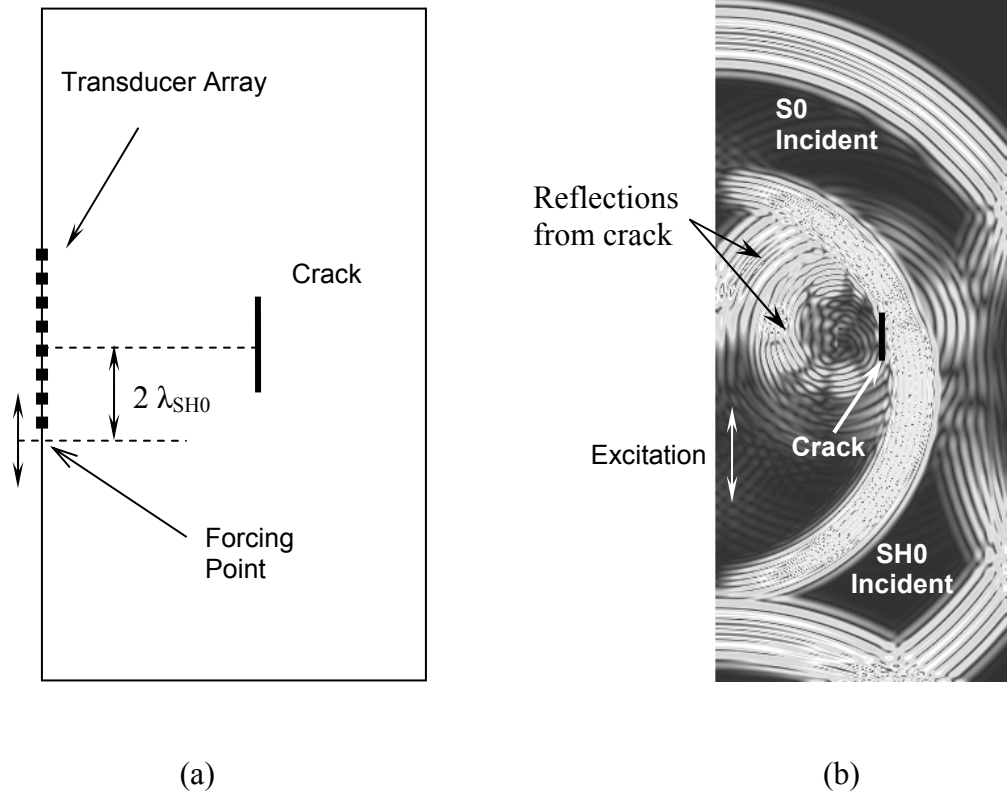
Figure 4.2 Modelling of the transducer array interaction with crack: typical example. (a) Example configuration, forcing applied at a point two SH0 wavelengths from the mid-plane of the model; (b) Snapshot of the contour of magnitude of resultant displacement from an FE simulation, illustrating the interaction of the modes generated from a single point, with a through-thickness crack; the grey-scale from black to white spans the range from the minimum to the maximum displacement amplitudes in the result.
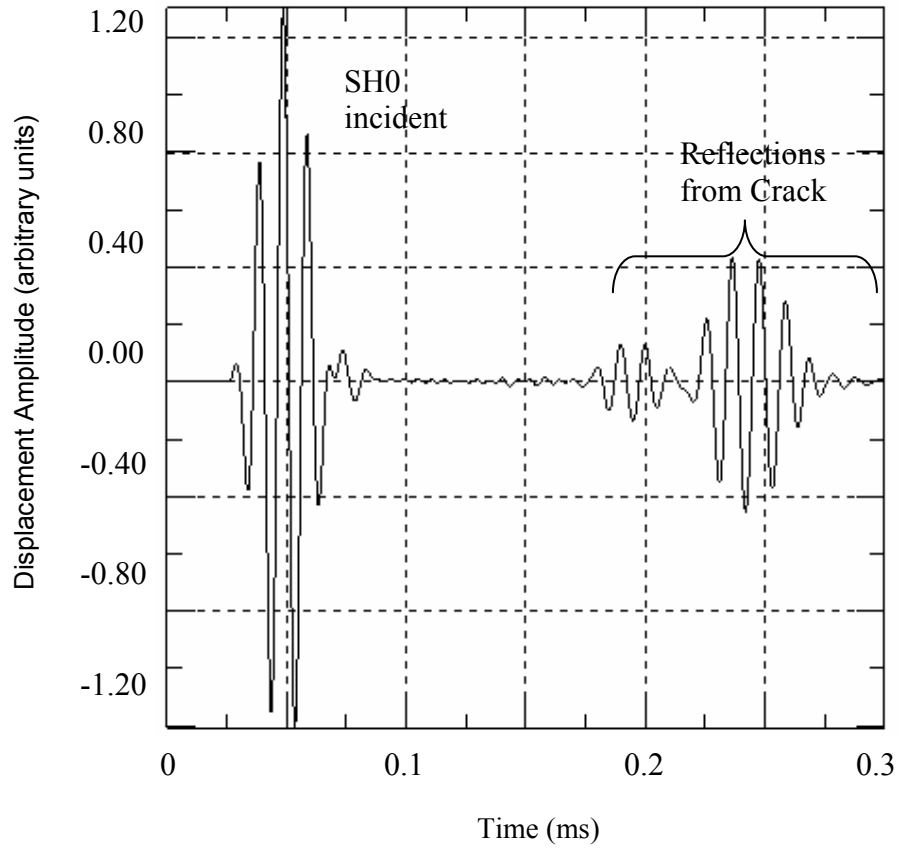
Figure 4.3 Time-trace recorded from FE simulations, at the array element directly perpendicular to the crack for forcing applied at a point two SH0 wavelengths from the mid-plane of the model.
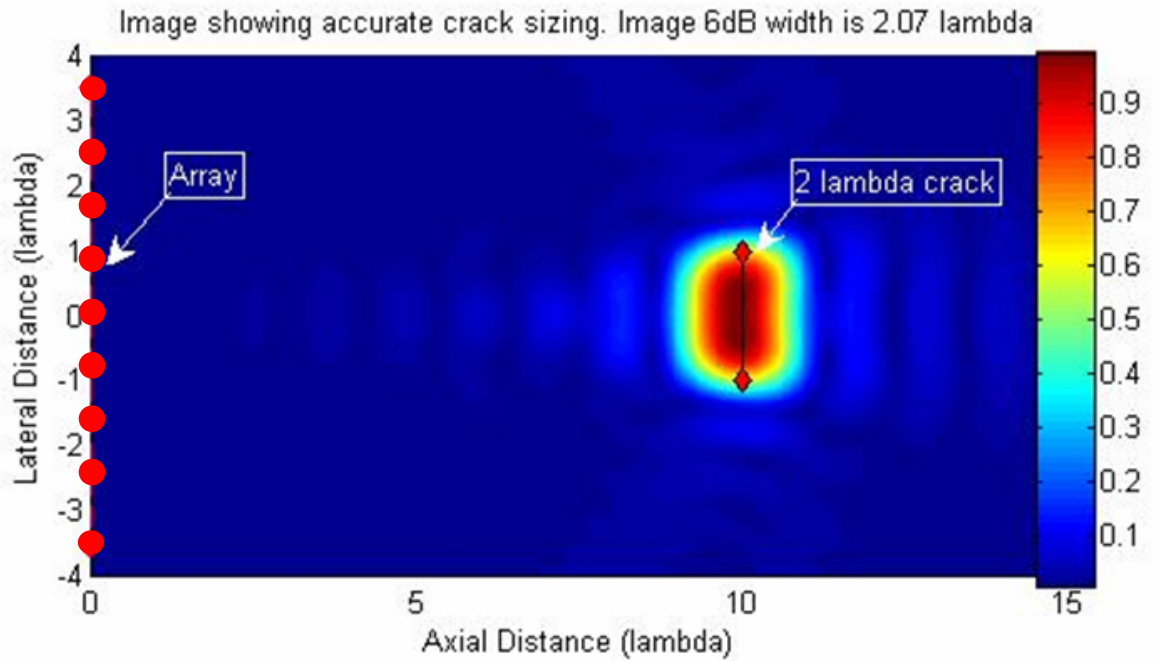
Figure 4.4 Image obtained by processing the matrix of send-receive combinations from the simulated interaction of an 8 λ_{SH0} aperture transducer with a 2 λ_{SH0} long through-thickness crack and a transducer-crack distance of 10 λ_{SH0}; The line has been added to the image to show the location of the crack. Picture source: J. Davies, NDT Group, Imperial College London. The width of the image when its intensity has fallen to half its peak value (called the '6dB width' since $20\log_{10}(x_0/x) = 20\log_{10}(1/0.5) = 6\text{dB}$) captures the actual length of the crack quite well.
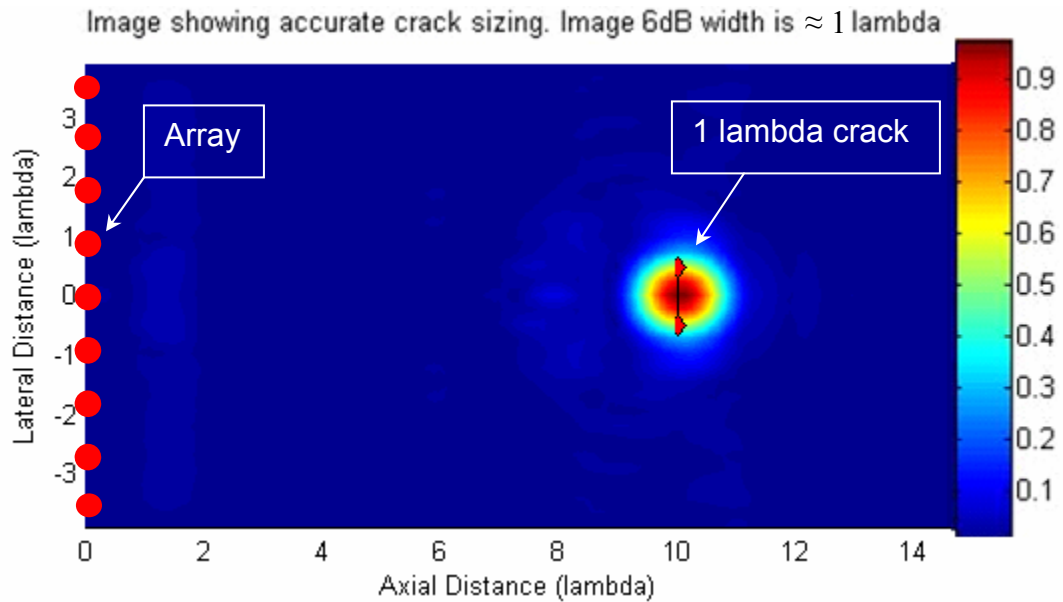
Figure 4.5 Image from simulated interaction of a 1 λ_{SH0} long crack running 50% through the plate thickness with the same transducer aperture and position as for Fig. 4.4. The line has been added to the image to show the location of the crack. Picture Source: J. Davies, NDT Group, Imperial College London; simulations performed with the help of Mr Sumeet Kale, summer student at the NDT Group.
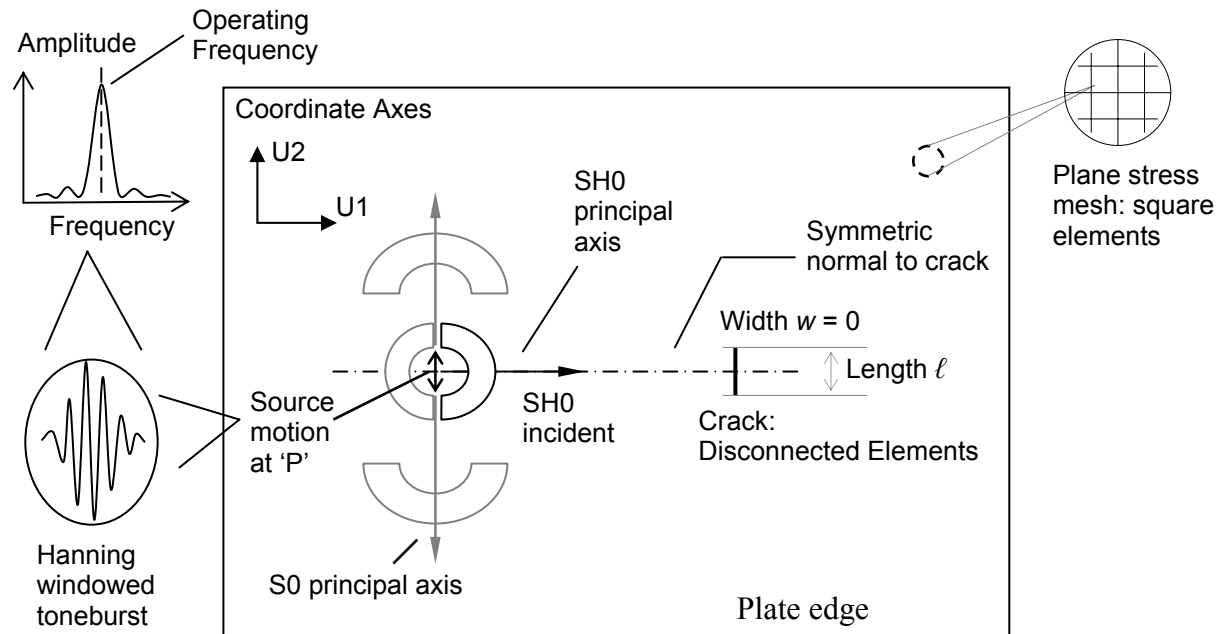
Figure 4.6 Details of the configuration studied. The SH0 mode has its principal axis aligned with the symmetric normal to the crack face.
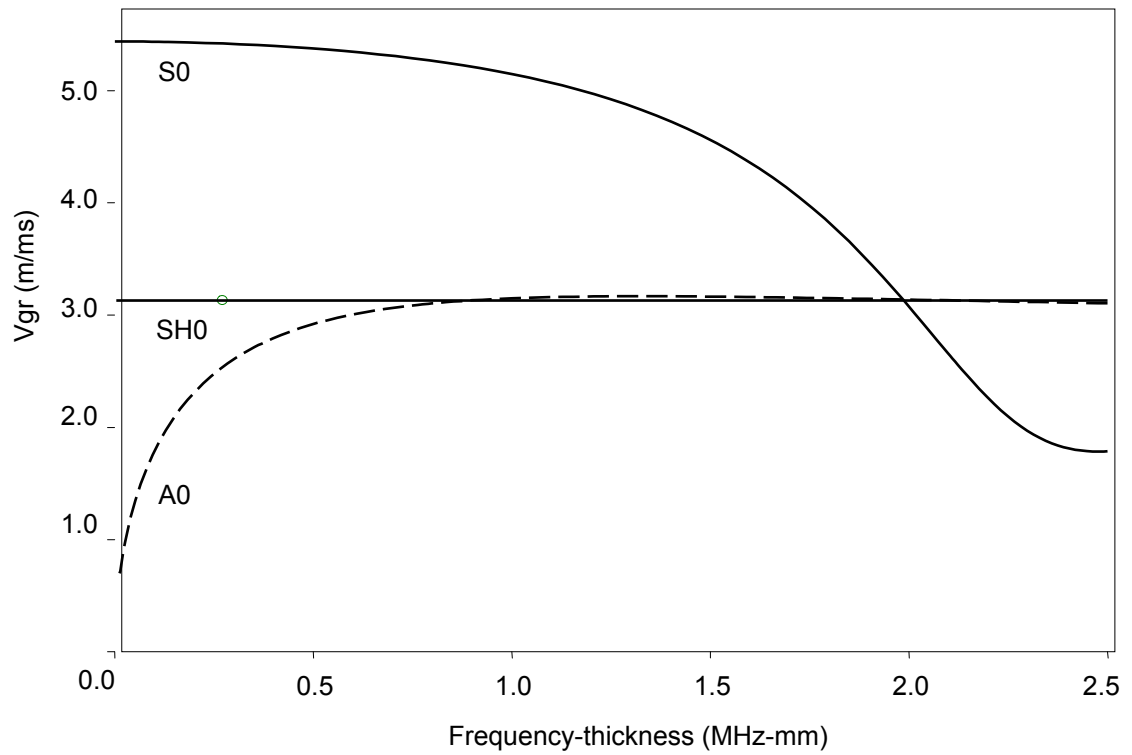
Figure 4.7 Group velocity dispersion curves for low frequency Lamb and SH waves in an Aluminium plate. Since the A0 mode does not occur in our problem, it is shown by a dotted line.

(a)   (b)
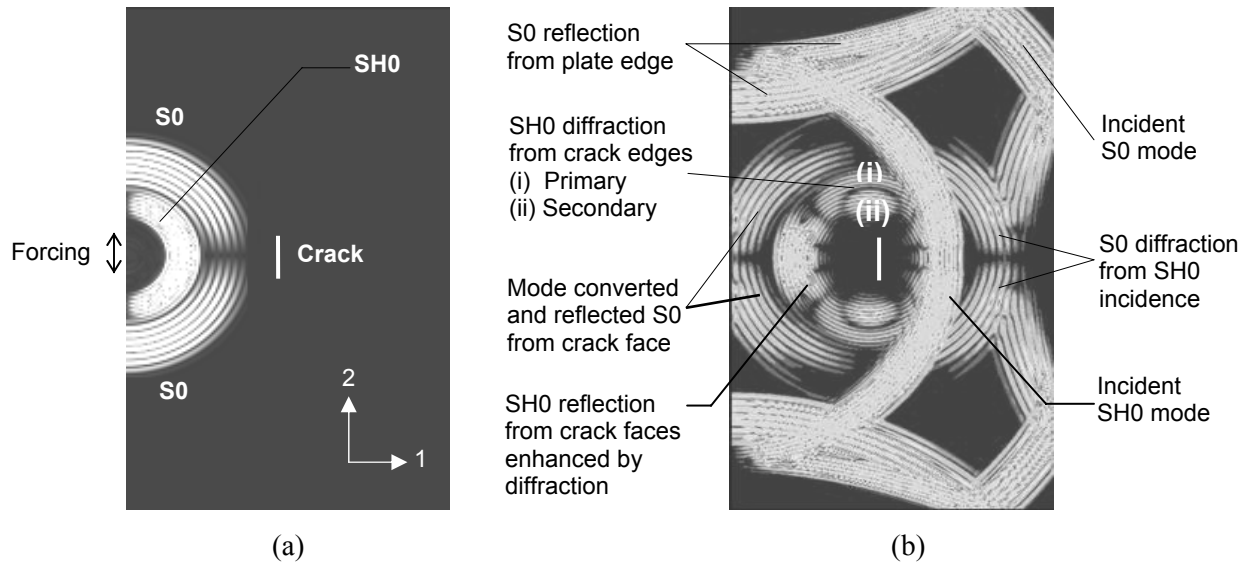
Figure 4.8 Snapshots of the contour of magnitude of resultant displacement from FE simulations, at different time instances (a) Soon after excitation; (b) SH0 mode interaction with the crack; The S0 mode does not interact strongly with the crack as it propagates primarily in the U2 direction.
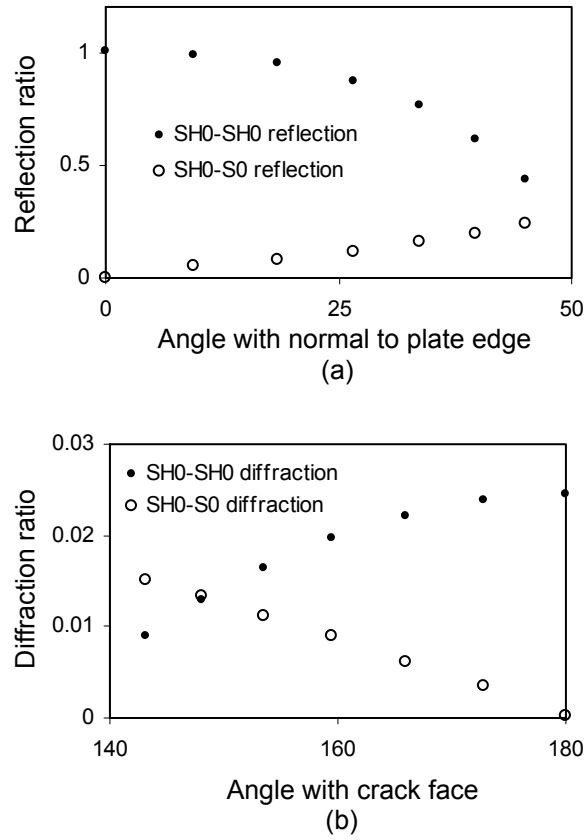
Figure 4.9 (a) Shows the SH0-SH0 and SH0-S0 reflection ratios obtained for a range of angles around the incidence direction for scattering by a straight edge; (b) Shows the SH0-SH0 and SH0-S0 diffraction ratios obtained for a range of angles around the crack line for scattering by a semi-infinite crack
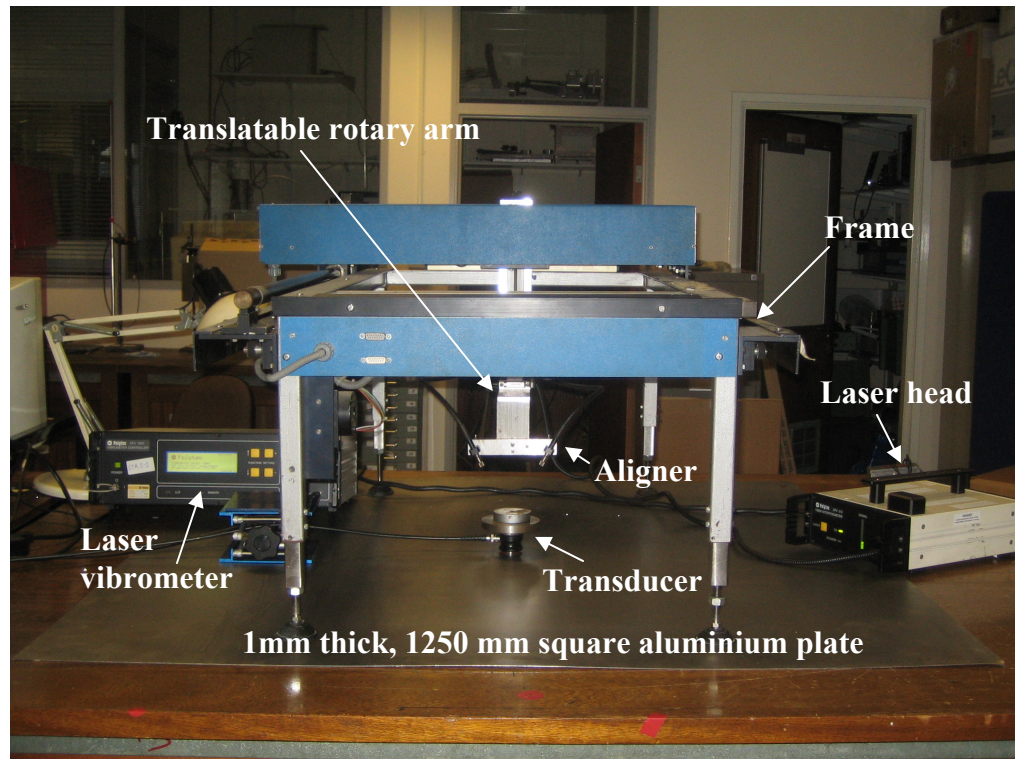
(a)
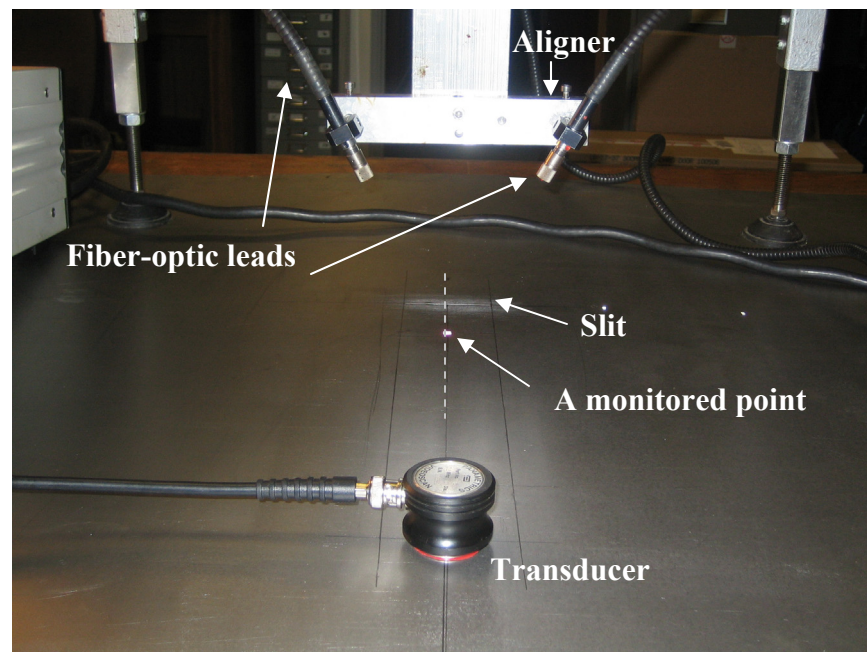
(b)

Figure 4.10 The experimental set-up: (a) Photograph of the entire system; (b) blow-up of

region around the slit. A detailed photograph of the rotary arm is presented in Chapter 5.
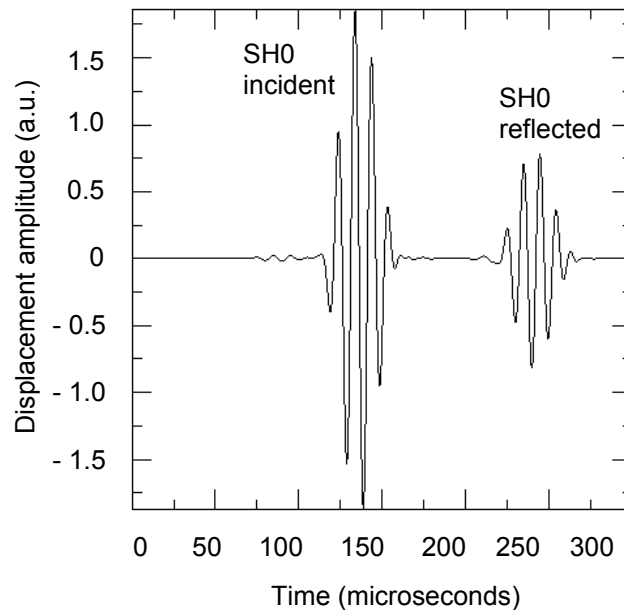
Figure 4.11 Normal incidence of SH0 mode on the crack: typical time plot of displacement in the U2 direction at the monitored point from FE simulations. The tiny precursor to the SH0 mode is the S0 mode, a small amount of which is always generated.
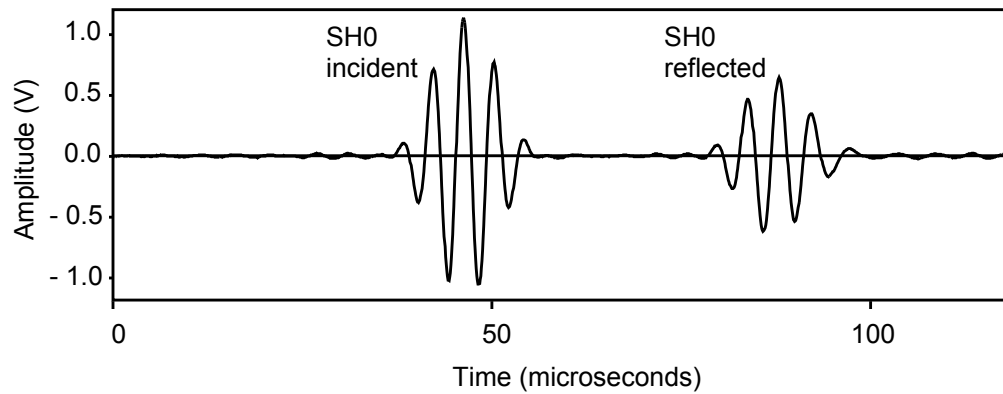
Figure 4.12 Typical time plots of monitored displacement from experiments showing reflection from the slit: values measured at 250 kHz from a 65 mm slit for excitation and monitoring at 200 mm and 64 mm from the slit respectively.
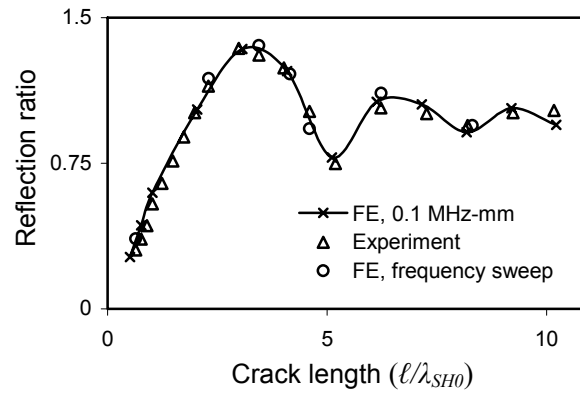
Figure 4.13 Measured and FE predicted values of the reflection ratio plotted with increasing crack lengths for excitation and monitoring at 16 λ_{SH0} and 5 λ_{SH0} from the crack face respectively.

(a)   (b)
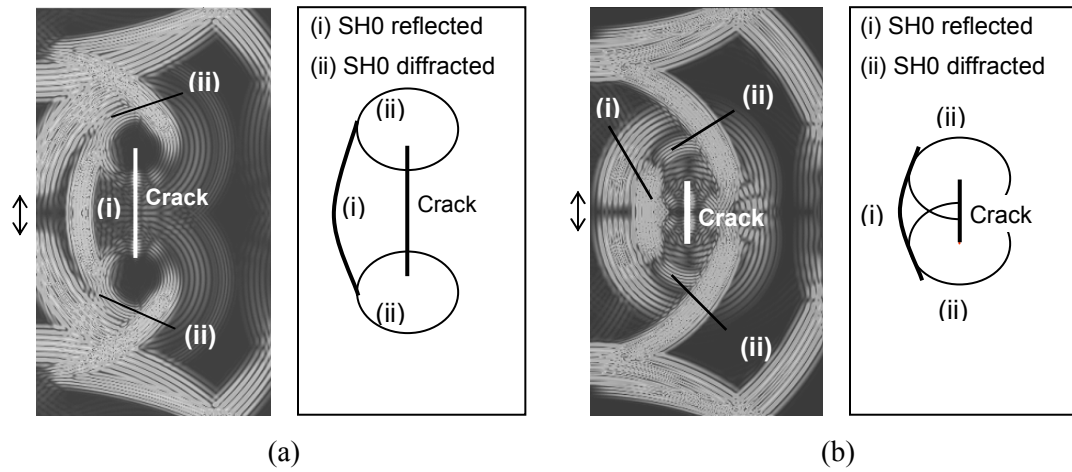
Figure 4.14 Interaction of SH0 with cracks of different lengths: (a) 20 λ_{SH0} and (b) 7 λ_{SH0} Snapshots of the contour of magnitude of resultant displacement obtained from FE simulations and line diagram focusing only on reflected and diffracted SH0 due to SH0 incident are shown. The grey-scale from black to white spans the range from the minimum to the maximum displacement amplitudes in the result.
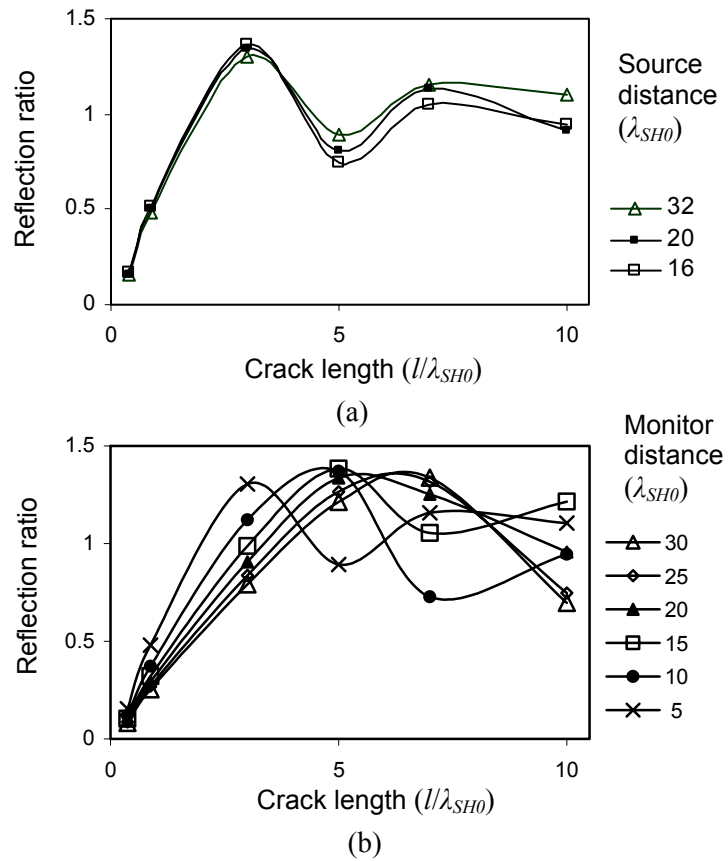
Figure 4.15 Reflection ratio-crack length plot (a) Monitored at 5 λ_{SH0} from the crack with range of source positions; (b) Source at 32 λ_{SH0} with range of monitoring positions.
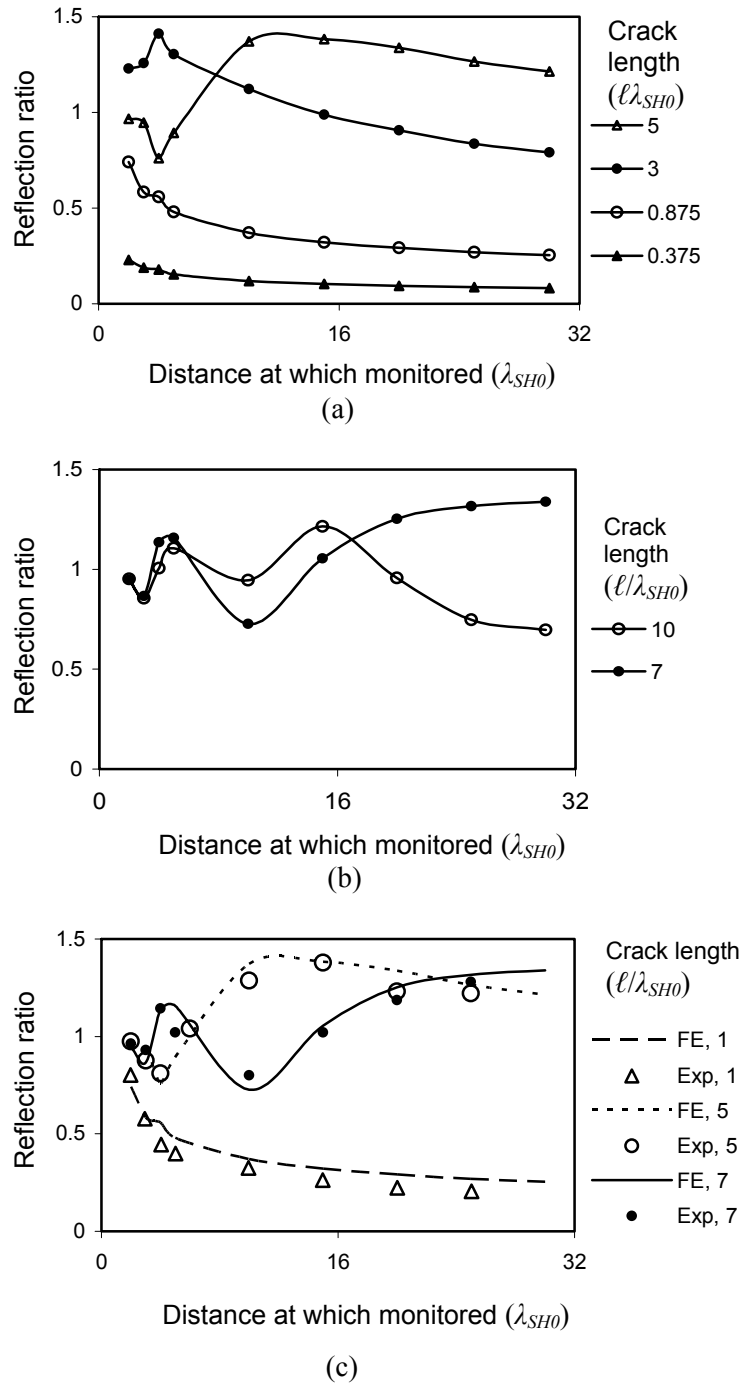
Figure 4.16 The reflection ratio plotted with the monitoring distance for increasing crack lengths; (a) and (b) show FE predicted values for small and large cracks respectively; (c) Comparison of FE with experimental measurements for 3 different slit lengths.

(a)

(b)
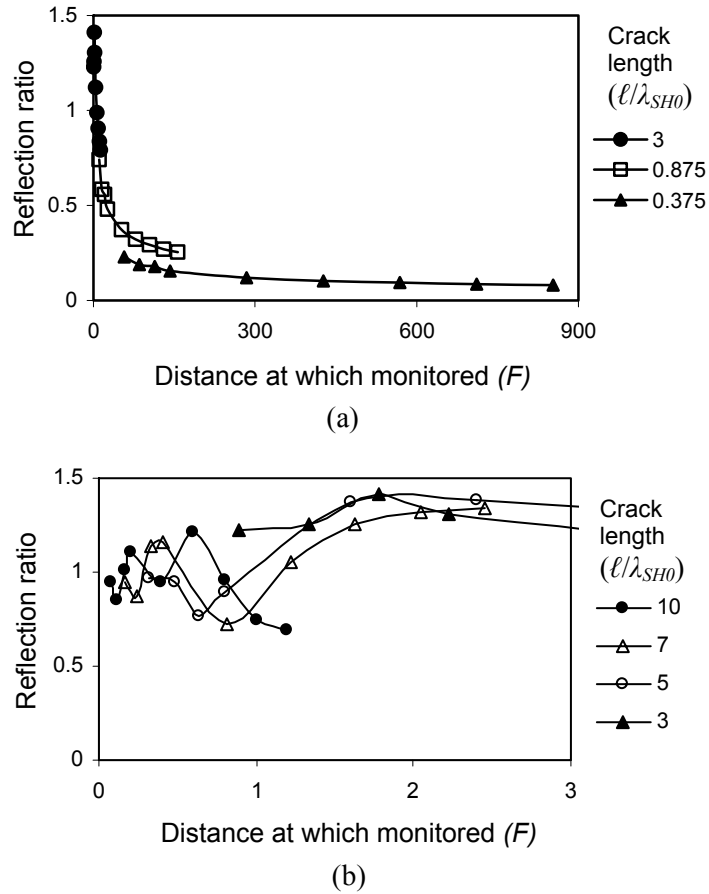
Figure 4.17 The reflection ratio is plotted with the monitoring distance normalized to the Fresnel parameter F for (a) Small cracks (b) Long cracks.
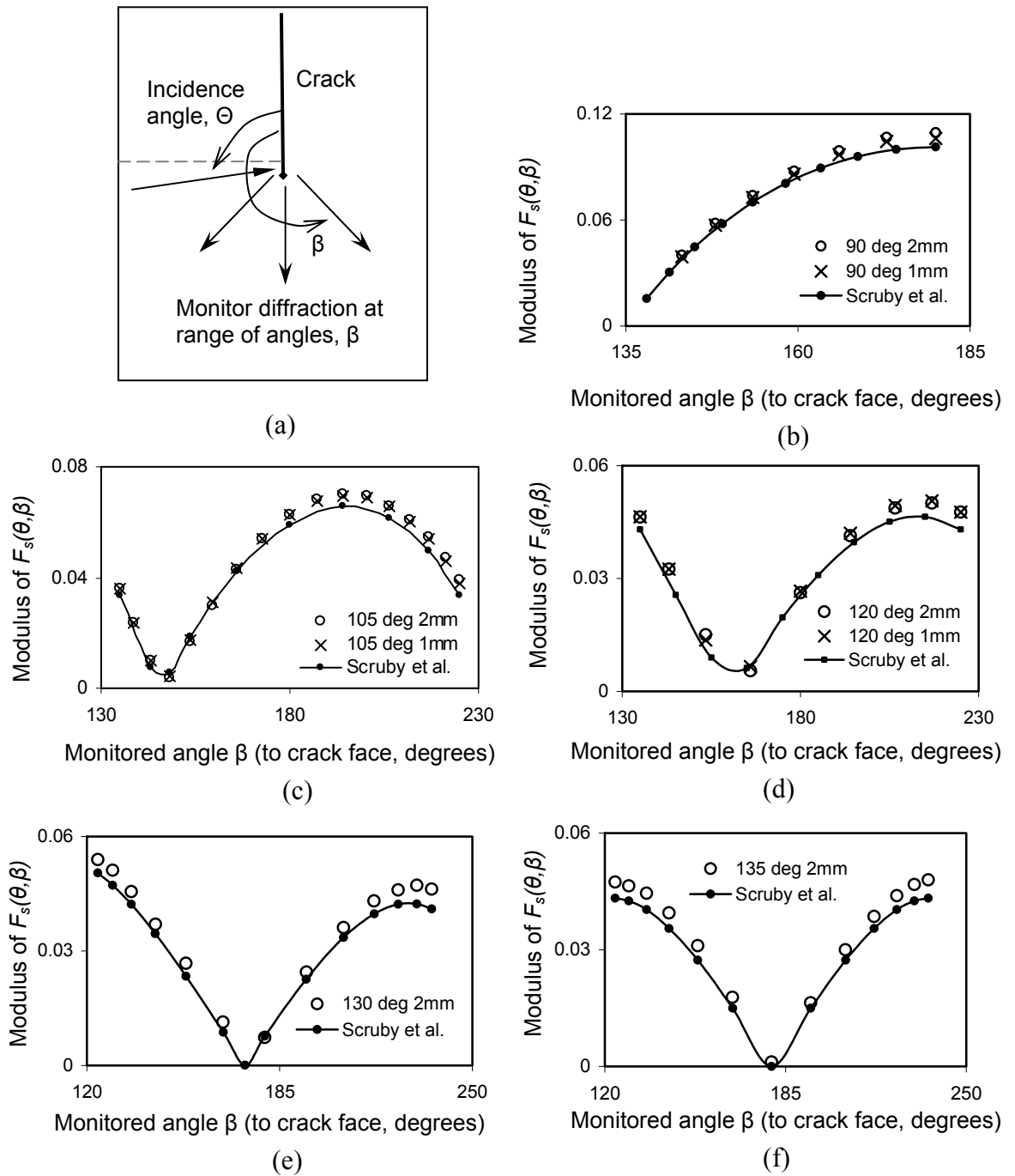
Figure 4.18 (a) Representation of the model generated for diffraction validation. (b) - (d) Comparison of results from FE simulations with two mesh sizes and the theoretical calculations presented by Scruby *et al.* [175]for incidence angle cases of 90^0, 105^0, 120^0; (e) and (f): comparison for incidence angles of 130^0 and 135^0, 2mm FE mesh.
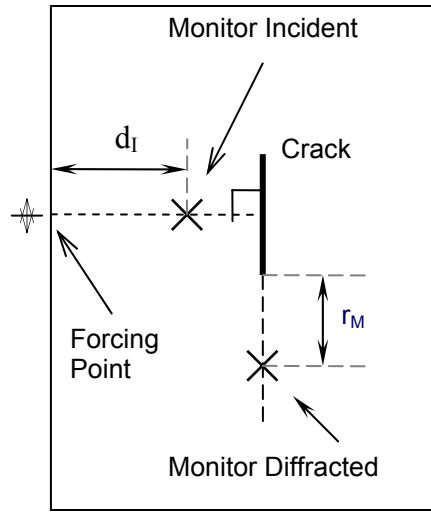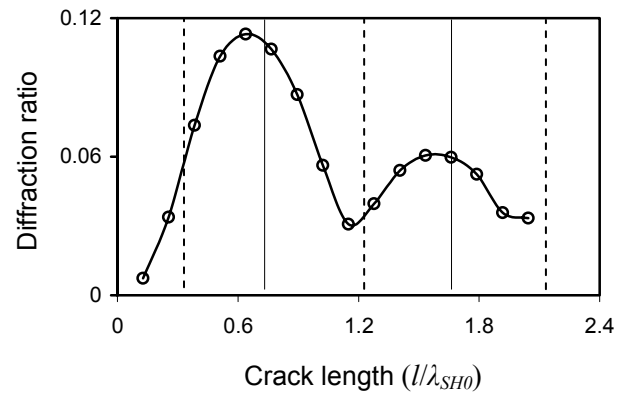
Figure 4.19 (a) The positions for monitoring incident and diffracted waves (b) The diffraction ratio calculated at 0.1 MHz for a point along the monitoring line, plotted with increasing crack length; the solid and dashed vertical lines are located at positions where the analysis in Section 4.4.2 predicts the peaks and troughs would be located.

Radiation of Rayleigh
waves travelling on the
crack surface

(i) SH0 incident

(ii) SH0 diffracted
at crack tip

(a)   (b)
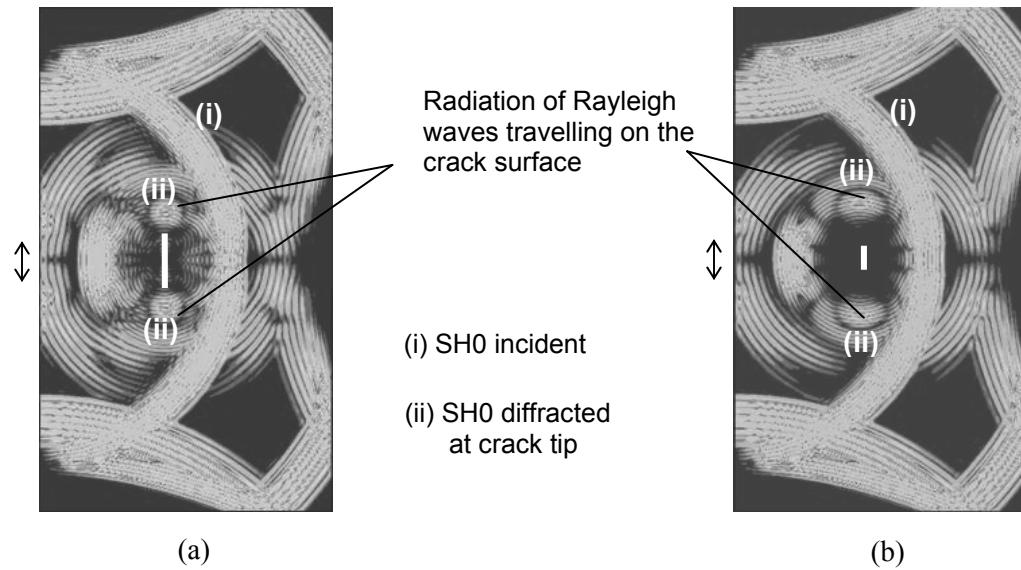
Figure 4.20 Snapshots of the contour of magnitude of resultant displacement for diffraction study for two different crack lengths: (a) 4 λ_{SH0} (b) 2 λ_{SH0}. The grey-scale from black to white spans the range from the minimum to the maximum displacement amplitudes in the result.
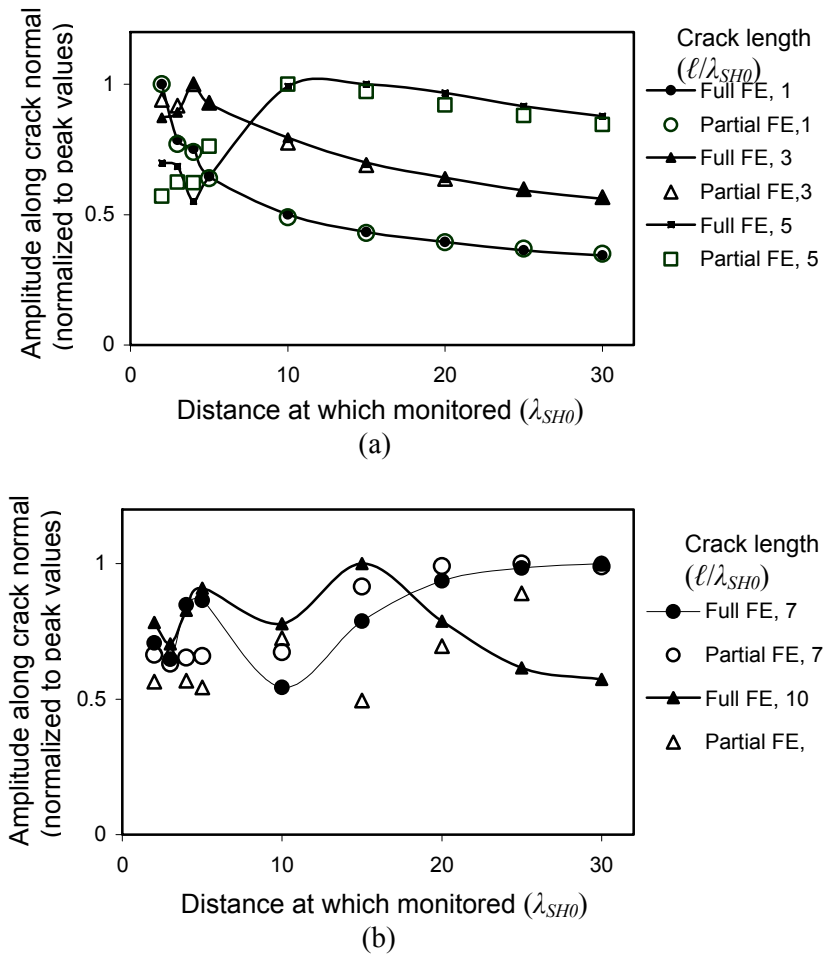
**Figure 4.21** U2 amplitude monitored along the symmetric normal to the crack obtained from FE simulations of cracks with one face loaded with parallel point forces: (a) plots the values for cracks 1, 3 and 5 λ_{SH0} long; (b) plots those for 7 and 10 λ_{SH0} long cracks. For each crack length case, the amplitudes are normalized to the maximum value and compared with similarly normalized results from full-FE studies of Figure 4.16.
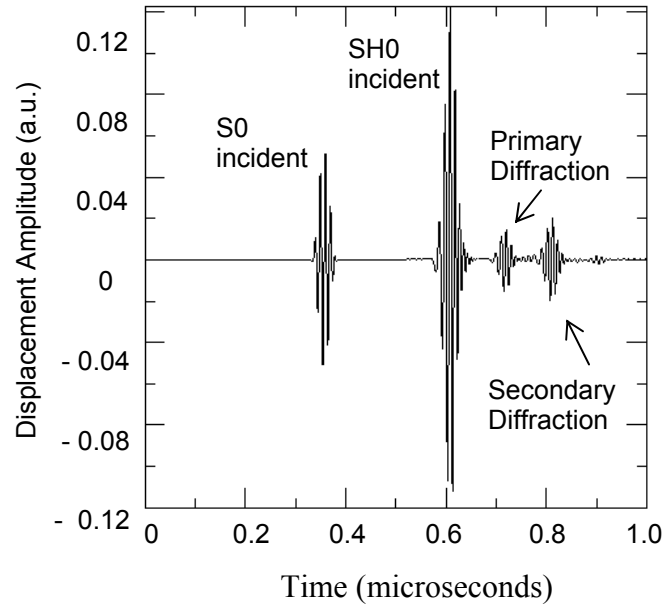
Figure 4.22 Typical time trace of the U1 component of displacement monitored along the crack line. The primary and secondary diffraction components are extracted from such a signal by time gating.
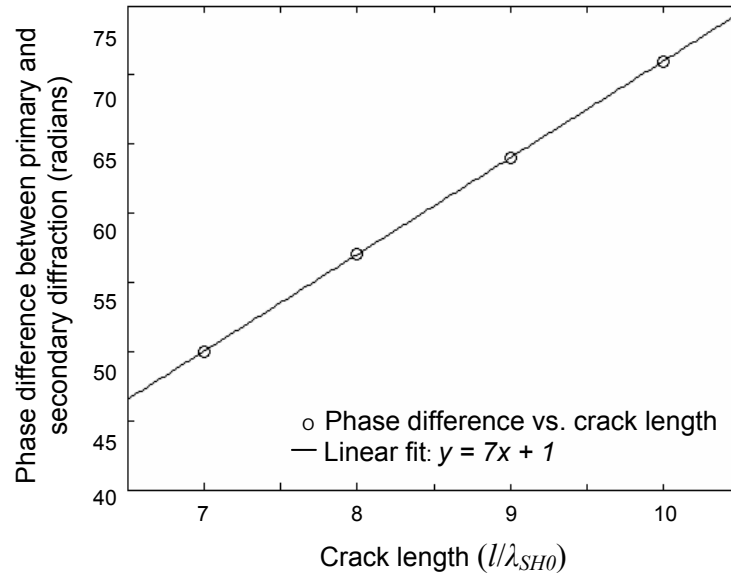
Figure 4.23 $\delta\phi_{P-S}^{edge}$ from FE simulations plotted with the crack length ℓ. A linear fit yields $\delta\phi_{P-S}^{edge} = 7\ell + 1$ if ℓ is expressed in λ_{SH0} or equivalently $\delta\phi_{P-S}^{edge} = 223.64\ell + 1$ if ℓ is in SI units.

Chapter 5

Low frequency SH0 mode interaction with through-thickness cracks: oblique incidence

5.1 Introduction

This is the second of the three chapters studying the general shorter range scattering of the fundamental shear horizontal guided wave (SH0) mode by ideal but finite surface-breaking cracks in isotropic plates. The attractiveness of the SH0 mode, requirement of cylindrical wavefronts and studies focusing on the spatial behaviour of scattering from through-thickness cracks were presented in Chapter 4. The scattering behaviour was studied in terms of the influence of the crack length on the specular reflection and diffraction fields. The studies were carried out using Finite Element (FE) analysis and general results were validated with experiments, while the diffraction modeling was verified by comparison with similar problems in bulk wave literature.

This Chapter continues with through-thickness cracks but considers general non-symmetric or 'oblique' SH0 mode incidence on the crack and studies the angular profile of the scattering. Essentially we will study how the scattering at different angles of observation varies due to different angles of incidence and crack lengths. The problem is complex, involving a number of parameters, including the angles of incidence and observation, the wavelength, the length of the crack, and the distances of the source and

the receiver from the crack. But findings from the simpler case of normal incidence from Chapter 4 clarified the physics of the scattering and helped identify the minimum number of independent parameters required. Both the source and the receiver are thus placed in the far-field of the largest cracks to be studied in a given model, in order to avoid spatial fluctuations in the scattered field. The crack length is stated in terms of the SH0 wavelength at the centre-frequency of the incident toneburst. The largest cracks studied were 5 wavelengths long so a distance of 15 wavelengths was sufficient. For the reflection studies, the parameters are further reduced by considering two complementary configurations involving the incidence and the observation angles, which together help understand the larger picture. For the diffraction studies only cracks that are long enough to allow the separation of primary and secondary diffraction from each other are considered. As in Chapter 4, the studies are carried out using Finite Element (FE) analysis and general results are validated with experiments, while the diffraction modeling is verified by comparison with theoretical results from bulk elastic wave scattering literature.

In what follows, first the procedure for FE simulations and the experiments is briefly described. Studies examining the angular behaviour of the reflection and diffraction are then presented and the results are discussed in the light of the physics of scattering. Finally these insights are used to consider the implications for imaging applications.

5.2 Methods

A detailed description of the configuration studied along with Group velocity dispersion curves and the general procedure for FE simulations and experiments is given in Chapter 4. For a self-contained presentation within this chapter, the key features are again quickly summarised here.

5.2.1 Studied configuration and general procedure for FE simulations

Figure 5.1 illustrates the configuration studied and the procedure for FE simulations. A finite length planar through-thickness crack of vanishing width is located in a thin isotropic plate. A point excitation [168] of in-plane force vibrating along the U2 direction is applied uniformly through the plate thickness and along a line which bisects the crack face at a given incidence angle. This generates incident circular-crested waves of the SH0 mode travelling principally in the U1 direction and those of the S0 mode, principally in the U2 direction. Away from their principal directions both modes exhibit a cosine angular decay of the displacement amplitude. At the low frequency-thickness of 0.1 MHz-mm chosen for the study, only these two in-plane modes can be present even after scattering. The S0 mode travels much faster than the SH0 mode and this fact is used to help time-gate its effects and study the scattering due to the latter in isolation. The A0 mode does not occur in this problem since it is not generated at the source and the through-thickness symmetry of the crack ensures that there is no mode conversion into it by the scattering. We then seek to study the angular profile of the SH0 mode reflected back from the crack face and diffracted around the crack tips (or edges). As shown in Chapter 4, this problem is equivalent to that of the scattering phenomena in the sagittal plane when bulk SV waves interact with strip-like internal cracks.

The problem was modeled by FE simulations in the two-dimensional domain with assumption of plane stress, implemented using the commercial package ABAQUS[149]. The plate thickness is assumed to be 1 mm so the frequency-thickness at an input frequency of say f_0 MHz would simply be f_0 MHz-mm. As demonstrated in Chapter 4, for through-thickness cracks, the results obtained at f_0 would be valid at any other frequency f_1 provided the dimensions are appropriately scaled by a factor of f_1/f_0. The mesh consisted of perfectly square elements, allowing for around 16 elements per SH0 wavelength, respecting the spatial discretization limit required for accurate modelling of wave propagation [146].Cracks of vanishing width were created by disconnecting nodes along adjacent elements. Material properties of aluminium were used for the reflection studies while those of steel were chosen for the study of diffraction so as to facilitate

comparison with the literature consulted, although there is only a small difference in the results obtained using these two properties. Absorbing layers with increasing damping (see Castaings *et al.*[170, 171] and Drozdz *et al.*[169] for details on the use of absorbing boundaries in FE analysis) were used around the edges of the plate in order to isolate the scattered SH0 waves.

The excitation consisted of a 5 cycle Hanning windowed toneburst centred at 0.1 MHz applied as a force vibrating in the direction parallel to the crack face at a single node. This generated the S0 and SH0 modes, with their principal directions parallel and perpendicular respectively to the applied force. Explicit time integration with a constant time step respecting the stability limit simulated the propagation of the modes. The default condition on the faces of the disconnected elements representing the crack is that of zero stress. Thus, the scattering from an ideal open crack was simulated.

5.2.2 General procedure for experiments

A point-like excitation was achieved by means of a plane wide-band piezoelectric shear transducer (Panametrics V301, 0.5 MHz center frequency) coupled to the plate through a small, thin (0.2 mm thickness, 3 mm diameter) brass disc. The source signal consisting of a 5 cycle Hanning windowed toneburst was generated by a Wavemaker (Macro Design Ltd., UK) instrument and centered at the required frequency.

The detection was achieved using a laser interferometer with dual differential fiber optic lines (Polytec OFV 2700) which are aligned at an angle of 30^0 to the surface of the plate, so that the difference between their signals gives the in-plane surface displacement. The aligner holding the two optical fiber leads is in turn, attached to a translatable rotary arm, a photograph of which is shown in Figure 5.2. The interferometer reads in-plane displacements perpendicular to the direction in which the arm points, and thus the SH0 mode propagating along that direction is picked up when the axis of the arm is vertically above the source point. A thin reflective tape was attached to the surface of the plate to

enhance the optical backscatter from the laser beams and the quality of measurement was improved by applying a band-pass filter and taking an average over 500 acquisitions.

Measurements were carried out on 0.5 mm wide slits of lengths 8 mm, 16 mm, 36 mm, and 65 mm cut in 1250 mm square standard aluminium (commercial purity, AA1050) plates of 1mm thickness. The center frequency of excitation was varied in order to obtain different values of slit-length in terms of the wavelength. The excitation and detection positions were also varied at each center frequency, so that they were located at a certain constant number of wavelengths away from the slit.

5.3 Specific studies and results

5.3.1. Angular influence on reflection

The angular influence on SH0 reflection is examined through two complementary sets of studies. First the case of normal incidence is considered and the angular profile of the total reflected field, both specular and diffuse, is studied as the crack length increases. In this context, the term 'specular' denotes the direction of mirror-like reflection as given by Snell's law and 'diffuse' refers to all the directions in which the waves can be reflected in the backscatter direction. Next the behaviour of just the specular reflection is studied at various other angles of incidence, again with increasing crack length. The overall angular profile of the reflected field can then be pictured by an intuitive superposition of the findings from these two sets of studies. For these reflection studies, the angles are defined in a counter-clockwise sense from the crack face symmetric normal, *to a ray pointing to or from its centre* along a required direction. For simplicity, large angles say $\alpha = 360^0 - \theta$ defined in this way are referred to as $-\theta$ instead, measuring clockwise from the symmetric normal. These details are shown in Figure 5.3.

The reflection behaviour was studied in terms of a frequency domain ratio of the resultant displacement of the reflected signal to that of the signal incident at the centre of

the crack face. The signals were compensated for beam-spreading such that the ratio from a straight edge would be unity. Thus

$$\text{Reflection ratio} \quad = \quad \frac{|R(\omega)| \cdot \sqrt{D + d_M}}{|I(\omega)| \cdot \sqrt{d_I}} \qquad (5.1)$$

where $R(\omega)$ and $I(\omega)$ are the frequency spectra of the reflected and incoming signals respectively, D is the distance between the source and the centre of the crack, d_M is the distance from the crack centre to the point where the reflection is monitored and d_I is the distance from the source to the point where the incident signal is monitored. (See Figure 5.3 for an example illustration).

5.3.1.1 Study of diffuse reflection due to normal incidence

Figure 5.3 illustrates the geometry used for the study of reflection at various diffuse angles θ_R for incidence angles $\theta_I = 0^0$. In the FE models, the excitation was located at a distance $D = 32\ \lambda_{SH0}$ (SH0 wavelengths at the centre frequency of the toneburst) away from the crack and such that the principal axis of the generated SH0 waves was aligned with SN, its symmetric normal. Since this is a normal incidence study, the FE time snapshots in Figure 4.8, Chapter 4 showing mode generation and interaction with the crack are illustrative of this present case as well. The U2 displacement of the incident waves was monitored along their principal axis at a distance d_I from the source: since this is the only displacement component here, it directly gives the total magnitude I. Reflected SH0 waves were monitored along one half of a vertical line at a distance d_{M0} $=15\ \lambda_{SH0}$ from the crack and bisected by its symmetric normal at a point called S. Starting from a point along this line at a distance of 17.6 λ_{SH0} from S, nodal displacements R_{U2} in the U2 direction were monitored at intervals of 1.6 λ_{SH0} all the way down to S. This yielded monitoring angles in the range $\theta_R = 0^0$ to 50^0 in intervals of 3^0-6^0. The resultant displacement R is related to R_{U2} as $R\cos(\theta_R) = R_{U2}$, so for each monitored point the resultant displacement values were obtained from the U2 values as $R = R_{U2} / \cos(\theta_R)$. The values in the range from -50^0 down to 0^0 were assumed to be identical to these due to

the symmetry in the configuration. The reflection ratio was then calculated using Equation (5.1) with $d_M = d_{M0} / \cos(\theta_R)$.

Experiments were carried out on slits of length 1 λ_{SH0} and 5 λ_{SH0} achieved using the required centre-frequency values on slits of lengths 8 mm and 36 mm respectively. Measurements were taken at the appropriate excitation and monitoring distances in terms of λ_{SH0} at the operating centre-frequency. Thus the transducer was located at a distance $D = 32\ \lambda_{SH0}$ from the crack and along SN, while the reflected signals were monitored along a vertical line (i.e. perpendicular to SN) which was $d_{M0} = 15\ \lambda_{SH0}$ from the crack. Measurements were taken at locations along this line which were at distances $d_M = d_{M0} / \cos(\theta_R)$ from SN while θ_R spanned the range from -45^0 to 45^0 in equal intervals of 9^0. At each of these positions, reflected SH0 waves were measured by positioning the axis of the rotary arm to be vertically above the centre of the slit face and then placing the arm along the required direction θ_R. This directly gives the magnitude of the reflected signal, R. The incident SH0 waves were monitored simply from the $\theta_R = 0^0$ measurement position when the rotary arm is placed along the symmetric normal to the slit and $d_{M0} = 15\ \lambda_{SH0}$ from the crack. The reflection ratio was then calculated using equation (5.1) using a procedure similar to that for the FE predictions.

Figure 5.4 (a) and 5.4 (b) show the plot of reflection ratio with θ_R obtained from FE simulations for small and long cracks respectively and Figure 5.4 (c) and 5.4 (d) present comparisons with experiments for two slit length cases. There is a very good agreement between the FE and experimental results.

The first observation is that as the crack length increases, most of the reflected energy is seen to be concentrated in a narrow region around the backscatter direction. An explanation for such behaviour follows from arguments we presented in Chapter 4, that in the configuration studied, the insonified face of cracks can be taken to behave like a simple ideal shear transducer focusing energy back. It is known that the field from a circular piston transducer is increasingly collimated with increasing piston radius (see for

instance, the text by Rose [38] pages 347-348). We do discern such a trend from Figure 7: as the crack length increases, the reflection tends to become increasingly concentrated around the direction of the crack's symmetric normal. We will discuss this idea in some more detail in Section 5.4.

5.3.1.2 Study of specular reflection at various incidence angles

Figure 5.5 illustrates the geometrical details for this study. In the FE models, excitation in the U2 direction was applied at a node along a vertical line at a fixed distance $x_I = 19$ λ_{SH0} from the crack face and skewed from its symmetric normal by a certain distance y_I. For each angle of incidence θ_I, $y_I \approx x_I \cdot \tan(\theta_I)$ and angles in the range 0^0 to 55^0 were considered. Figure 5.6 shows snapshots of the contour of magnitude of resultant displacement from FE simulations, showing the interaction of SH0 mode with the crack at an oblique angle of incidence. The U2 displacement of the incident SH0 waves was monitored along their principal axis at a distance d_I from the source, directly giving the total incident magnitude I. For specularly reflected waves at angles $\theta_R = -\theta_I$, nodal displacements R_{U2} in the U2 direction were monitored along a vertical line at a distance $x_R = 16\ \lambda_{SH0}$ from the crack and a distance $y_R \approx x_R \cdot \tan(\theta_I)$ from its symmetric normal. The resultant displacement values were then obtained as $R = R_{U2}/\cos(\theta_R)$. The values in the range from -55^0 to 0^0 were assumed to be identical with these due to the symmetry in the configuration. The reflection ratio was then calculated using Equation (5.1) with $D = x_I/\cos(\theta_I)$ and $d_M = x_R/\cos(\theta_I)$.

Experiments were again carried out on slits of 1 λ_{SH0} and 5 λ_{SH0} achieved using the required centre-frequency values on slits of lengths 8 mm and 36 mm respectively. Measurements were taken using exactly the same procedure for the FE simulations, with appropriate excitation and monitoring positions as in terms of λ_{SH0}. The reflection ratio was calculated using exactly the same procedure as that for the FE predictions.

Figure 5.7 (a) shows FE predicted values of the reflection ratio plotted with $\theta_R = -\theta_I$ and Figures 5.7 (b) and (c) present comparison with experiments for two slit length cases. We find a fairly good agreement between FE and experiments except at large angles of incidence where the crack tip diffraction contributes strongly to the reflected field but the tip of the experimental notch does not represent the crack tip very well.

We see that as the crack length increases, the highest specular reflection occurs at normal incidence, while almost no reflection is observed at a constant incidence angle of around 30^0 to the crack normal. In order to understand this behaviour, Figure 5.7(a) also overlays the reflection coefficient predicted for plane SV wave reflection from a straight edge. When a plane SV wave is incident on a straight edge, the reflected energy is repartitioned into SV and P waves traveling at angles given by Snell's Law. As the angle of incidence increases, more and more energy is delivered to the reflected P-wave. This happens until the first critical angle θ_{cr1} (around 29^0 for aluminium) at which the P-wave begins to graze through the surface of the edge and almost all the reflected energy goes into the P-wave. Beyond this angle energy is again diverted to the reflected SV wave and the reflection coefficient rises with the incidence angle until it settles at a steady value. What we see is that as the crack length increases the reflection behaviour from a finite crack increasingly tends towards that of the straight edge case. However, in the finite crack case, there is an interference characteristic of the presence of diffraction components which are not much separated in time. We will further discuss these findings and also their implications for imaging applications in Section 5.4.

5.3.2 Angular influence on diffraction

In the case of diffraction, attention is drawn to the validation of FE modeling in Chapter 4: for long single-tipped cracks, it was shown that the angular behaviour of diffracted SH0 waves agreed with that of bulk SV waves in a similar configuration. Thus we would expect that even for finite cracks, if we can isolate the primary diffraction at each of the two crack tips, its behaviour must correspond to that of bulk SV wave values for appropriate angles of incidence at a semi-infinite crack. Here we will scrutinise this

prospect and distinguish between two regimes of crack lengths, depending on whether or not the primary tip diffraction can be separated from secondary multiple diffraction components. For these diffraction studies, the angles are defined counter-clockwise from the crack face t*o a ray pointing to or from the crack tip in the required direction* as shown in Figure 5.8

First a case is taken up the where such a separation can be achieved. From this perspective, using a 5 cycle Hanning windowed toneburst excitation with a 100 kHz centre frequency, a crack longer than 7 λ_{SH0} is suitable and a value of 10 λ_{SH0} was used for the FE studies. As in Chapter 4, the study is performed by comparing the FE results with those from Scruby *et al.*[175] for the equivalent bulk SV wave problem with the help of the diffraction coefficient

$$\left|F_s(\theta,\beta)\right| = \frac{\left|\psi_D\right|}{\left|\psi_I\right|}\sqrt{\frac{r_M}{\lambda_S}} \tag{2}$$

where ψ_D is the frequency-domain amplitude of the monitored diffracted signal and ψ_I that of the wave incident at the crack tip, λ_S is the wavelength of bulk shear waves, r_M is the distance from the crack tip to the observation point, and θ, β are the angles of incidence and diffraction at the crack tip measured in a counter-clockwise sense from the crack face (see Figure 5.8 for an illustration)

The details of the model used are shown in Figure 5.8. A point source vibrating parallel to the crack face is located along its symmetric normal at a distance $D = 32\,\lambda_{SH0}$ from it. This causes the incidence of SH0 waves at the two crack tips (labelled Tip 1 and Tip 2) at angles θ_{I1} and θ_{I2} with the crack face. The U2 displacement of the incident waves I_{U2} was monitored at a distance d_o from the source along their principal axis: the amplitude incident at each crack tip n (n = 1 or 2) situated at a distance $d_{In} = D/\sin(\theta_{In})$ from the source would then be $\psi_{inc} = \frac{I_{U2}\sqrt{d_o}}{\sqrt{d_{In}}}\sin(\theta_{In})$. The U1 component of the diffracted signal D_{U1} was monitored at a range of angles θ_{Dn} around both the crack tips (n = 1 and 2) at radial positions d_M, with the resultant displacement obtained as $\psi_{dn} = D_{U1}/\cos(\theta_{Dn})$.

Equation (5.2) is then used to calculate the modulus of the diffraction coefficient and Figure 5.9 compares it with the results from bulk SV wave scattering literature [175, 176]. The FE results for angles around both the crack tips are mutually identical as predicted by, and in good agreement, with the theoretical calculations, thus confirming our expectation. The deviations from the theoretical predictions two are because of the unavoidable presence in the FE measurements, of unwanted signals which arrive together with the primary diffraction. We thus note that even for finite cracks, the angular pattern as well as the amplitude of the primary diffraction can be estimated quite well from the theoretical results for bulk SV waves.

In the case of shorter cracks, where the primary and secondary diffraction cannot be separated, the diffraction behaviour will be modulated by the presence of these additional components. Consistent trends may not exist in this case and due to the presence of multiple interfering components it would be advisable to work at a single frequency. As an illustration of a typically mixed signal, Figure 5.10a presents a time trace of the diffraction from the tip of a 5.25 λ_{SH0} long crack, for a normally incident SH0 wave; 5.10b shows the Fourier transform of just the mixed diffraction signal: interference due to multiple components can be observed.

5.4 Discussion

5.4.1 Understanding reflection behaviour

Trends similar to those of the results for guided SH0 wave reflection from through-cracks presented in Section 5.3 are known for the analogous problem of bulk shear wave scattering from strip-like cracks (see for ex. Danilov [182] and more recently, Caleap *et al.* [183]).). Chapter 4 employed a Kirchhoff-like approximation to demonstrate that cracks which are small compared to the distance from the source could be considered to behave as if uniform point shear sources were placed along the insonified face. Such a model was seen to be valid for cracks as long as 7 λ_{SH0} for the range of distances of

interest to this work. The observed angular behaviour of reflection for normal incidence, as noted in Section 5.3.1.1, with a narrowing down of the field at increasing crack lengths, does conform to such a model. Here FE simulations are again used to further quantitatively compare the behaviour of this Kirchhoff approximation based model with the reflection results from earlier full-FE studies. One face of the crack was loaded with parallel point forces and the generated amplitude was monitored at a range of angles around the crack face, using the same procedure as described in 5.3.1.1. This procedure was repeated for cracks of lengths 1, 3 and 5 λ_{SH0}, and for each crack length the monitored amplitude was normalized to the peak value: Figure 5.11 compares these with similarly normalized values for the same crack lengths from the results of Figure 5.4. We observe a very good agreement, revealing that the angular trend of reflection at normal incidence noted earlier does indeed arise from the insonified crack face exhibiting an ideal shear-source like behaviour.

The trend of reflections at other angles of incidence considered in Section 5.3.1.2 can also be understood from a Kirchhoff approximation framework. The main contribution to the reflection field can be said to be occurring from the central region of the crack, where there is very little interaction between the crack faces. Therefore, incident waves would reflect from the crack face locally as if it were an infinite straight edge and thus the reflection ratio would approach that from such an edge for increasing crack lengths. We indeed discern such a trend in Figure 5.7.

5.4.2 Implications for Imaging

We infer from the results of the normal incidence study that SH0 mode reflection from planar through-cracks is likely to be concentrated in a narrow angular band around the specular direction. The oblique incidence studies show that the specular reflection itself is strongest at normal incidence, but drops rapidly at other angles, reaching a distinct minimum around the material's first critical angle. These factors are likely to play a key role when defining the limits for the spatial resolution achievable by different imaging methods.

Provided that the crack and signal length are appropriate to allow the primary component to be isolated, the variation of diffraction with the angular position can be predicted from known solutions from bulk SV wave scattering literature. This can potentially yield important additional information such as the crack size and orientation which could be useful for more precise imaging. For smaller cracks, the presence of multiple interfering components means that a single frequency for calculations would be important.

5.5 Conclusions

This Chapter studied the interaction of low frequency SH0 waves with through-thickness cracks at non-normal angles of incidence. The interaction was studied in terms of both the reflection from the crack face and the diffraction at the crack tips. From two complementary sets of studies, it is seen that the reflection is mainly concentrated in a narrow angular band around the specular direction and that it approaches that from a straight edge for large cracks. The specular reflection itself varies quite rapidly with the incidence angle, and is strongest at normal incidence. If the crack is long enough to allow isolation of the tip diffraction at the operating frequency, an estimate of its amplitude and angular variation can be obtained from known solutions of bulk SV wave canonical scattering problems. The next Chapter will further extend this line of investigation and consider part-through instead of through-thickness cracks.
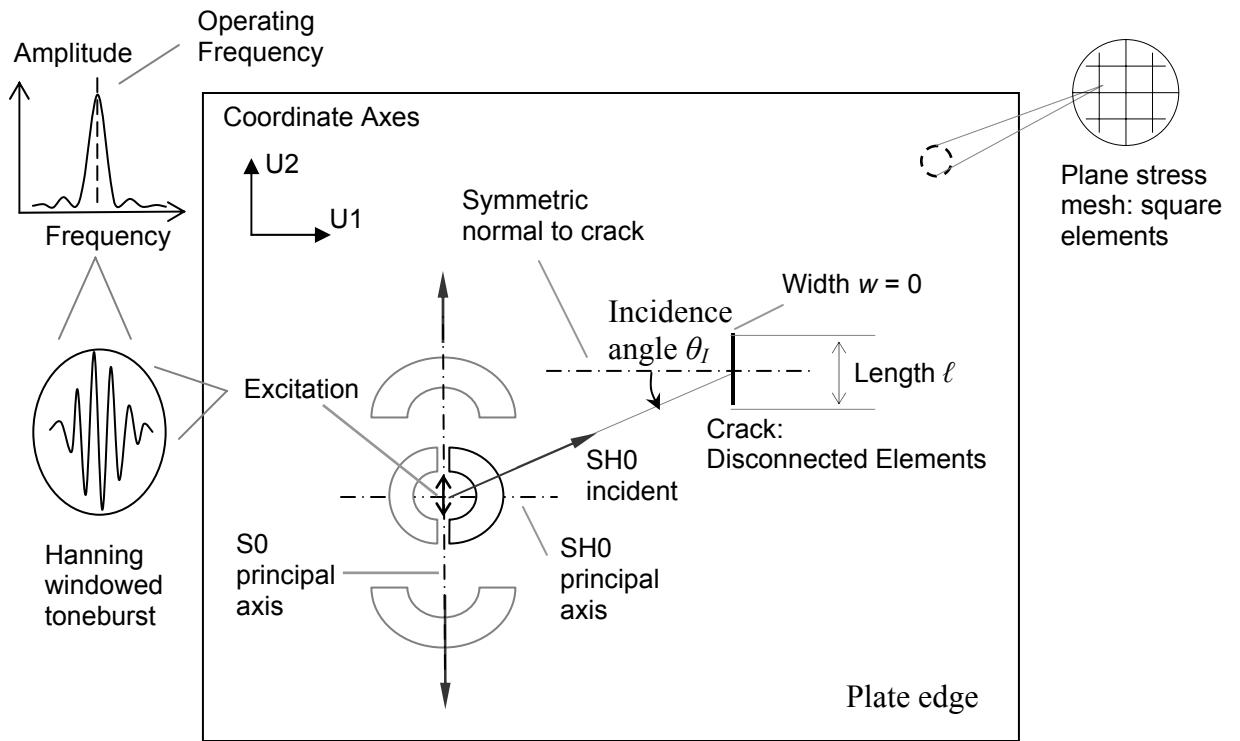
Figure 5.1 Details of the configuration studied. The SH0 mode is generated such that a line from the wave source bisects the crack face at a required angle.
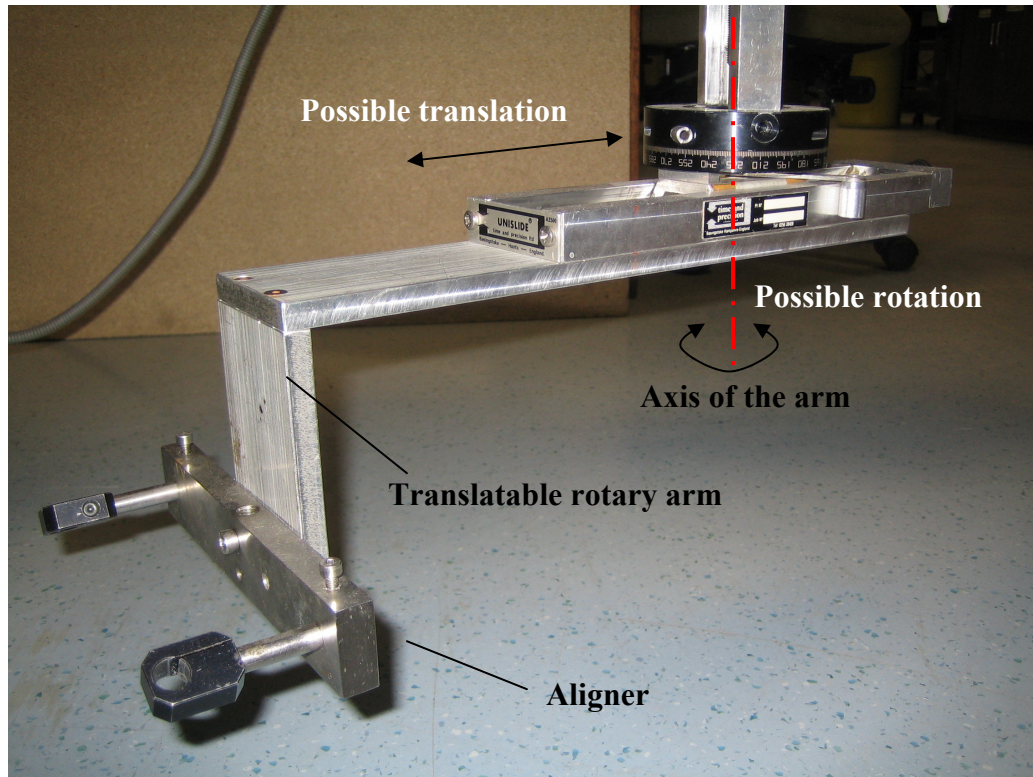
Figure 5.2 Close-up photograph of the translatable rotary arm which holds the aligner for the optical fiber leads.
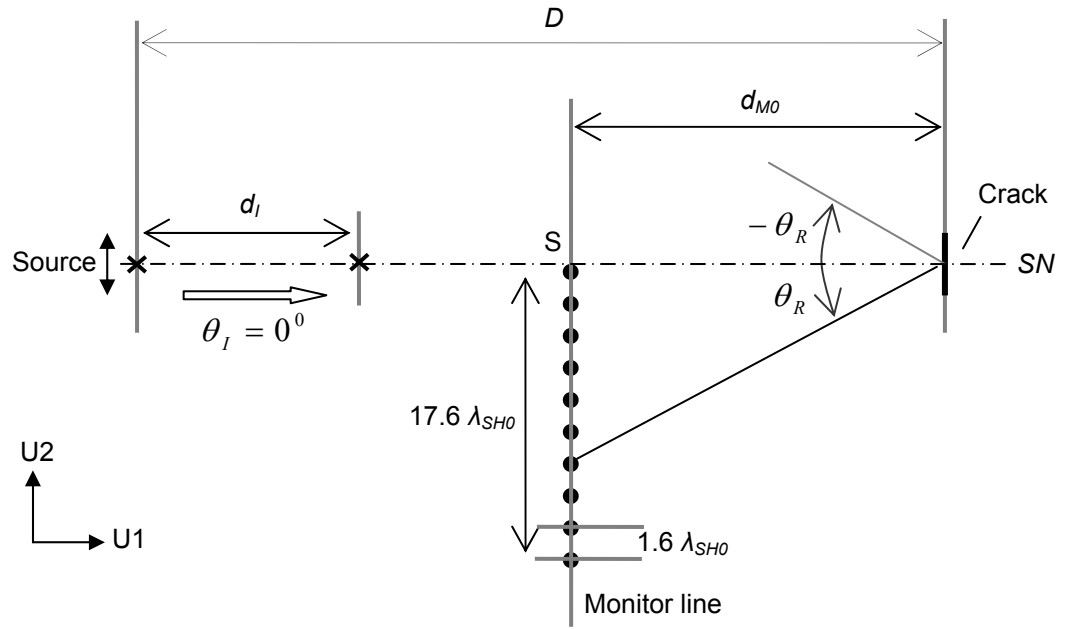
Figure 5.3 Geometry for study of reflection at angles θ_R for an incidence angle $\theta_I = 0^0$.
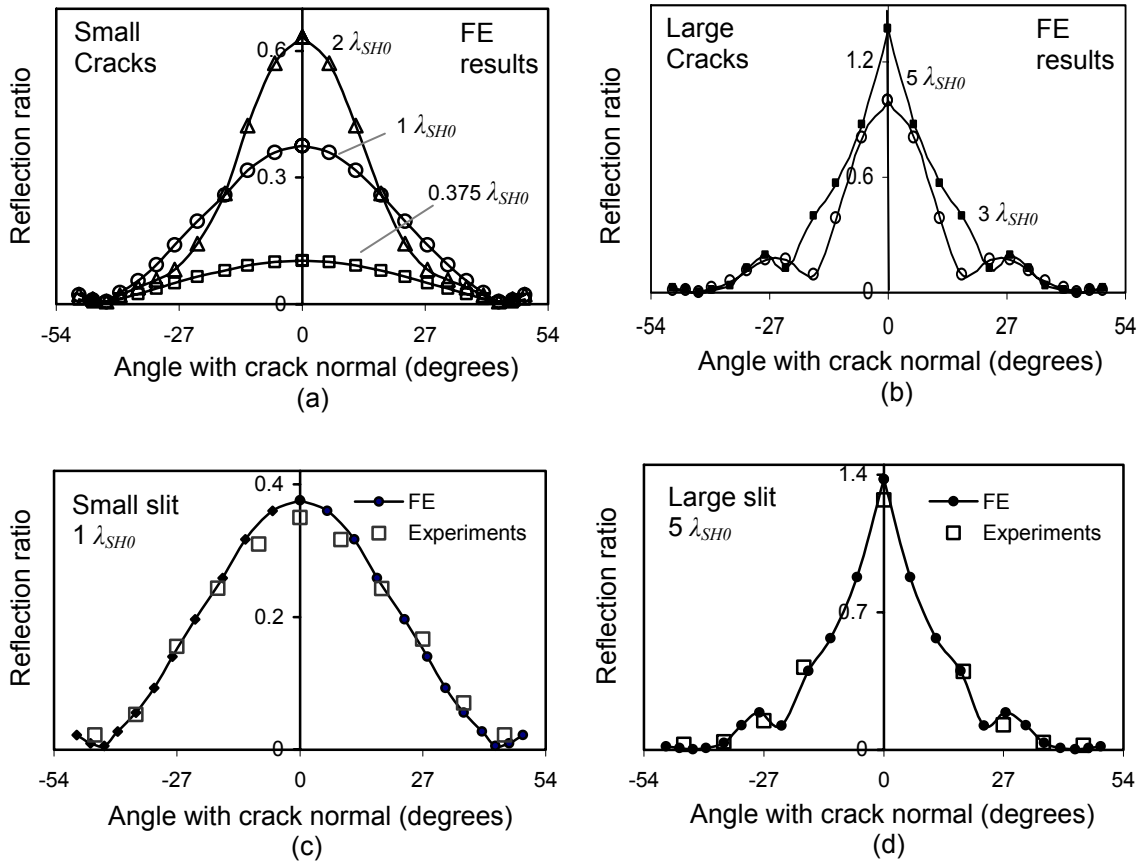
Figure 5.4 (a) and (b) Plot of reflection ratio from FE simulations with θ_R for $\theta_I = 0^0$, for small (0.375, 1 and 2 λ_{SH0}) and large (3 and 5 λ_{SH0}) cracks respectively; (b) and (c): comparison of FE results with experiments for two slit length cases of 1 and 5 λ_{SH0}.
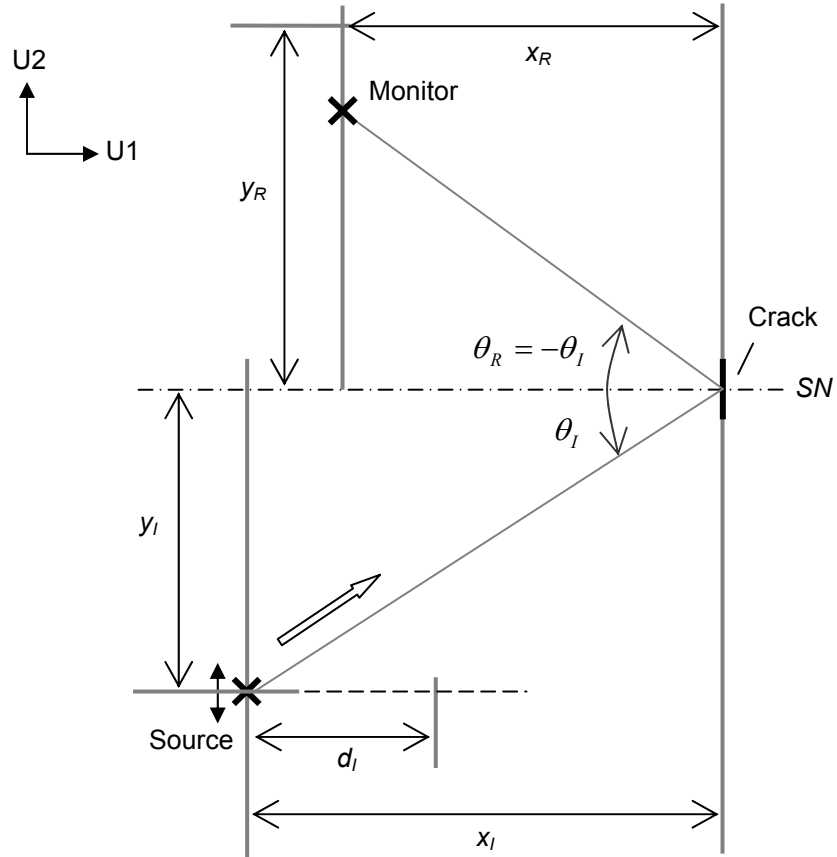
Figure 5.5 Geometrical details for the study of specular reflection for oblique incidence angles.

(a)   (b)

(c)   (d)
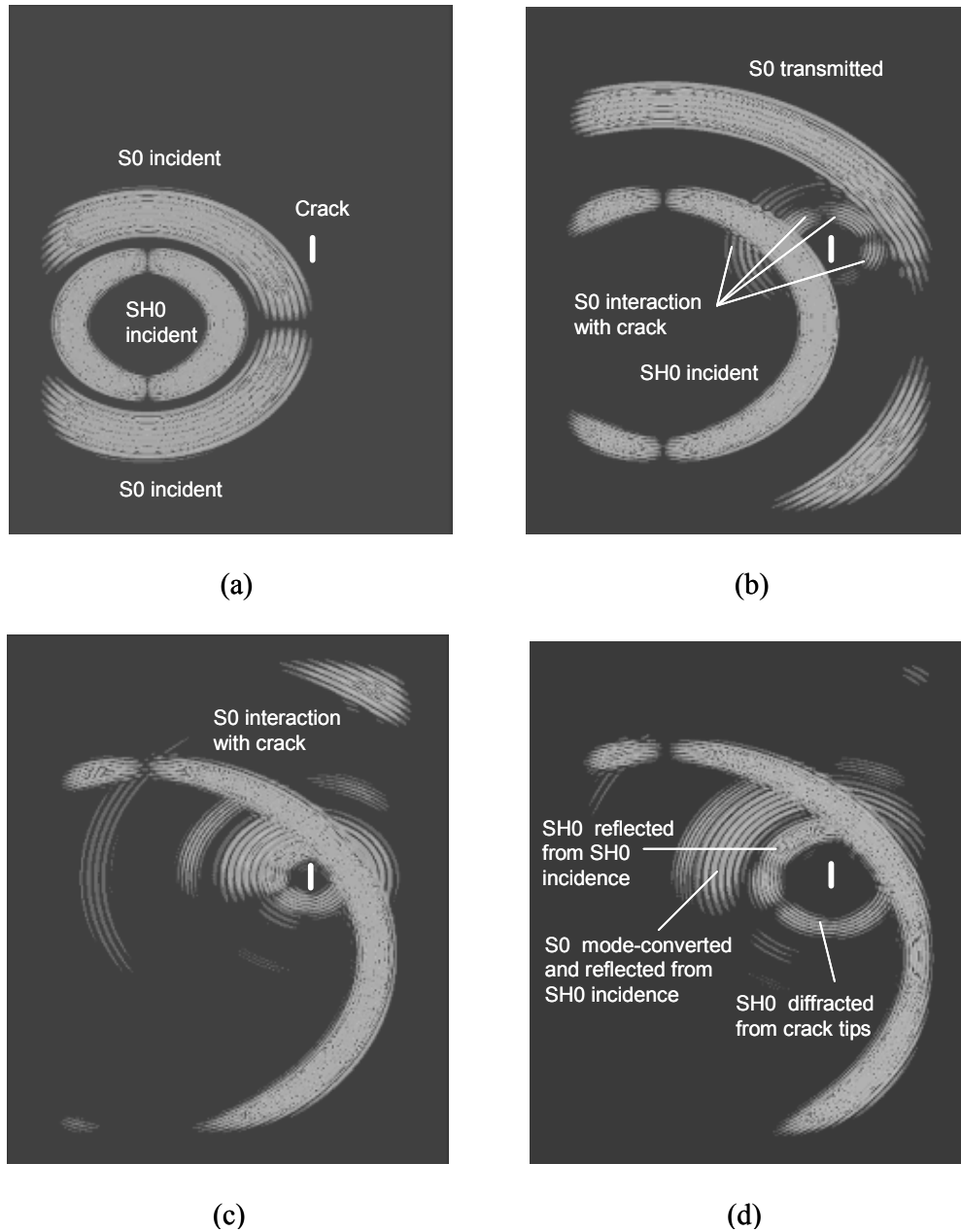
Figure 5.6 Snapshots of the contour of magnitude of resultant displacement from FE simulations: oblique angle of incidence. Absorbing boundaries present all around the actual plate isolate the interaction of the waves with the crack. (a) Shows the generation of the waves (b) shows the weak interaction of the S0 mode with the crack while (c) and (d) show the interaction of the SH0 mode with the crack.

(a)

(b)   (c)
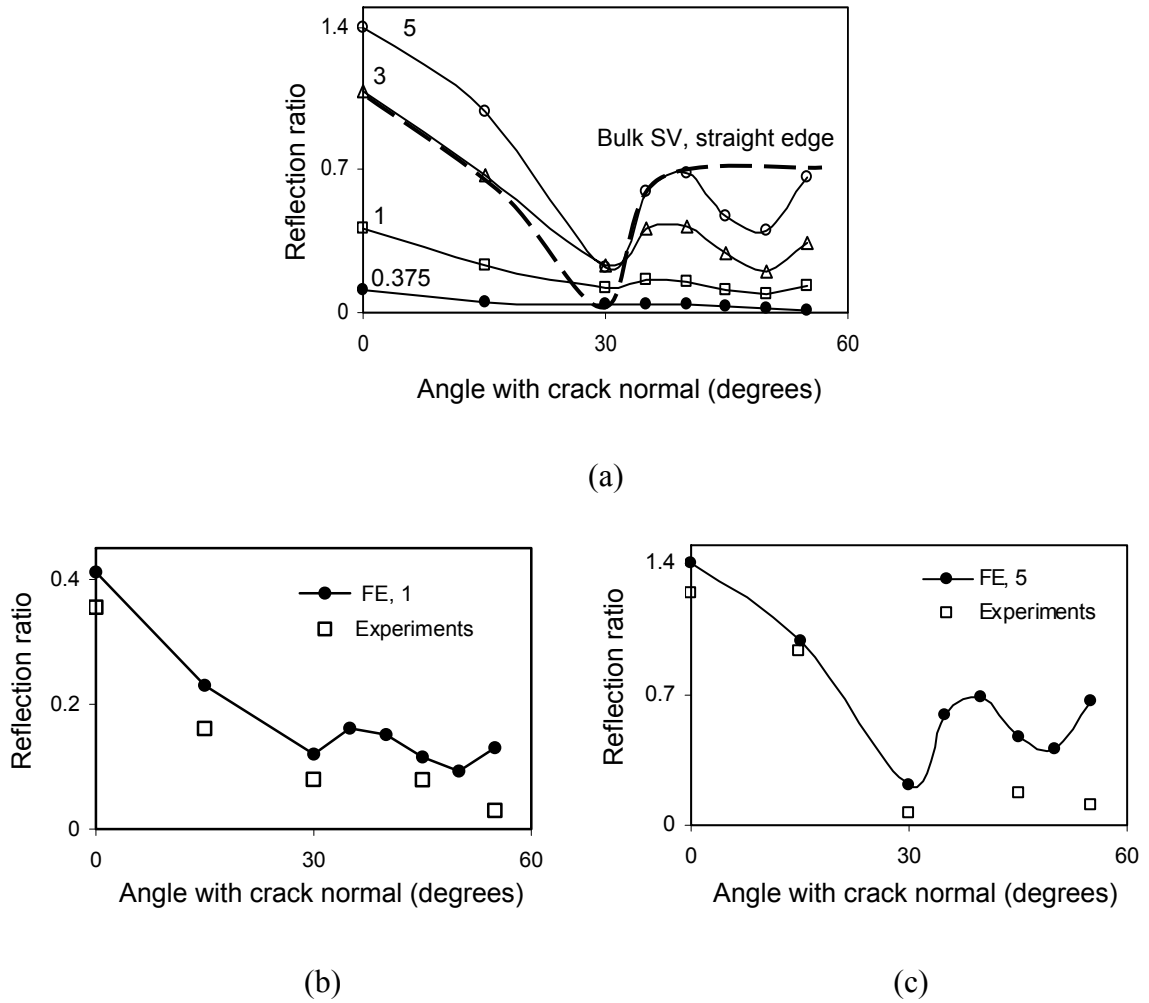
Figure 5.7 (a) FE predicted values of the reflection ratio plotted at $\theta_R = -\theta_I$: crack lengths are indicated in terms of λ_{SH0}; dashed lines show the reflection coefficient for plane bulk SV wave reflection from a straight edge; (b) and (c): comparison with experiments for two slit length cases of 1 and 5 λ_{SH0}.
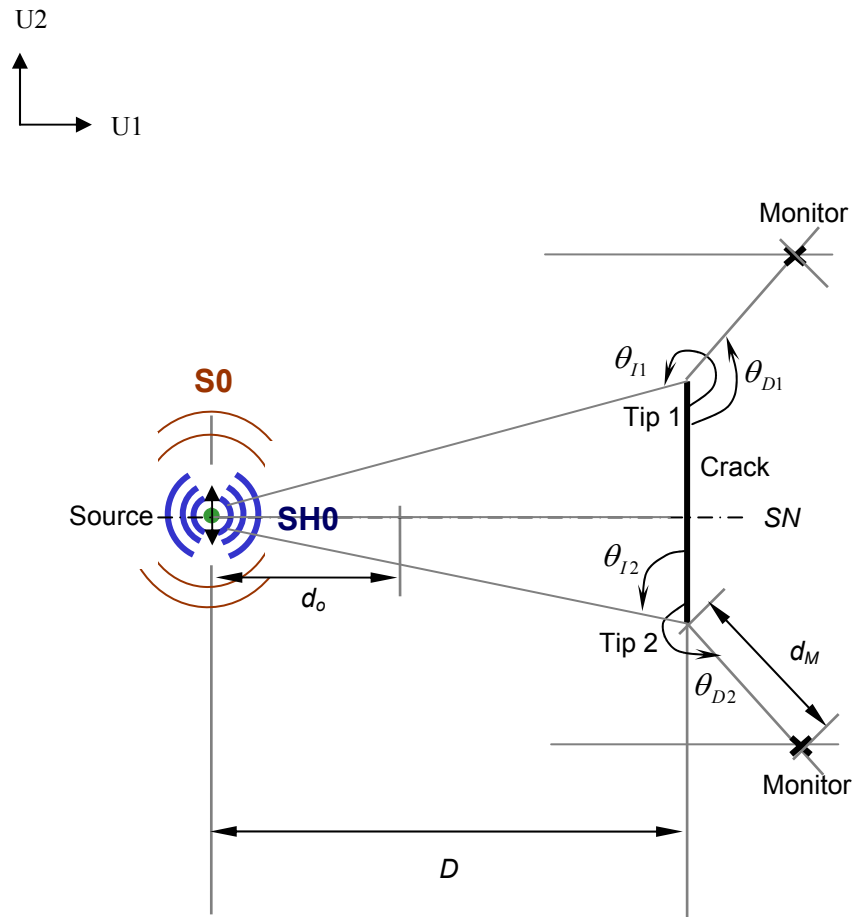
Figure 5.8 Details of the model used for diffraction study (see text for definition of the different terms).
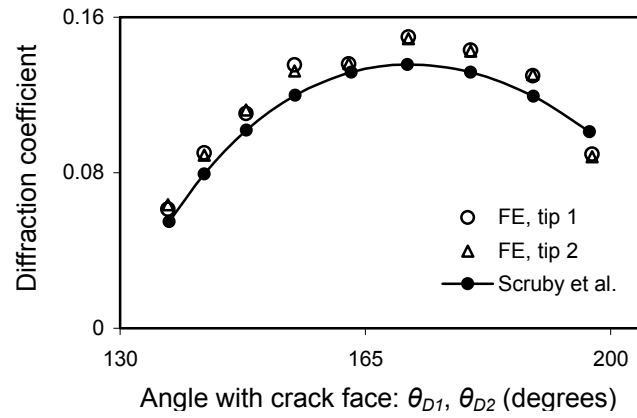
Figure 5.9 Modulus of diffraction coefficient from FE simulations of SH0 waves incident symmetrically at a 10 λ_{SH0} long through-thickness crack, for the primary diffraction at both the crack tips, compared with theoretical results from bulk SV wave scattering literature [175, 176].
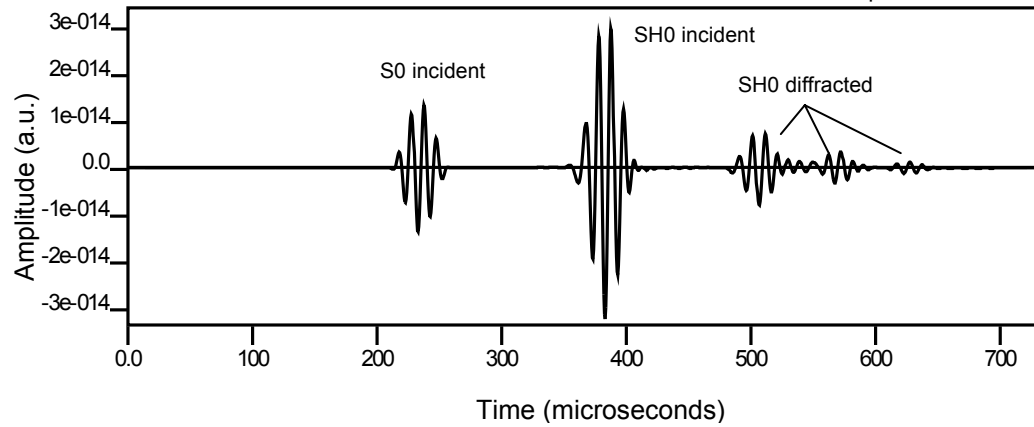
(a)
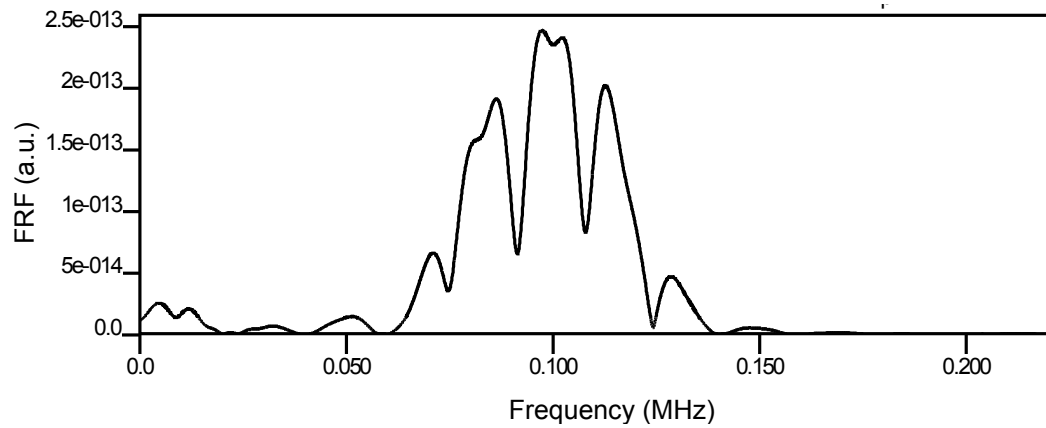
(b)

Figure 5.10 (a) Time trace of diffraction from the tip of a 5.25 λ_{SH0} long crack for a normally incident SH0 wave; (b) Fourier transform of just the mixed diffraction components.

(a)

(b)   (c)
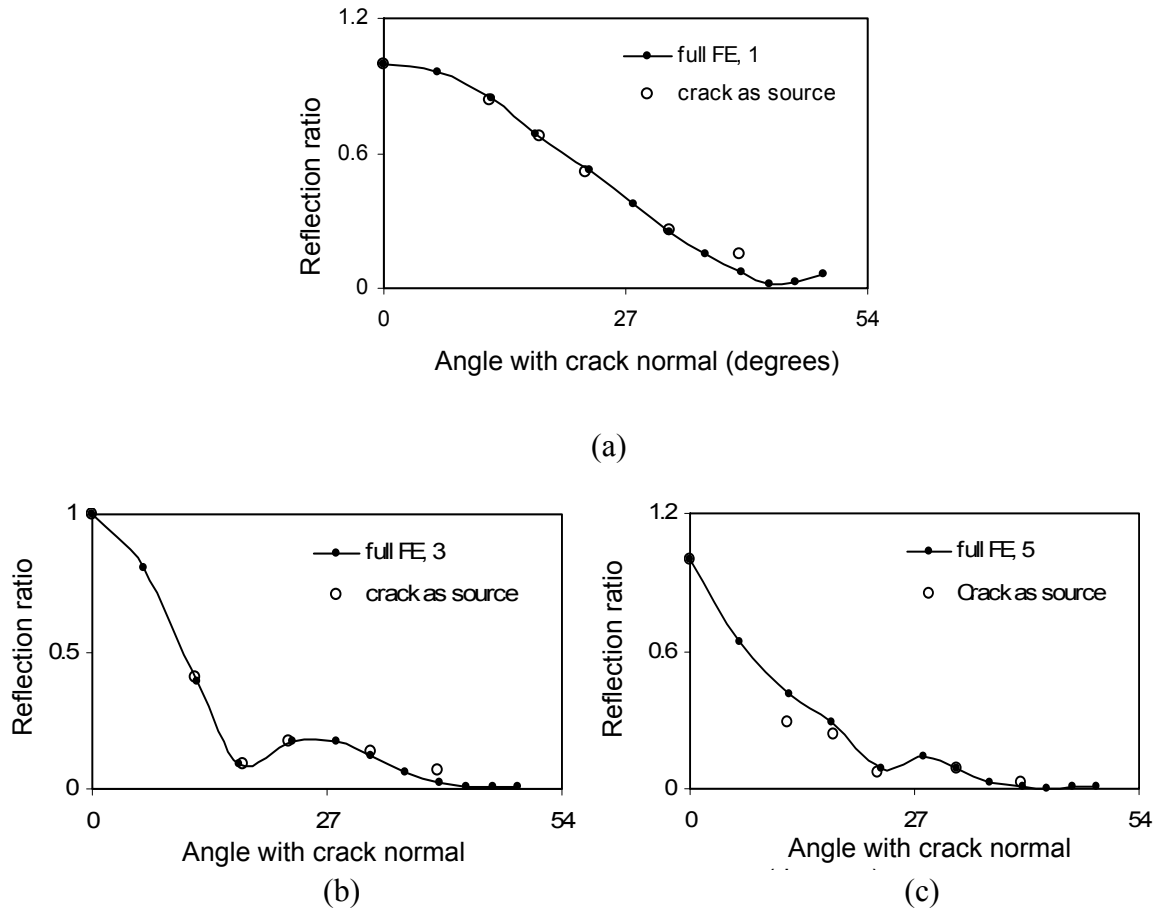
Figure 5.11 Comparison of amplitudes from part-FE simulation of crack face loaded with parallel point forces and reflection results from Figure 5.4. In both cases, the values are normalized with the peak value, giving a unit maximum. (a) (b) and (c) show results for cracks of lengths 1, 3 and 5 λ_{SH0}.

Chapter 6

Low frequency SH0 mode interaction with part-thickness cracks

6.1 Introduction

This is the last Chapter studying the interaction of cylindrical crested fundamental shear horizontal (SH0) guided waves with finite cracks in an isotropic plate, in the context of array imaging using ultrasonic guided waves [43, 155]. The background to this work and studies on the scattering by through-thickness cracks were presented in Chapters 4 and 5. The interaction was studied in terms of both the reflection from the crack face and the diffraction at the crack tips or edges. Finite Element (FE) analysis was used to obtain results which were verified by experiments and comparison with those from similar problems in bulk elastic wave scattering literature.

This Chapter further extends the investigation to consider part-through instead of through-thickness cracks. Although only the symmetric incidence case and the reflection behaviour are studied, general conclusions are drawn for the scattering of the SH0 mode based on the relationship of the results with those for through-cracks. In doing so, the general method in Chapters 4 and 5 is again adopted: first the influence of crack length and the monitoring distance on the specular reflection is examined and then the angular profile of the diffuse reflection is studied. Here 'specular' refers to the direction of

mirror-like reflection as given by Snell's law and 'diffuse' to all the directions in which the waves can be reflected in the backscatter direction. To facilitate comparison of results, the same excitation and monitoring distances from the crack as those used for similar studies in the through-thickness case are maintained. For each crack length, different crack depths and operating frequencies are considered, to gain an understanding of the reflection behaviour. Studies on the relation of the scattering from part-thickness cracks and notches have shown [19] that notches of extremely small axial extent or width (< 0.01% of the wavelength) are necessary to approximate the behaviour of cracks. Instead of attempting to create such small-width notches, separate FE studies with finite-width notches were performed for experimental validation of the modeling.

In the following, Section 6.2 describes the configuration studied and the general procedure for FE simulations and experiments. Section 6.3 deals with specific studies, taking up in order, the influence of the crack length and measurement location on the specular reflection, the angular profile of the reflected field and finally the validation of FE modeling with experiments. In Section 6.4 the results are analyzed and an empirical formula for the scattering of the SH0 mode by part-thickness cracks is sought. Finally the findings are discussed and conclusions are drawn in Section 6.5.

6.2 Methods

6.2.1 Configuration studied

Figure 6.1 shows the details of the configuration studied and those for the FE simulations described in the next part of this section. A finite length ideal (planar, zero-width) surface-breaking part-thickness crack is located in a thin isotropic plate. A line excitation consisting of in-plane point forces vibrating in the U2 direction applied uniformly through the plate thickness generates [168] incident circular-crested waves of the SH0 mode principally along U1 and those of the S0 principally along U2. The operating frequency-thickness values are always low enough so that only fundamental modes can be present even after scattering. Due to the through-thickness symmetry of the excitation,

the fundamental antisymmetric Lamb mode (A0) is not generated at the source. The SH0 mode is generated such that it propagates principally along the crack's symmetric normal. The fact that the S0 mode travels much faster than the SH0 mode at these frequencies is used to time-gate its effects and although some A0 will be generated by mode conversion at the scattering, its modal properties are exploited so that it is not picked up at the monitored positions. Thus the SH0 reflection from the crack face solely due to the SH0 mode incident at it is studied in isolation.

We will then examine successively, the influence of the crack length, depth and measurement position on the reflection using FE simulations validated with experiments. We observed in Chapter 4 that SH0 mode scattering from through-thickness cracks which are not too small (cracks of length ℓ such that $k_{SH0}\ell > 1$ where k_{SH0} is the wavenumber) can be described well by the Kirchhoff approximation. This means that the faces of the crack do not interact and reflection would be governed by the secondary sources placed on the insonified face. Thus the results at a frequency f_0 would be valid at another frequency f_1 provided the crack length and the other dimensions are scaled appropriately by a factor of f_1/f_0 by which the wavelength is scaled. But such simple scaling will not work with part-thickness cracks since their faces interact in a more complex frequency-dependent manner and so the Kirchhoff-approximation does not hold except at high frequencies: therefore the influence of the operating frequency on each of these cases is also studied.

The cracks that occur in practice will be more complex, with features such as roughness, curving and closure of the faces, branching at tips etc, but we wish to obtain trends which might still be valid. Also, uniform width notches were created for experimental validation of FE simulations. Mention must be made here of the analysis on the relationship between cracks and notches in Demma *et al.* [19], which brings out an important difference in the scattering behaviour of a through-thickness notch from that of a part-thickness one must be. Only the insonified face of the through-thickness notch participates directly in the scattering process. But with a part-thickness notch both faces contribute and the scattered packet consists of reflections from the first face followed by

multiple reverberations across the width of the notch. Because of this, the scattering from a part-thickness notch is strongly influenced by the operating frequency.

Thus a through-thickness crack can be well represented in its scattering by a through-thickness rectangular notch or slit with suitably small axial extent (width). But a part-thickness notch fails to represent a part-through crack unless it has width less than 0.01% of the operating wavelength. Since it is difficult to create such a small uniform notch, we decided to perform separate FE studies with notches for comparison with experiments. The configuration studied in this case remains the same, except that the crack is now replaced by a finite width notch. The dimensions of the notch and the operating frequency will all have a combined influence in this study.

6.2.2 General procedure for Finite Element simulations

The problem was simulated by FE analysis in the general three-dimensional domain implemented using the commercial package ABAQUS [149]. The model plate was assumed to be 2 mm thick and material properties of aluminium were used, simply in order to match the experimental plate dimensions and properties. The mesh consisted of perfectly cubic 8 noded linear continuum elements and four elements were used to represent the thickness. This allowed for around 16 elements per SH0 wavelength at the highest centre-frequencies used, thus respecting well the spatial discretization limit required for accurate modelling of wave propagation [146]. Cracks of vanishing width were created by disconnecting nodes on elements representing the adjacent faces. Notches of 0.5 mm width (equal to the size of an element) were created by removing columns of elements from the mesh. Absorbing layers with increasing damping (or *ALID*, see Drozdz *et al.* [169]; see Castaings *et al.* [170, 171] for details on the use of absorbing boundaries in FE analysis) were used around the edges of the plate in order to isolate the scattered SH0 waves.

The excitation consisted of a 5 cycle Hanning windowed toneburst centred at the required frequency and applied as a force in the direction parallel to the crack face at a

single line formed by all nodes through the thickness. This generates the S0 and SH0 modes, with their principal directions parallel and perpendicular respectively to the applied force and ensures that no A0 mode is generated. Explicit time integration with a constant time step respecting the stability limit [146] simulates the propagation of the modes. The default condition on the faces of the disconnected elements representing the defect is that of zero stress. Thus the scattering from an ideal open crack or uniform rectangular notch is simulated.

As in Chapters 4 and 5, the reflection behaviour was studied in terms of the frequency domain ratio of the beam-compensated reflected and incident signals, given as

$$\text{Reflection ratio} \quad = \quad \frac{|R(\omega)| \cdot \sqrt{D + d_M}}{|I(\omega)| \cdot \sqrt{d_I}} \qquad (6.1)$$

where $R(\omega)$ and $I(\omega)$ are the frequency spectra of the resultant displacement obtained from the reflected and incident signals, D is the distance between the source and the centre of the crack, d_M is the distance from the crack centre to the point where the reflection is monitored and d_I is the distance from the source to the point where the incident signal is monitored. (See for instance, Figure 6.4 for an illustration).

The reflection ratio for a fully through-thickness crack was obtained at 0.4 MHz-mm and the results agreed very well with the previous plane-stress studies obtained at 0.1 MHz-mm, thus assuring us of the integrity of the definition of the crack. As expected, the results for the through-thickness crack were identical for different frequencies, with the dimensions suitably scaled.

6.2.3 General procedure for experiments

The experimental set-up was identical to the one described in detail in Chapters 4 and 5. A point-like excitation was achieved by means of a plane wide-band piezoelectric shear transducer (Panametrics V301, 0.5 MHz center frequency) coupled to the plate through a small, thin brass disc. The source signal consisting of a 5 cycle Hanning windowed

toneburst was generated by a Wavemaker (Macro Design Ltd., UK) instrument and centered at the required frequency. The detection was achieved using a laser interferometer (Polytec OFV 2700, with dual differential fiber optic lines) measuring the displacement component parallel to the surface of the plate through a reflective tape to enhance the optical backscatter. The quality of each displacement measurement was enhanced by applying a band-pass filter and taking an average over 500 acquisitions.

Measurements were carried out on two 0.5 mm wide, 10 mm long notches of depths 1 mm and 1.5 mm respectively, cut in 1250 mm square standard aluminium plates of 2 mm thickness. The center frequency of excitation was varied in order to obtain different values of frequency-thickness and notch-length in terms of the wavelength. The excitation and detection positions were also varied at each center frequency, so that they were located at the same number of wavelengths away from the notch as in the FE simulations.

6.3 Specific studies and results

6.3.1 Study of specular reflection

First the influence of the crack length and measurement position on the specular reflection is studied, as the crack depth and the operating frequency are varied. Since this is a symmetric incidence problem, the direction of specular reflection lies along the symmetric normal to the crack face. In this direction the scattered waves of the A0 mode have displacements entirely in the U1-U3 plane, while those of the SH0 mode have displacements entirely in the U2 direction. Thus it was enough to monitor the U2 displacements on the surface of the model plate, in order to measure the reflected SH0 waves without contamination by the A0 mode. As mentioned earlier, the S0 mode travels much faster than the other two modes so that its effects can be time-gated out and thus SH0 mode scattering is studied exclusively.

6.3.1.1 Influence of crack length

A number of models with cracks of lengths up to 5 λ_{SH0} (SH0 wavelengths at the centre frequency of the toneburst) were set up to understand the dependence of the SH0 reflection over the length of the crack. For each crack length, models with three different crack depths, 25%, 50% and 75% of the plate thickness were created. Further, in order to study the influence of the frequency-thickness, the simulations were performed with centre-frequencies of 200 kHz, 300 kHz and 400 kHz for each crack depth. The excitation was located at a distance of 16 λ_{SH0}, while nodal displacements in the U2 direction were monitored 5 λ_{SH0} from the crack and along its symmetric normal. The generated S0 mode has nearly zero displacement along this line, so only the incident and reflected SH0 signals are recorded at the monitored points.

The reflection ratio was calculated according to equation (6.1) for each centre-frequency value; Figure 6.2 (a)-(c) shows it plotted with crack length (expressed in λ_{SH0}) for each of the three crack depths studied. Each plot shows the ratio at the three different frequency-thickness values and also the expected results if the Kirchhoff approximation was valid (obtained simply as 0.25, 0.5 and 0.75 times the results from the through-thickness crack case, reproduced in Figure 6.2 (e) from figure 4.13, Chapter 4).

The observed trend of the reflection ratio, rising almost linearly with crack length initially and then falling, agrees very well with that for through-thickness cracks where it later continues into an oscillatory regime. This trend is consistent with the understanding obtained from earlier studies: diffraction effects are important in the short range, leading to focusing of energy in the backscatter direction. The actual reflection ratio values though, fall short of the Kirchhoff prediction even for 75% deep cracks at low frequency-thickness; but the ratio rises sharply and can be seen to approach it asymptotically as the frequency is increased. For shallow cracks 25% deep, the ratio is well below the approximate estimate even at 400 kHz and there is not much variation from that at 200 kHz. We will discuss this in some more detail with the analysis in Section 6.4.

6.3.1.2 Influence of distance of measurement

The source was fixed at a distance of 32 λ_{SH0} from the crack face, while the reflection was monitored at distances of 3, 4, 5, 10, 15, 20 and 25 λ_{SH0} from it. Results were obtained for two crack lengths, 1 and 5 λ_{SH0}, representing small and large cracks respectively. For each crack length two crack depths 25% and 75% of the plate thickness, representing shallow and deep cracks, were studied, and simulations were performed at a centre-frequency of 400 kHz spanning the low to high-frequency regimes.

The reflection ratio was calculated at this centre-frequency, again using equation (6.1). Figures 6.3 (a) and (b) show the reflection ratio plotted with the distance at which the reflected signal is monitored (expressed in λ_{SH0}) for the two crack length cases and each of the two crack depths studied. Figures 6.3 (c) and (d) reproduce the results for 1 and 5 λ_{SH0} long cracks from through-thickness crack results of Figure 4.16, Chapter 4. We notice that at both crack depths the trend is identical with that for the through-thickness crack case of the same length except for a scale factor associated with the part-through cracks. The reflection ratio rises and falls before stabilizing at farther distances from the crack. For through-thickness cracks, this behaviour could be explained by a simple model assuming the insonified face to behave like a uniform ideal shear transducer. The present study shows that such an explanation holds even for part-thickness cracks and the results differ only in their magnitude by a frequency dependent factor. We will examine why this happens and study the nature of this factor in Section 6.4.

6.3.2 Angular profile of the reflected field

Next we examine the reflection at various angles θ_R for an incidence angle $\theta_I = 0^0$ (the angles are defined counter-clockwise from the crack's symmetric normal). At these diffuse angles the reflected A0 mode will have displacements in all the three directions at the surface of the plate, but its mode shape is such that the in-plane components vanish entirely at the mid-plane. Therefore for this set of studies, the SH0 mode reflection is isolated by monitoring at the mid-plane of the model plate.

The geometrical details on the mid-plane of the model are shown in Figure 6.4. The excitation was located at a distance $D = 32\ \lambda_{SH0}$ (SH0 wavelengths at the centre frequency of the toneburst) away from the crack and such that the principal axis PA of the generated SH0 waves coincides with SN, the symmetric normal to the crack. The incident signal I was monitored at a distance d_I from the source, along PA. Reflected SH0 waves were monitored along one half of a vertical line intersecting SN at a point S and a distance $d_{M0} = 12\ \lambda_{SH0}$ from the crack. Starting from a point along this line at a distance of 12.5 λ_{SH0} from S, nodal displacements R_{U2} in the U2 direction were monitored at intervals of around 1 λ_{SH0} all the way down to S. This yielded monitoring angles in the range $\theta_R = 0^0$ to 45^0 in intervals of 6^0-10^0. The resultant displacement R is related to R_{U2} by $R\cos(\theta_R) = R_{U2}$ so the resultant displacement values were obtained from the U2 values for each monitored point as $R = R_{U2}/\cos(\theta_R))$. The values in the range from -45^0 down to 0^0 were assumed to be identical with these due to the symmetry in the configuration. The reflection ratio was then calculated using equation (6.1) with $d_M = d_{M0}/\cos(\theta_R)$. Cracks of two lengths 1 and 5 λ_{SH0}, and three different depths 25%, 50% and 75% of the plate thickness for each crack length were studied, and simulations were performed at a centre-frequency of 400 kHz.

Figures 6.5 (a)-(c) shows the reflection ratio plotted with the angle at which the reflection is monitored for the two crack length cases and each of three crack depths studied, while 6.5 (d) reproduces that for through-thickness cracks from Figure 5.2, Chapter 5. We again observe excellent agreement of the angular profile of the reflected field with that for the through-thickness crack case for all the three crack depths. The reflected energy is concentrated in a narrow beam around the specular direction and this focusing increases with the length of the crack, just as an ideal transducer would tend to generate a more collimated beam at larger diameters.

6.3.3 Experimental validation of FE modeling

The reflection ratio-crack length study in Section 6.3.1.1 was repeated with the crack replaced by a notch, for the validation studies. 10 mm long, 0.5 mm wide notches at two

depths, 50% and 75% of the plate thickness were created in the FE models, matching the details of the notches cut in the experimental plates. In both simulations and experiments, the same procedure was followed regarding the excitation and monitoring of scattered signals and the frequency sweep. SH0 waves were excited from a distance of 16 λ_{SH0} from the notch face so that a symmetric incidence problem is realized. Nodal displacements in the U2 direction were monitored 5 λ_{SH0} from the notch, along its symmetric normal. As in the crack case, the incident and reflected SH0 signals are expected almost exclusively at the monitored points. Starting from 200 kHz, the operating frequency was swept in steps of 50 kHz up to 400 kHz so that different notch lengths with respect to λ_{SH0} were obtained. The reflection ratio was again calculated using equation (6.1), and Figure 6.6 shows the results obtained at different frequency-thickness (and hence different ℓ/λ_{SH0}) values for the two notch depths, from FE simulations and experiments. We find excellent agreement between the measurements and predictions.

6.4 Analysis

The studies in the previous sections show that the reflection of the SH0 mode from part-thickness cracks is related to that from through-thickness cracks of the same length through a frequency dependent scale factor. This factor as it were, seems to account for the change in the crack depth. Through the following parts of the present section, we seek to systematically understand the physical basis for and conditions underpinning such behaviour. Continuing with the analytical approach of Chapter 4, in the first part 6.4.1, we derive a formula for the beam-compensated reflection ratio for our problem. Consideration of the relationship between the reflection ratio for through- and part-thickness cracks in 6.4.2 using insights from Chapters 4 and 5 reveals the conditions when a scale factor-like behaviour manifests. Finally, 6.4.3 helps understand the nature of the scale factor by arriving at and testing the limits of estimates for it in the different frequency regimes.

6.4.1 Formula for reflection ratio

Following on from the analysis in Chapter 4, the scattered displacement field $u_k^{sc}(\vec{p})$ in the $\hat{e}_k$ direction at a position $\vec{p}$ in the medium due to a crack of length ℓ, depth b and outward normal n_j, is written as a superposition of elemental sources placed on its insonified face s^+ as[68, 69]:

$$u_k^{sc}(\vec{p},\omega) = \int_{s^+} \Delta u_i(\vec{s},\omega)[\Sigma_{ij;k}^0(\vec{p}\,|\,\vec{s},\omega)n_j]\,dS \qquad (6.2)$$

where $\Delta u_i(\vec{s})$ is the displacement jump across the crack faces, $\Sigma_{ij;k}^0(\vec{p}\,|\,\vec{s},\omega)n_j$ is the traction Green's function giving the traction force in the $\hat{e}_k$ direction at a position $\vec{p}$ due to a point force applied in the $\hat{e}_i$ direction at the position $\vec{s}$ in *the free medium in the absence of the crack* and dS is an area element and the integral is on the insonified face s^+ of the crack. As usual, the frequency term $e^{j\omega t}$ is suppressed here and throughout this presentation.

In the following, we will adapt equation (6.2) to our problem. A harmonic point excitation vibrating parallel to the crack face and uniform through the thickness of the thin plate is assumed to be located at a distance D from the crack. We introduce cylindrical coordinates as shown in Figure 6.7, with the origin at the excitation point and the negative 'z' axis pointing into the plate thickness. Thus the excitation consists of a line force vibrating along $\theta = \pi/2$ and uniform through the plate thickness, while the crack is located along the line $r\cos(\theta) = D$ with normals $\hat{n} = \cos(\phi)\hat{e}_r + \sin(\phi)\hat{e}_\theta + z\hat{e}_z$.

Introducing $d\ell = rd\theta$ as a length element and taking $\cos(\phi) \approx 1$, the scattered displacement due to the incident SH0 mode having displacements only in the u_θ direction can then be given as

$$u_k^{sc}(\vec{p},\omega) = \iint_{s^+} \Delta u_\theta(\vec{s},\omega)\Sigma_{r\theta;k}^0(\vec{p}\,|\,\vec{s},\omega)\,d\ell dz \qquad (6.3)$$

At the low frequencies considered, displacements and stresses will be uniform in the 'z' or the depth direction, so we can take $\Sigma_{r\theta;k}^{0}(\vec{p}\,|\,\vec{s},\omega)$ as depth invariant; assuming further that the displacement jump $\Delta u_{\theta}^{sc}(\vec{s},\omega)$ does not vary in the length direction of the crack and changing the order of integration yields

$$u_{k}^{sc}(\vec{p},\omega) = \int_{0}^{b} \Delta u_{\theta}(\vec{s},\omega)dz \int_{\ell} \Sigma_{r\theta;k}^{0}(\vec{p}\,|\,\vec{s},\omega)\,d\ell \qquad (6.4)$$

The reflection ratio according to equation (6.1) for a crack of depth b and length ℓ would then be

$$R(b,\ell) = \frac{u_{\theta}^{sc}(\vec{p},\omega)\sqrt{D+d_{M}}}{u_{\theta}^{inc}(\vec{s},\omega)\sqrt{D}} = \sqrt{\frac{D+d_{M}}{D}}\,\frac{\int_{0}^{b}\Delta u_{\theta}(\vec{s},\omega)dz}{u_{\theta}^{inc}(\vec{s},\omega)}\int_{\ell}\Sigma_{r\theta;k}^{0}(\vec{p}\,|\,\vec{s},\omega)\,d\ell \qquad (6.5)$$

where $u_{\theta}^{inc}(\vec{s},\omega)$ is the incident SH0 displacement on the insonified crack face.

6.4.2 Formula for the scale factor

If the Kirchhoff approximation in the depth direction is valid, then $\Delta u_{\theta}(\vec{s},\omega) = u_{\theta}(\vec{s}\in s^{+},\omega) = 2u_{\theta}^{inc}(\vec{s},\omega)$ so that the first integral in equation (6.5) is easily evaluated: $\int_{0}^{b}\Delta u_{\theta}(\vec{s},\omega)dz = 2u_{\theta}^{inc}(\vec{s},\omega)b$. The reflection ratio would simply be

$$R(b,\ell) = \sqrt{\frac{D+d_{M}}{D}}\,2b\int_{\ell}\Sigma_{r\theta;k}^{0}(\vec{p}\,|\,\vec{s},\omega)\,d\ell \qquad (6.6)$$

As observed earlier this approximation holds for through-thickness cracks which are not too small (i.e. of length ℓ such that $k_{SH0}\ell > 1$) and we can take the reflection ratio $R(b,\ell)$ for this case to be given by equation (6.6) with reasonable accuracy.

Thus for part-thickness cracks which can exhibit a Kirchhoff-like behaviour, the reflection ratio for a crack at a given depth b and length ℓ can be obtained from the value for a through-thickness crack of the same length simply as

$$R(b,\ell) = \alpha . R(h,\ell)\text{, with } \alpha = \frac{b}{h} \qquad (6.7)$$

where 'h' is the thickness of the thin plate.

In general though, the reflection ratio for a part-thickness crack would be related to that for the through-thickness case as

$$R(b,\ell) = k(\alpha,\omega)R(h,\ell) \qquad (6.8a)$$

$$\text{where } k(\alpha,\omega) = \frac{\int_0^b \Delta u_\theta^{sc}(\vec{s},\omega)dz}{(2h)u_\theta^i(\vec{s},\omega)} \qquad (6.8b)$$

Engineering intuition would tell us that we should be able to obtain the reflection from a part-thickness crack by knowing that from a through-crack of the same length and accounting for the difference in the crack depth. But such thinking implicitly assumes that the effects of the length and the depth of the crack on the scattering process are uncoupled. The assumptions made in arriving at 6.8 uncover the conditions in which this uncoupling can happen: the frequency must be low enough such that the stresses are constant through the plate thickness, and the crack must be small compared to the incident wavefront, so that the COD is constant along the crack length. Equation 6.8b reveals that the frequency dependence of the scale factor $k(\alpha,\omega)$ comes about from that of the amplitude of the incident wave and how the crack opens in response. Also we see that the difference in the reflection from part- and through-thickness cracks is due to the difference in the way they respond to the incident wave.

6.4.3 Estimates

Specific knowledge of how the crack opens is necessary to evaluate the factor $k(\alpha,\omega)$ by which the part- and through-thickness crack cases are related. However, here

approximate estimates for the different scattering regimes are suggested. For the high-frequency regime we can deduce from equation (6.7) that $k(\alpha, \omega) = \alpha$. From past studies on the scattering of fundamental guided waves by long cracks [27, 28], at low frequencies $\Delta u_\theta^{sc}(s, \omega)$ would appear to be of the order of $(b/h)^2$ or α^2: therefore, we can take $k(\alpha, \omega) \approx \alpha^3$. This seems valid for the low-frequency scattering of SH0 waves by long cracks, reproduced from the paper by Demma *et al* [29] in Figure 3.17, Chapter 3. Finally, through an examination of the results presented in Section 6.3, a suggested empirical first-estimate for medium frequencies is $k(\alpha, \omega) \approx \alpha^2$.

We will next examine the limits of these estimates with the help of the results from section 6.3.1.1. Table 6.1 classifies cracks of different depths h considered in that study into the low, medium or high frequency regimes based on whether the product $k_{SH0}h$ is less than, approximately equal to or greater than unity. . This helps identify the estimates for $k(\alpha, \omega)$ in the frequency regime appropriate for each crack depth. Equation (8a) is then invoked and the reflection ratio for the different part-thickness cracks is calculated from results for through-thickness cracks of the same length from Chapter 4. The estimated values of the reflection ratio so obtained are compared with the actual FE results of Section 6.3.1.1 in Figure 6.8 (a)-(c) for different crack depths and frequency-thickness values, while Figure 6.8 (d) shows the same comparison but with the reflection ratio plotted with the crack depth instead of length, for the case of a 3 λ_{SH0} long crack. We find very good agreement for the 75 % crack depth case where the three frequencies studied nearly fall into the three different scattering regimes, whereas for the other two crack depths, the estimates are not that accurate. For the 25% deep crack, Table 6.1 would suggest that all the 3 frequencies studied lie within the low-frequency regime, but the actual FE results lie somewhere between the low- and medium-frequency estimates. For the 50% deep crack, even though the full FE results lie around the low- to medium-frequency regimes, the estimates cannot distinguish between 300 and 400 kHz. Arguably the low-frequency estimates suggested here are very rough, but the results show that often we can obtain a fair hint of the order of the reflection amplitude. With better

approximations for $k(\alpha, \omega)$ and knowledge of the crack length and the frequency used, this approach can provide an alternative prognosis for the crack depth.

6.5 Discussion and conclusions

This chapter studied the interaction of low frequency SH0 waves with part-thickness cracks for the symmetric incidence problem. The interaction was studied in terms of the influence on the specular reflection, of the crack length and the spatial and angular measurement positions at different crack depths and operating frequencies. The FE modeling was validated by comparison with experiments for the case of scattering by a finite part-depth rectangular notch. The results from all the studies are similar to those obtained for the corresponding through-thickness case with the trend being identical and actual values differing only by a frequency dependent scale factor. Theoretical analysis is used to reveal the physical basis for such behaviour and helps obtain estimates for the scale factor, exactly derived for the high-frequency scattering regime, and empirical for the medium and low-frequency regimes.

From the perspective of guided wave imaging, the finding that the effects of the length and depth of cracks on the reflection uncouple provided the incident wavefront is larger than the crack and the stresses are depth-independent, means that the understanding obtained for scattering of the SH0 mode from through-thickness cracks is often sufficient to deal with the part-thickness case as well. Although only the symmetric incidence problem and the reflected field were studied here, the generality of the results helps infer that the reflection at oblique or non-symmetric incidence as well as the diffraction from part-cracks would be related to that for the through-thickness case through an appropriate factor. Estimates of the scaling and thus of the scattered amplitudes at different scattering regimes will help when studying the influence of the crack dimensions on the image intensity. Finally, the influence of the width of a finite notch on the scattering as highlighted here again brings up the importance of the difference between notches and cracks and the frequency-related limit when they would be equivalent.
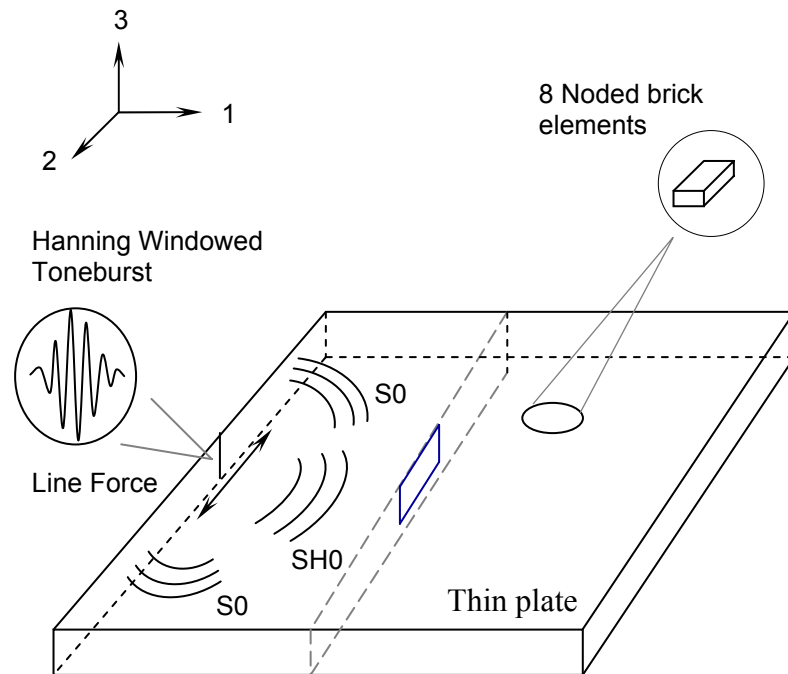
Figure 6.1 Details of the configuration studied in this Chapter and those for the FE simulations.
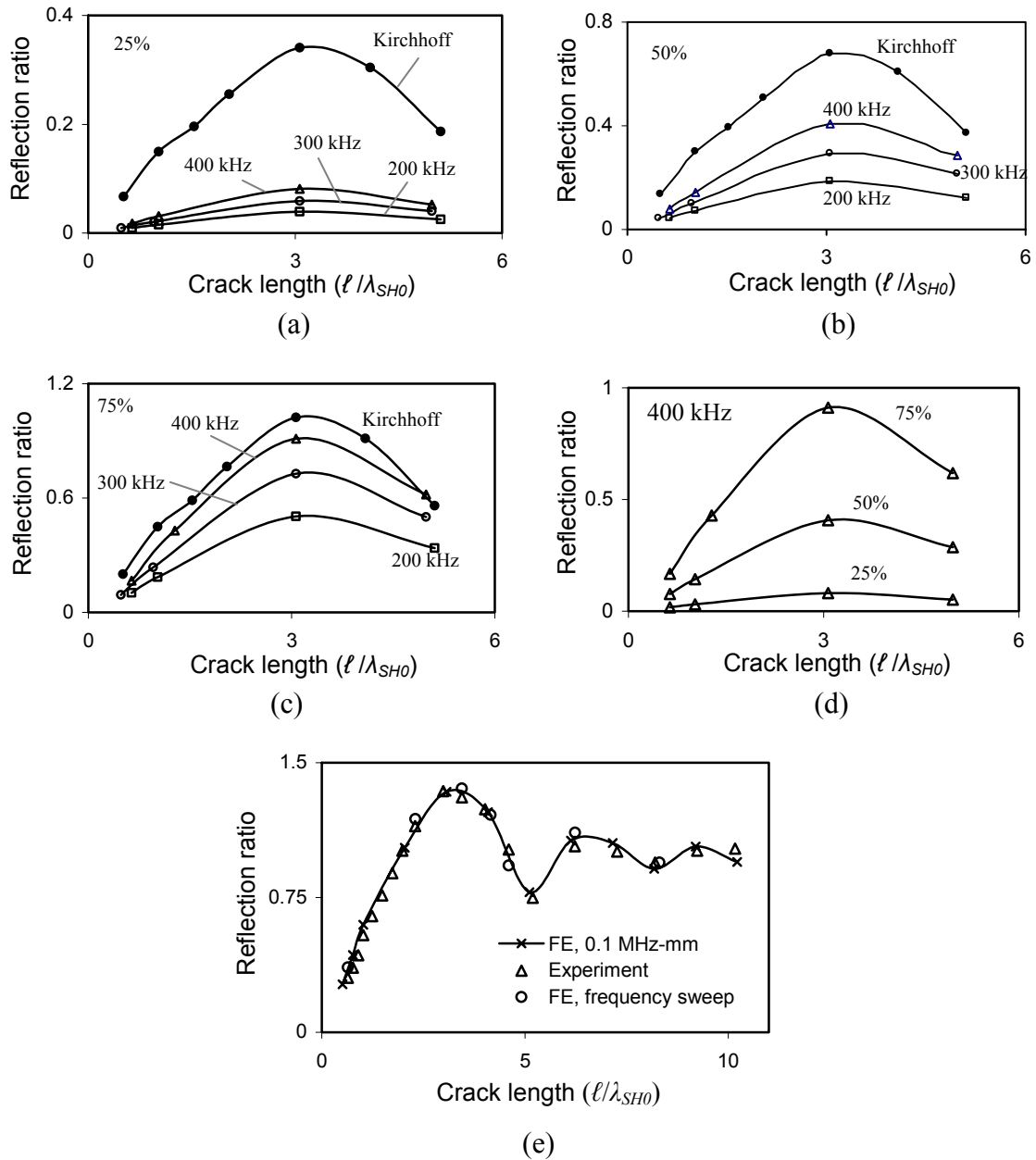
Figure 6.2 (a)-(c) Reflection ratio plotted with crack length (expressed in λ_{SH0}) for 25%, 50% and 75% deep cracks respectively. Each plot shows results at different incident frequencies; the lines with filled circles indicate estimates using Kirchhoff approximation; (d) shows the results for all 3 crack depths for just the 400 kHz case; (e) reproduces Figure 4.13 from Chapter 4.
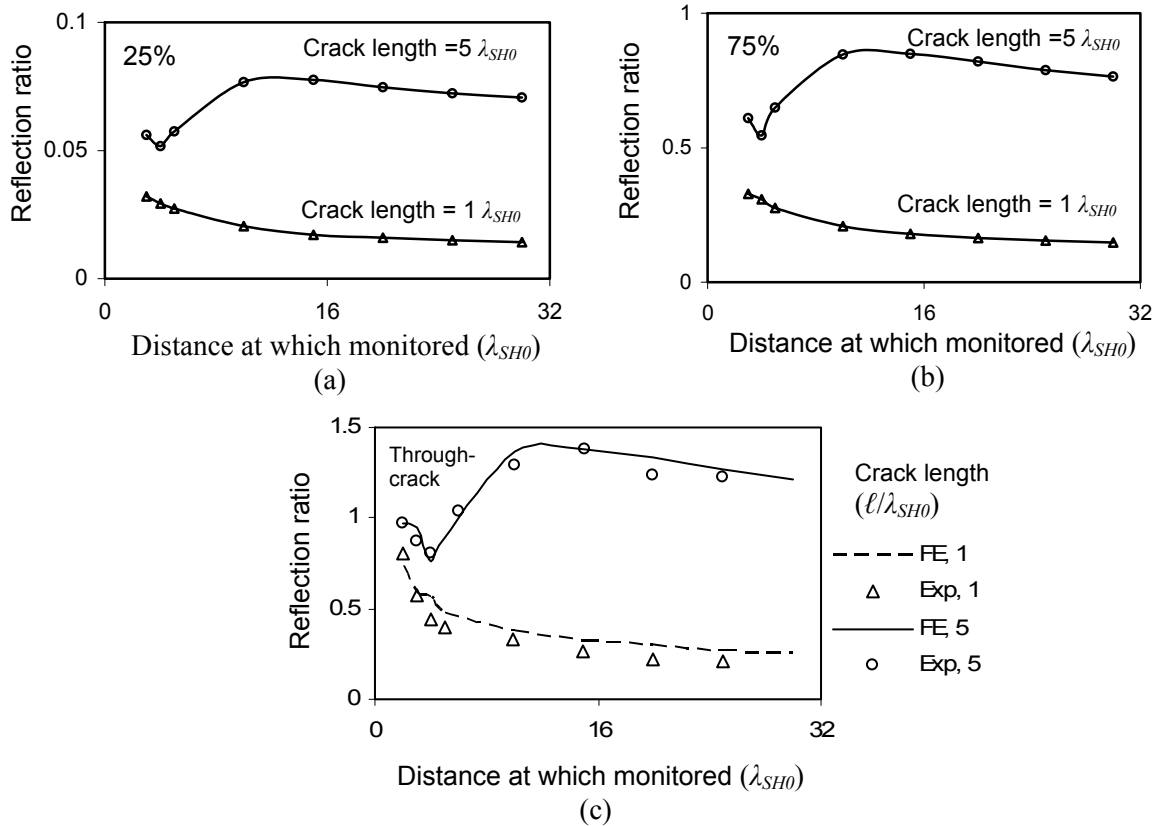
Figure 6.3 Reflection ratio plotted with the distance at which the reflected signal is monitored (expressed in λ_{SH0}) for two crack lengths 1 λ_{SH0} and 5 λ_{SH0}; (a) and (b): results for two crack depths, 25% and 75% of the plate thickness; (c): results for through-thickness crack cases of the same lengths, reproduced from Figure 4.16 (c), Chapter 4.
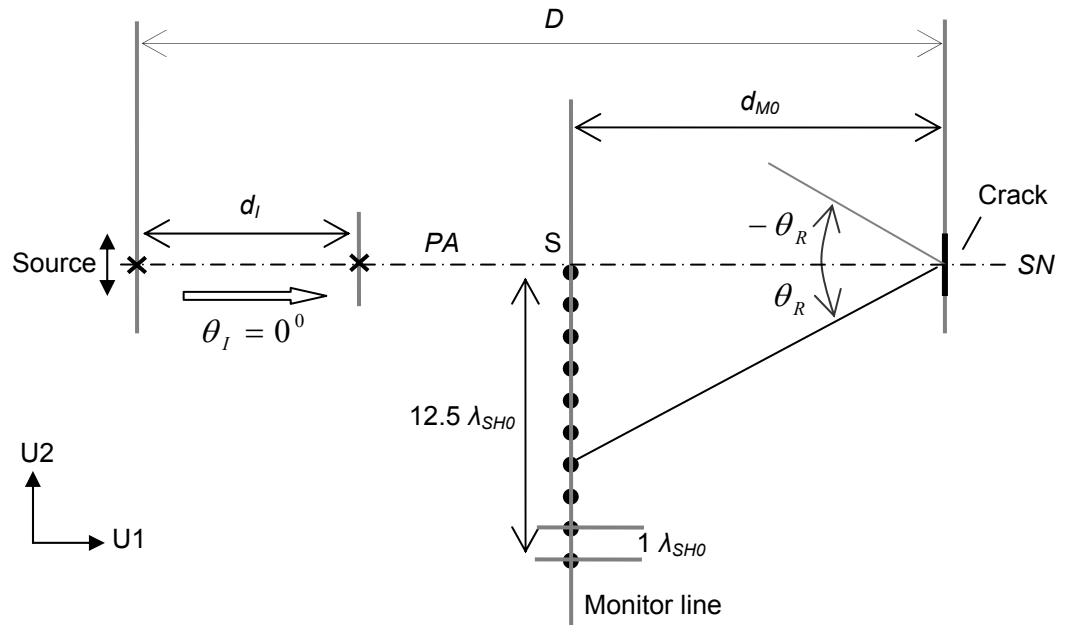
Figure 6.4 Geometry for the study of reflection at angles θ_R for an incidence angle $\theta_I = 0^0$ (defined with respect to the crack's symmetric normal).
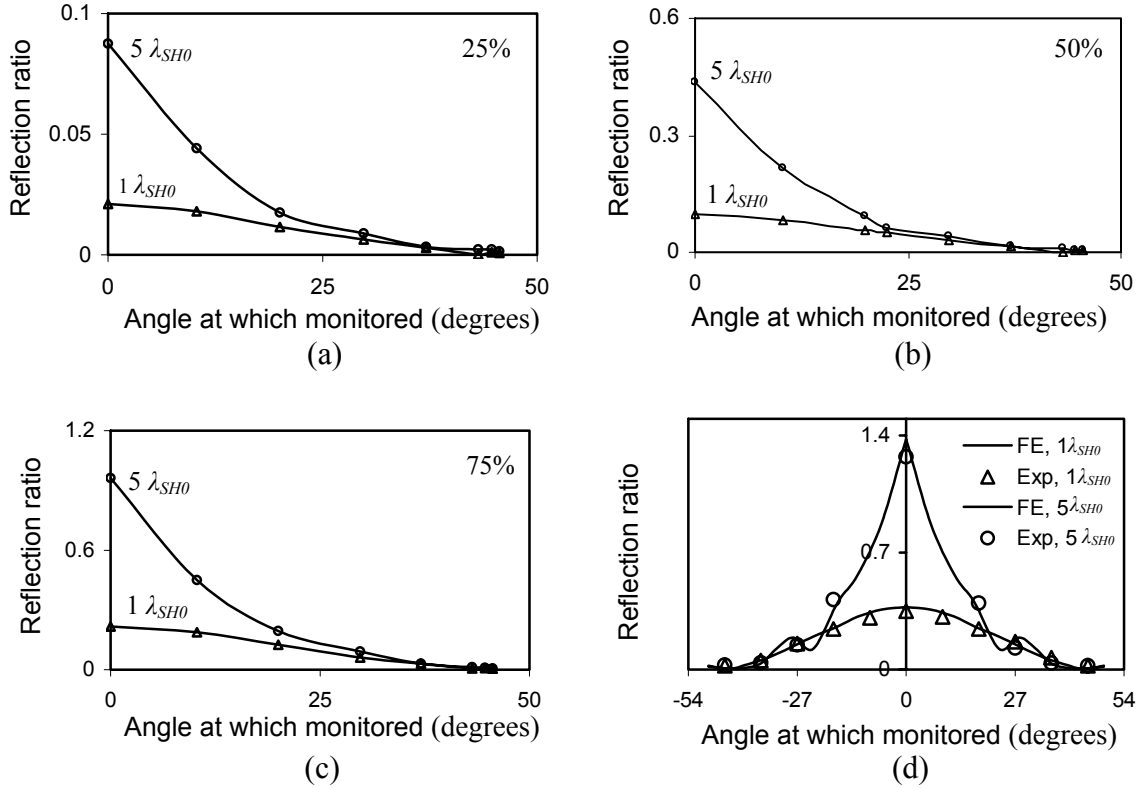
Figure 6.5 Reflection ratio plotted with $90^0 - \theta_R$: results are shown for two crack lengths 1 λ_{SH0} and 5 λ_{SH0} studied for each of three crack depths cases (a) 25%, (b) 50% and (c) 75% of the plate thickness; (d) through-crack results for cracks of the same lengths from Figure 5.2, Chapter 5.

(a)   (b)
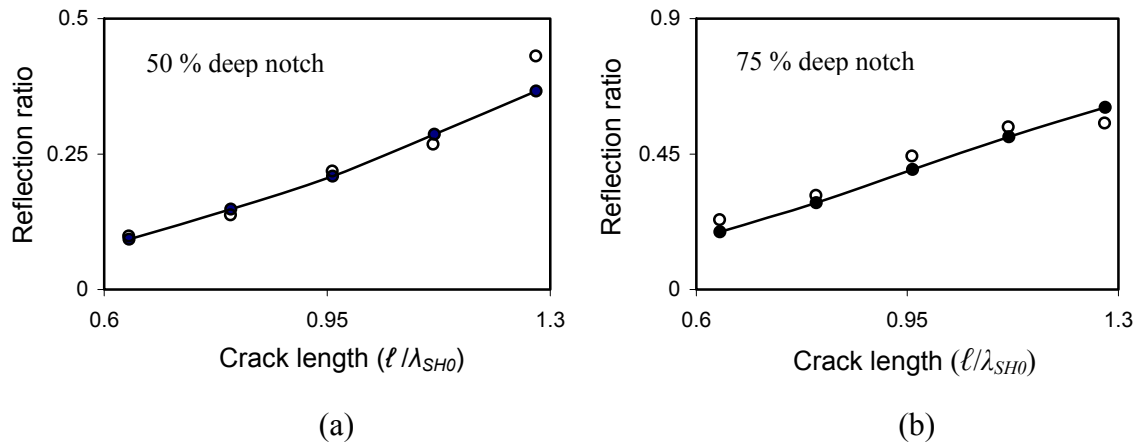
Figure 6.6 Reflection results from FE simulations (filled circles) and experiments (empty circles) obtained using a frequency sweep (and hence different ℓ/λ_{SH0}) for two notch depth cases (a) 50% and (b) 75% of the plate thickness.
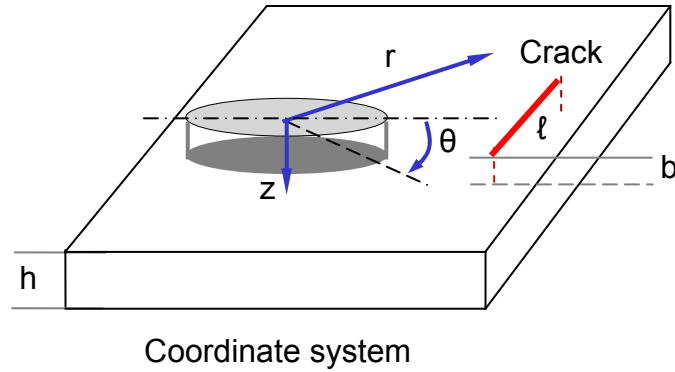
Coordinate system

Figure 6.7 Cylindrical coordinates with origin at the excitation point and the negative 'z' axis pointing into the plate thickness: a line force vibrating along $\theta = \pi / 2$ and uniform through the plate thickness provides the excitation and the crack is located along the line $r\cos(\theta) = D$ with normals $\hat{n} = \cos(\phi)\hat{e}_r + \sin(\phi)\hat{e}_\theta + z\hat{e}_z$.

Crack Depth → ↓ Frequency	25% 0.5 mm	50% 1 mm	75% 1.5 mm
200 kHz $k_{SH0} \approx 0.4$ mm^{-1}	**L**	**L**	**L**
300 kHz $k_{SH0} \approx 0.6$ mm^{-1}	**L**	**L / M**	**M**
400 kHz $k_{SH0} \approx 0.8$ mm^{-1}	L	**M**	**M / H**

Table 6.1 Cracks of different depths h studied in 6.3.1 are classified into the low (L), medium (M) or high (H) frequency regimes based on whether the product $k_{SH0}h$ is less than, approximately equal to or greater than unity.
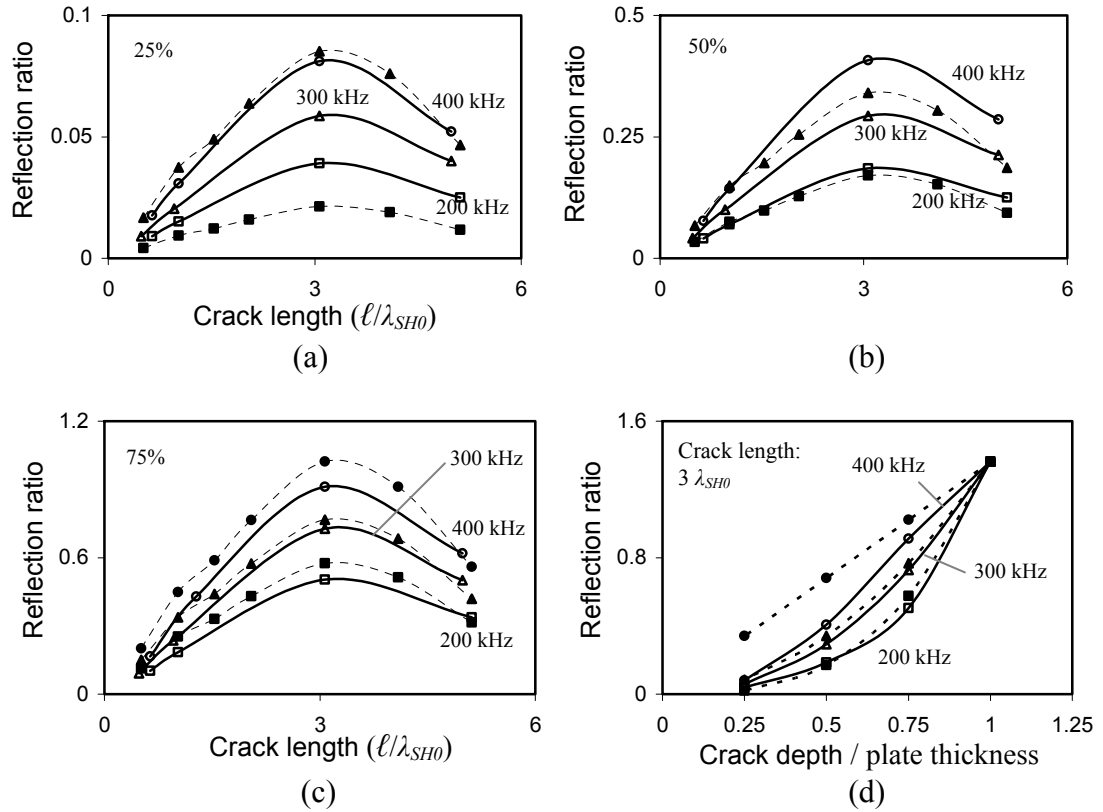
Figure 6.8 Estimated values of reflection ratio obtained using the approach in Section 6.4 compared with the actual FE results of Section 6.3.1 for different incident frequencies at each of the crack depths, (a) 25%, (b) 50% and (c) 75% of the plate thickness: the filled square, triangle and circle denote estimates at the low, medium and high frequency regimes respectively. (d) Shows the same information but the reflection ratio is plotted with the crack depth instead of length, for the case of a 3 λ_{SH0} long crack.

Chapter 7

Conclusions

7.1 Thesis review

This thesis studied the interaction of guided waves with finite planar cracks in free unloaded pipes and plates in the context of higher resolution guided wave inspection.

Chapter 1 discussed basic concepts in guided wave inspection and the limitations on the resolution achievable by current methods. The high-frequency multimodal method and low-frequency array imaging were then introduced as two possible approaches for improving the resolution of guided wave inspection.

Chapter 2 reviewed the basics of the theory of guided elastic wave scattering in order to identify methods which can be used to illuminate the physics behind the results obtained through the rest of the thesis. First the link between bulk and guided elastic wave scattering was pointed out, and this helped see how techniques in treating the latter originate in and developed from the former. Several among the more important methods in bulk wave scattering were introduced, and those which have also been extended to the guided wave case were highlighted. The possibilities for using some methods which have not yet been extended to the treatment of guided wave scattering were discussed.

Chapter 3 considered a simple implementation of the high-frequency multimodal approach in which only one fundamental mode is used in the interrogating signal, and the multi-mode scattered packet is assumed to permit separation into different component modes. Both flat plates and annular cylinders (pipes) were studied. The fundamental antisymmetric Lamb A0 mode was used as the input in plates with long rectangular cracks and the fundamental torsional mode T(0,1) was used in pipes with full-circumference but part-depth planar cracks. The results obtained were analysed for the sensitivity of the reflection of individual modes to the crack depth and that of mode-conversion patterns to different crack depth regimes.

In the light of encouraging results from parallel work at the NDT Group [43, 44, 155] using low-frequency array methods, Chapters 4-6 focussed on the interaction of cylindrical crested low-frequency SH0 waves with finite cracks in thin plates. Since guided SH waves in thin plates correspond to torsional modes in pipes, the results obtained helped clarify the physics of scattering so that imaging methods may be better formulated and developed.

Chapter 4 first set the background by introducing sample results from array imaging methods and presented the motivation for using cylindrical crested SH0 waves. The simple case of symmetric incidence where a line from the wave-source bisects the crack face normally was then considered. Both specular reflection from the crack face and the diffraction from its edges were studied and implications for guided wave inspection were presented.

Chapter 5 continued with through-thickness cracks but the results from the symmetric incidence studies in Chapter 4 were used to understand the more difficult case of arbitrary incidence. Insights from both these chapters were then combined to draw a general picture of the scattering of SH0 waves from through-thickness cracks.

In chapter 6, the understanding obtained about the scattering of SH0 waves by through-thickness cracks was used to investigate that by part-thickness cracks. Only the

symmetric incidence case and the behaviour of the reflected field were studied, but the generality of the parameters considered and the results obtained helped draw conclusions for scattering in general. The relationship between the through- and part-thickness crack problems was also studied and important conclusions bearing upon guided wave inspection were obtained.

7.2 Summary of findings

7.2.1 The two approaches to higher resolution

Working with current inspection frequencies but finding the solution to the resolution problem by means such as array imaging, and working at higher frequencies are the two possible approaches to improved resolution highlighted in Chapter 1. The high frequency approach is the immediate intuitive solution since shorter wavelengths can be achieved allowing better sensitivity to defect dimensions; but this approach also calls for dealing with multiple dispersive modes with complex mode shapes and may require development of new methods of transduction and post-processing of data. On the other hand, although it suffers from inherent low sensitivity, the low-frequency approach has the advantage of simple and often nondispersive modes; current transduction methods are sufficient and array imaging techniques from bulk or scalar wave literature are immediately applicable. These are the costs against which any improvement in resolution achievable by these methods can be assessed relative to one another.

7.2.2 Theoretical methods for understanding the physics of scattering

A general outlook taken at the Imperial College NDT group towards theoretical methods is that even if they do not yield the full solution to the scattering problem, they can often give useful insights into the underlying physics. Chapter 2 first highlighted the well-known essential unity of methods dealing with scattering of both bulk and guided elastic waves. Of these, the integral equation formulation is simple to grasp since it gives a direct mathematical representation of the physical mechanism of scattering of waves as

envisaged by Huygens's principle. An important route to this formulation is through the elastodynamic reciprocity theorem which yields integral formulas for scattering. This formulation also provides a convenient starting point for a number of approximate analytical methods: the Born, quasi-static and extended quasi-static approximations at low frequencies and the Geometric Theory of Diffraction (GTD), Kirchhoff and uniform COD approximations at high frequencies are widely used. Though the Kirchhoff approximation is among the simplest, it is quite accurate at high frequencies and near-specular directions and can form the basis for an elegant analytical treatment of the scattering of guided waves. Examples of such treatment can be found in Chapters 3, 4 and 6 of this thesis- as expected, with plane waves and at high frequencies the method is quite accurate and even at low frequencies and when multiple-diffraction is important, it can provide a very good first estimate. The predictions can be improved using better estimates for the total field induced by the incident wave on an obstacle.

7.2.3 High-frequency multimodal approach

The studies with long cracks in plates and pipes reveal that a simple approach of using a single interrogating mode can prove beneficial in practice. From the perspective of sensitivity to smaller defects, the reflection behaviour due to both A0 and T(0,1) mode incidence is beneficial, although for the A0 mode the frequency must be carefully chosen. Among the different reflected modes, some modes appear to be more sensitive to defect dimensions than others and these can be chosen as the reference 'best modes'.

The extent to which the reflections of other modes differ from those of the best modes provides a powerful method of distinguishing different regimes of the defect dimensions. We have thus suggested that the scatter between the amplitudes of different reflected modes can be used as a parameter to quantify mode conversion for this purpose. With the T(0,1) mode, mode conversion effects at higher frequencies clearly lead to better discrimination between shallow and deep cracks, but this is not always the case with the A0 mode which requires us to choose appropriate operating frequencies.

Information about regions of little or no mode-conversion provides an alternative method of distinguishing different defect dimension regimes. With torsional modes below the T(0,4) cut-off frequency, this can be a straightforward way to distinguish middle-sized cracks where all three modes are present, from shallow and very deep ones where T(0,2) and T(0,3) modes tend to vanish. Similarly when the A0 mode is incident between 2 - 2.5 MHz-mm, the reflected S0 mode vanishes at very shallow and very deep cracks and this can be used to separate the different crack depth regimes in a plate.

7.2.4 Scattering of low frequency cylindrical-crested SH0 waves by cracks

7.2.4.1 Through-thickness cracks

At low frequencies, short range scattering of the SH0 mode is strongly affected by diffraction phenomena which leads to focusing of energy by the crack in the backscattered direction. The diffracted field consists of components arising from primary diffraction from the crack tips (or edges) and multiple reverberations of Rayleigh-like waves traveling along the crack length. A simple diffraction model assuming uniform shear sources on the insonified face can yield very good results for cracks as long as seven times the wavelength considered. From the guided wave imaging perspective, these results provide a simple estimate for the far-field values for a given operating frequency-thickness and crack length. The strong presence of diffraction means that more information may be received by a transducer array than would be contributed by specular reflection alone. Further, there would be a pronounced difference between the scattering from small and very large cracks- for small cracks, it would be difficult to separate specular reflection from edge diffraction.

The angular behaviour of reflection of the SH0 mode from planar cracks is such that it is strongest in the specular direction. Further, the specular reflection itself is strongest at symmetric incidence, but falls rapidly to vanish around the first critical angle of bulk SV waves and then rises to a nearly constant but low value. Because of the equivalence of the physics of the scattering of SH0 waves with that of bulk SV waves, this behaviour is very

similar to that of reflection of bulk SV waves from straight edges. This also means that the amplitudes of the SH0 wave primary diffraction can be estimated from known solutions to canonical bulk SV wave diffraction problems. For long cracks, asymptotic solutions in bulk wave literature can be used to estimate even the secondary diffraction.

Studies with torsional modes which are being currently investigated in array imaging methods for pipes suggest that they can be decomposed into SH0-like waves travelling in helical paths along the pipe length, with each mode corresponding to a different starting angle [155, 184]. This is shown in Figure 7.1. The highly specular and directional nature of SH0 wave reflection from flat cracks, with only little energy reflected at angles above 45^0 means that only the first few torsional modes will be generated by the reflection process. Thus the nature of flat cracks inherently prevents us from fully exploiting the advantages offered by imaging methods which rely on making use of information from all reflected modes. This imposes a limitation on the extent to which the resolution of inspection can be improved by low-frequency methods.

7.2.4.2 Part-thickness cracks

The trend of the scattering from part-thickness cracks results is identical to that from through-thickness cracks of the same length and the actual values differ only by a frequency dependent scale factor. SH0 mode scattering from part-cracks can thus be thought of as an appropriately scaled field of an ideal shear transducer placed on the crack's insonified face. Theoretical analysis reveals that the physical basis for such behaviour comes from the uncoupling of the effects of the length and depth of cracks at low frequencies and when cracks are small compared to the radius of the incident wavefront. It is possible to arrive at estimates for these scale factors, exactly derived for the high-frequency scattering regime, and empirical for the medium and low-frequency regimes.

From the perspective of guided wave imaging this kind of uncoupling means that the understanding obtained for scattering of the SH0 mode from through-thickness cracks is

sufficient to deal with the part-thickness case as well. This is significant because the through-thickness case can often be modeled in simple two-dimensional domains and the results are related to bulk SV wave problems. Moreover, with knowledge or an idea of the appropriate frequency regime, a measured reflection value and an estimate of the crack length, we can immediately work out an estimate of the crack depth with the help of the scale factors.

The part-thickness crack studies also highlighted again, the difference between scattering from notches and cracks and the frequency-related limit when they would be equivalent. Often the reflection from notch-like defects with a finite width would be much stronger than that from a crack of corresponding length.

7.3 Future work

7.3.1 High frequencies

The suggested next step at higher frequencies is to understand the reflection behaviour with smaller, fully three-dimensional cracks. Unlike the low-frequency SH0 studies, the effects of the length and the depth of the cracks on the scattering will not fully uncouple at higher frequencies: this is because at such frequencies the stress mode shapes will be depth-dependent and a reduction such as that between equations (6.3) to (6.4) cannot be achieved. But the effect of finiteness of the crack can be expected to be similar to that at low frequencies- it would induce a directivity pattern into the reflection behaviour. Whether the reflection amplitudes of different modes individually and relative to each other retain a high degree of sensitivity to defect dimensions as with long cracks in such a situation, needs to be seen.

Moreover in practice, the effects of dispersion and that of similar velocities for multiple modes could mean that the different modes cannot be separated and a 2D FFT may not be feasible Strategies for extracting different component modes from such mixed signals need to be studied and doing so using appropriate transduction could be an important area.

The work on high-frequency guided waves in this thesis has assumed incident plane waves: in practice often finite sources are employed and therefore the reflection behaviour due to such sources is a further area to be investigated. The general approach adopted in understanding low-frequency SH0 wave scattering can be followed to reduce the number of parameters in such studies.

7.3.2 Low frequencies

The next steps towards aiding the development of the low frequency array imaging methods would be to understand the scattering of circular-crested SH0 waves by defects approaching other geometries of practical interest such as corrosion patches. Finite rectangular holes and notch-like part-thickness defects such as those shown in Figure 7.2 could be a first starting point for such studies. Although the overall behaviour is likely to be similar to that predicted for reflection of the plane SH0 waves from a notch [19], the low frequencies of interest and cylindrical incident waves mean that diffraction from the sides of the notch could have an important influence on the scattered field. Surface waves are likely to be generated on the base of the notch and will reverberate along its length.

Studying the scattering from circular part- and through-thickness holes represented in Figure 7.3 would be the logical next step. From what we already know about the scattering of SH0 waves from straight edges and cracks, the behaviour from such circular defects can be predicted. When the hole is very small compared to the incident wavelength, it will tend towards a point scatterer in a solid. But when the hole diameter is comparable to or greater than the incident wavelength, interesting results can be expected: at any angle of incidence, a line joining the wave source to the centre of the hole will be a normal to the hole and along this direction, there will be a strong reflection. Thus a peak reflection would be obtained in the backscatter direction along this line, for any source position. This in general, is likely to set a limit on improving the resolution limits with low-frequency array imaging methods.
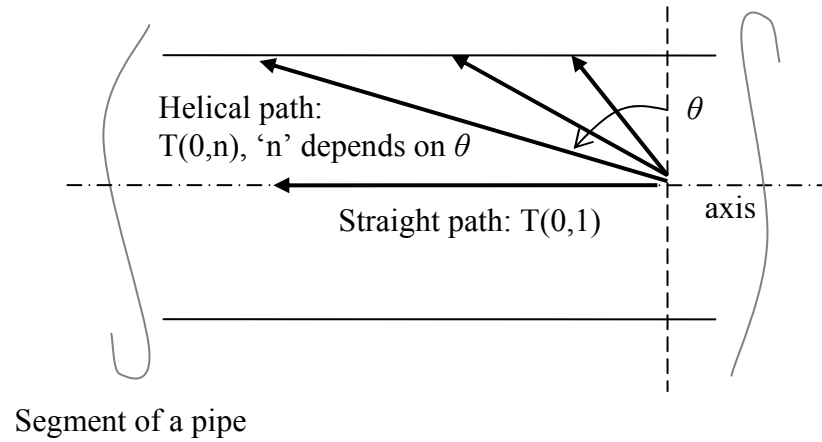
Figure 7.1 Torsional modes can be decomposed into SH0-like waves travelling in helical paths along the pipe length, with each mode corresponding to different starting angles [155, 184].
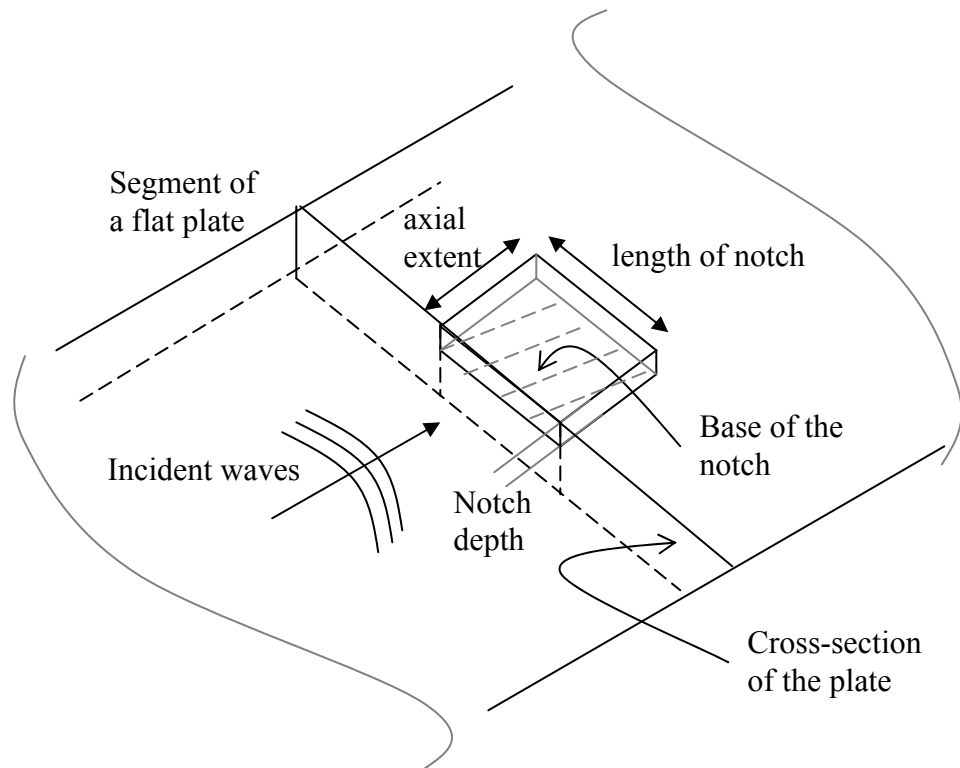
Figure 7.2 Rectangular holes and notch-like part-thickness defects in flat plates.
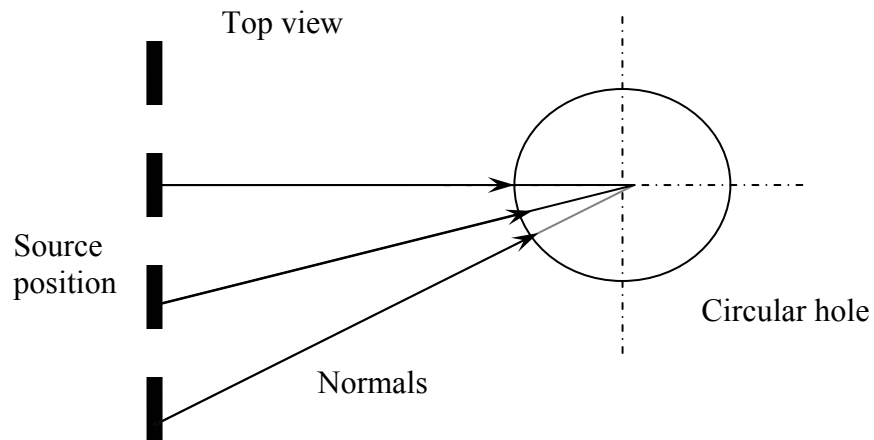
Figure 7.3 Scattering from circular part- and through-thickness holes: top view. Any line from the wave-source to the centre of the hole would represent a normal along which there would be a strong backscattered reflection.

References

1.	Alleyne, D., *et al.*, *Rapid long range inspection of chemical plant pipework using guided wave.* Insight, 2001. **43**(2): p. 93 - 96.

2.	Wilcox, P., *et al.*, *Guided wave testing of rail.* Insight, 2003. **45**: p. 413-420.

3.	Wilcox, P., M. Lowe, and P. Cawley, *An EMAT array for the rapid inspection of large structures using guided waves*, in *Review of Progress in Quantitative NDE*. Vol. 22. 2003, American Institute of Physics: Melville, New York. p. 814-821.

4.	Wilcox, P., *Omni-directional guided wave transducer arrays for the rapid inspection of large areas of plate structures.* IEEE Transactions on Ultrasonics, Ferroelectrics and Frequency control, 2003. **50**(6): p. 699 - 709.

5.	Fromme, P., P. Wilcox, and P. Cawley, *Remote monitoring of plate-like structures using guided wave arrays*, in *Review of Progress in Quantitative NDE*, D.O. Thompson and D.E. Chimenti, Editors. Vol. 22. 2003, American Institute of Physics: Melville, New York. p. 157 - 164.

6.	Fromme, P., *et al.*, *On the development and testing of a guided ultrasonic wave array for structural integrity monitoring.* Ultrasonics, Ferroelectrics and Frequency Control, IEEE Transactions on, 2006. **53**(4): p. 777-785.

7.	Silk, M.G., *The use of diffraction-based time-of-flight measurements to locate and size defects.* British Journal of Nondestructive Testing, 1984. **26**: p. 208-213.

8.	Silk, M.G., *Defect sizing using ultrasonic diffraction.* British Journal of Nondestructive Testing, 1979. **21**: p. 12-55.

9.	Charlesworth, J.P. and J.A.G. Temple, *Engineering Applications of Ultrasonic Time of Flight Diffraction*. 2 ed. 2001, Philadelphia, PA: Research Studies Press Ltd.

10.	Alleyne, D.N. and P. Cawley, *Optimization of Lamb wave inspection techniques.* NDT & E International, 1992. **25**: p. 11-22.

11.	Cawley, P. and D. Alleyne, *The use of Lamb waves for the long range inspection of large structures.* Ultrasonics, 1996. **34**: p. 287-290.

12.	Lowe, M.J.S., D.N. Alleyne, and P. Cawley, *Defect Detection in Pipes using Guided Waves.* Ultrasonics, 1998. **36**: p. 147 - 154.

13.   Cawley, P., *et al.*, *Practical long range guided wave testing: Applications to pipes and rail.* Materials Evaluation, 2003(January): p. 66-74.

14.   Alleyne, D.N. and P. Cawley, *The effect of discontinuities on the long range propagation of Lamb waves in pipes.* Proceedings of the Institution of Mechanical Engineers, 1996. **210**: p. 217-226.

15.   Wilcox, P., M. Lowe, and P. Cawley, *The effect of dispersion on long-range inspection using ultrasonic guided waves.* NDT&E international, 2001. **34**: p. 1 - 9.

16.   Wilcox, P., M. Lowe, and P. Cawley, *Mode and transducer selection for long range lamb wave inspection.* Journal of intelligent Material systems and structures, 2001. **12**(August): p. 553-565.

17.   Mudge, P., *Field application of the Teletest long range ultrasonic testing technique.* Insight, 2001. **43**: p. 74-77.

18.   Rose, J.L., *et al.*, *Guided Wave Flexural Mode Tuning and Focusing for Pipe Testing.* Materials Evaluation, 2003(February): p. 162 - 167.

19.   Demma, A., P. Cawley, and M. Lowe, *Scattering of the fundamental shear horizontal mode from steps and notches in plates.* Journal of the Acoustical Society of America, 2003. **113**(4): p. 1880 - 1891.

20.   Demma, A., *et al.*, *The reflection of guided waves from notches in pipes: a guide for interpreting corrosion measurements.* NDT&E International, 2004. **37**: p. 167-180.

21.   Demma, A.C., P. Lowe, M. J. S., *Mode conversion of longitudinal and torsional guided modes due to pipe bends*, in *Review of Progress in Quantitative NDE*, D.O. Thompson and D.E. Chimenti, Editors. Vol. 20. 2001, American Institute of Physics: Melville, New York. p. 172-179.

22.   Diligent, O., *et al.*, *Prediction and measurement of nonpropagating Lamb modes at the free end of a plate when the fundamental antisymmetric mode A_0 is incident.* Journal of the Acoustical Society of America, 2003. **113**(6): p. 3032 - 3042.

23.   Lowe, M.J.S. and O. Diligent, *Reflection of the fundamental lamb modes from the ends of plates*, in *Review of Progress in Quantitative NDE*, D.O. Thompson and

D.E. Chimenti, Editors. Vol. 20. 2001, American Institute of Physics: Melville, New York. p. 89-96.

24. Fong, J. and M. Lowe, *Curvature effect on the properties of guided waves in plates.* Review of Progress in Quantitative NDE, 2004. **23**: p. 126-133.

25. Diligent, O., and Lowe, M.J.S., *Reflection of the s_0 Lamb mode from a flat bottom circular hole.* Journal of the Acoustical Society of America, 2005. **118**(5): p. 2869-2879.

26. Diligent, O., *et al.*, *The low-frequency reflection and scattering of the s_0 Lamb mode from a circular through-thickness hole in a plate: finite element, analytical and experimental studies.* Journal of the Acoustical Society of America, 2002. **112**(6): p. 2589 - 2601.

27. Lowe, M.J.S., *et al.*, *The low-frequency reflection characteristics of the fundamental anti-symmetric Lamb wave a_0 from a rectangular notch in a plate.* Journal of the Acoustical Society of America, 2002. **112**(6): p. 2612-2622.

28. Lowe, M.J.S., and Diligent, O., *Low -frequency reflection characteristics of the s_0 Lamb wave from a rectangular notch in a plate.* Journal of the Acoustical Society of America, 2002. **111**(1): p. 64-74.

29. Demma, A., *et al.*, *The reflection of the fundamental torsional mode from cracks and notches in pipes.* Journal of the Acoustical Society of America, 2003. **114**(2): p. 611-625.

30. Cawley, P., *et al.*, *The variation of the reflection coefficient of extensional guided waves in pipes from defects as a function of defect depth, axial extent, circumferential extent and frequency.* Proceedings of the Institution of Mechanical Engineers, 2002. **216**(C): p. 1131 - 1143.

31. Simonetti, F., *Lamb wave propagation in elastic plates coated with viscoelastic materials.* Journal of the Acoustical Society of America, 2004. **115**(5): p. 2041-2053.

32. Simonetti, F. and P. Cawley, *A guided wave technique for the characterisation of highly attenuative viscoelastic materials.* Journal of the Acoustical Society of America, 2003. **114**(1): p. 158 - 165.

33. Simonetti, F. and P. Cawley, *On the nature of shear horizontal wave propagation in elastic plates coated with viscoelastic materials.* Proceedings of the Royal Society of London. Series A, Mathematical, Physical and Engineering Sciences, 2004. **460**: p. 2197-2221.

34. Ma, J., F. Simonetti, and M.J.S. Lowe, *Sludge and blockage characterization inside pipes using guided ultrasonic waves*, in *Review of Progress in Quantitative NDE*, D.O. Thompson and D.E. Chimenti, Editors. Vol. 25. 2006, American Institute of Physics: Melville, New York. p. 1656-1663.

35. Ma, J., M.J.S. Lowe, and F. Simonetti, *Feasibility study of sludge and blockage detection inside pipes using guided torsional waves.* Measurement Science and Technology, 2007. **18**: p. 2629-2641.

36. Ma, J., M.J.S. Lowe, and F. Simonetti, *Practical Considerations of Sludge and Blockage Detection Inside Pipes Using Guided Ultrasonic Waves,* in *Review of Progress in Quantitative NDE*, D.O. Thompson and D.E. Chimenti, Editors. Vol. 26. 2007, American Institute of Physics: Melville, New York. p. 136-143.

37. Kolsky, H., *Stress waves in solids*. 1963, New York: Dover Publications.

38. Rose, J.L., *Ultrasonic waves in Solid Media*. 1999, Cambridge University Press: Cambridge, U.K.

39. Auld, B.A., *Acoustic fields and waves in solids*. Vols. 1 and 2. 1973, 1990, Florida: Robert E. Krieger Publishing Company.

40. Lowe, M.J.S., D.N. Alleyne, and P. Cawley, *The mode conversion of a guided wave by a part-circumferential notch in a pipe.* Journal of Applied mechanics, 1998. **65**: p. 649 - 656.

41. Lowe, M., D. Alleyne, and P. Cawley, *The mode conversion of a guided wave by a part-circumferential notch in a pipe.* Journal of Applied Mechanics, 1998. **65**: p. 649-656.

42. Alleyne, D.N., M.J.S. Lowe, and P. Cawley, *The reflection of guided waves from circumferential notches in pipes.* Journal of Applied Mechanics, 1998. **65**: p. 635 - 641.

43. Davies, J., *et al.*, *Review of synthetically focused guided wave imaging techniques with application to defect sizing*, in *Review of Progress in Quantitative NDE*, D.O.

Thompson and D.E. Chimenti, Editors. Vol. 25. 2006, American Institute of Physics: Melville, New York. p. 142-149.

44. Fleming, M., *et al.*, *Super resolution imaging: performance studies*, in *Review of Progress in Quantitative NDE*, D.O. Thompson and D.E. Chimenti, Editors. Vol. 25. 2006, American Institute of Physics: Melville, New York. p. 736-743.

45. Pavlakovic, B., *et al.*, *Disperse: A general purpose program for creating dispersion curves*, in *Review of Progress in Quantitative NDE*, D.O. Thompson and D.E. Chimenti, Editors. Vol. 16. 1997, Plenum: New York. p. 185 - 192.

46. Jones, D.S., *Acoustic and Electromagnetic Waves*. 1986, Oxford: Oxford University Press.

47. Morse, P.M. and H. Feshbach, *Methods of Theoretical Physics*. 1953: McGraw-Hill Book Company.

48. Bowman, J.J., T.B.A. Senior, and P.L.E. Uslenghi, eds., *Electromagnetic and acoustic scattering by simple shapes*. 1969, Amsterdam: North-Holland Publishing Company.

49. Graff, K.F., *Wave Motion in Elastic Solids*. 1975, Oxford: Clarendon Press.

50. Achenbach, J.D., *Wave Propagation in Elastic Solids*. 1973, North-Holland Publishing Company: Amsterdam.

51. Harker, A.H., in *Elastic waves in solids. With applications to Nondestructive Testing of Pipelines*. 1988, IOP Publishing Ltd and British Gas plc: Bristol, England and Philadelphia, USA.

52. Hopf, L., *Introduction to the Differential Equations of Physics*. 1949, New York: Dover Publications.

53. Spiegel, M.R., *Theory and problems of Vector Analysis and an introduction to Tensor Analysis*, in *Schaum's outline series*. 1974, McGraw-Hill Book Company: Singapore.

54. Martin, P.A. and G.R. Wickham, *Diffraction of Elastic Waves by a Penny-Shaped Crack: Analytical and Numerical Results.* Proceedings of the Royal Society of London. Series A, Mathematical and Physical Sciences, 1983. **390**: p. 91-129.

55. Pao, Y.H. and C.C. Mow, *Diffraction of Elastic Waves and Dynamic Stress Concentrations*. 1973, New York: Crane Russak.

56.   Guz', A.N., Kubenko, V. D., and Cherevko, M. A., *Diffraction of elastic waves.* International Applied Mechanics, 1978. **14**(8): p. 789 - 798 (Translated from Prikladnaya Mekhanika, Vol. 14, No. 8, pp. 3–15, August, 1978).

57.   Oien, M.A., and Pao, Y.-H., *Scattering of compressional waves on a rigid spheroidal inclusion.* Transactions of the ASME, E. Journal of Applied Mechanics, 1973. **40**: p. 1073.

58.   Datta, S.K., and Sangster, J.D., *Response of a rigid spheroidal inclusion to an incident plane compressional elastic wave.* SIAM Journal of Applied Mathematics, 1974. **26**(2): p. 350-369.

59.   Harumi, K., *Scattering of plane waves by a rigid ribbon in a solid.* Journal of Applied Physics, 1961. **32**(6): p. 1488-1497.

60.   Harumi, K., *Scattering of plane waves by a cavity ribbon in a solid.* Journal of Applied Physics, 1962. **33**(12): p. 3588-3593.

61.   Chapman, R.K. and J.M. Coffey, *A theoretical model of ultrasonic examination of smooth flat cracks*, in *Review of Progress in Quantitative NDE*, D.O. Thompson and D.E. Chimenti, Editors. Vol. 3. 1984, Plenum: New York. p. 151-162.

62.   Achenbach, J.D., A.K. Gautesen, and H. Mcmaken, *Ray methods for waves in elastic solids*. 1982, Pitman Books Ltd: London.

63.   Mal, A.K., *Diffraction of elastic waves by a penny-shaped crack.* Quarterly Journal of Applied Mathematics, 1968. **26**: p. 231-238.

64.   Mal, A.K., *Interaction of elastic waves with a penny-shaped Crack.* International Journal of Engineering Science, 1970. **8**: p. 381-388.

65.   Mal, A.K., *Interaction of elastic waves with a Griffith crack.* International Journal of Engineering Science, 1970. **8**: p. 763–776.

66.   Sih, G.C., and Loeber, J.F., *Normal Compression and Radial Shear Waves Scattering at a Penny-Shaped Crack in an Elastic Solid.* Journal of The Acoustical Society of America, 1969. **46**(3B): p. 711-721.

67.   Loeber, J.F., and Sih, G.C., *Diffraction of Antiplane Shear Waves by a Finite Crack.* Journal of the Acoustical Society of America, July 1968. **44**(1): p. 90-98.

68. Pao, Y.-H. and V. Varatharajulu, *Huygens' principle, radiation conditions, and integral formulas for the scattering of elastic waves.* Journal of the Acoustical Society of America, 1976. **59**(6): p. 1361-1371.

69. Gubernatis, J.E., E. Domany, and J.A. Krumhansl, *Formal aspects of the theory of the scattering of ultrasound by flaws in elastic materials.* Journal of Applied Physics, 1977. **48**(7): p. 2804-2811.

70. Tan, T.H., *Reciprocity relations for scattering of plane, elastic waves.* Journal of the Acoustical Society of America, 1977. **61**(4): p. 928-931.

71. Tan, T.H., *Far-field radiation characteristics of elastic waves and the elastodynamic radiation condition.* Applied Scientific Research, 1975. **31**(5): p. 363 - 375.

72. Varatharajulu, V., *Reciprocity relations and forward amplitude theorems for elastic waves.* Journal of Mathematical Physics, 1977. **18**(4): p. 537-543.

73. Kino, G.S., *The application of reciprocity theory to scattering of acoustic waves by flaws.* Journal of Applied Physics, 1978. **49**(6): p. 3190-3199.

74. Auld, B.A., *General electromechanical reciprocity relations applied to the calculation of elastic wave scattering coefficients.* Wave Motion, 1979. **1**: p. 3-10.

75. Kino, G.S., and Khuri-Yakub, B.T., *Application of the Reciprocity theorem to Nondestructive evaluation.* Research in Nondestructive Evaluation, 1992. **4**: p. 193-204.

76. Achenbach, J.D., *Reciprocity in Elastodynamics.* 2003, Cambridge: Cambridge University Press.

77. Achenbach, J.D., *Reciprocity and related topics in elastodynamics.* Applied Mechanics Reviews, 2006. **59**: p. 13-32.

78. de Hoop, A.T., *Handbook of radiation and scattering of waves : acoustic waves in fluids, elastic waves in solids, electromagnetic waves.* 1995, London: Academic Press.

79. Pao, Y.-H., *Mathematical theories of the diffraction of elastic waves*, in *Proceedings of the first international symposium on ultrasonic materials characterization held at NBS, Gaithersburg, Md. , June 7-9, 1978 (National Bureau of Standards special publication 596, 'Ultrasonic materials*

characterization'), H. Berger and M. Linzer, Editors. 1980, National Bureau of Standards (USA).

80.   Zhang, C. and D. Gross, *On wave propagation in elastic solids with cracks*. International series on advances in fracture mechanics, ed. M.H. Aliabadi. 1998, Southampton: Computational Mechanics Publications.

81.   Krenk, S., and Schmidt, H., *Elastic wave scattering by a circular crack*. Philosophical Transactions of the Royal Society of London. Series A, Mathematical and Physical Sciences., 1982. **308**: p. 167-198.

82.   Datta, S., *Scattering of elastic waves*. Mechanics Today, 1978. **4**: p. 149–208.

83.   Datta, S.K., *Diffraction of SH waves by an edge crack*. Journal of Applied Mechanics, 1979. **46**: p. 101 - 106.

84.   Kundu, T., *Scattering of torsional waves by a circular crack in a transversely isotropic solid*. Journal of the Acoustical Society of America, 1990. **88**(4): p. 1975-1980.

85.   Bostrom, A., *Review of hypersingular integral equation method for crack scattering and application to modeling of ultrasonic nondestructive evaluation*. Applied Mechanics Reviews, 2003. **56**(4): p. 383-405.

86.   Lin, W., and Keer, L.M., *Scattering by a horizontal subsurface penny-shaped crack*. Proceedings of the Royal Society of London. Series A, Mathematical and Physical Sciences, 1986. **408**(1835): p. 277-294.

87.   Lewis, P.A., and Wickham, G.R., *The diffraction of SH waves by an arbitrary shaped crack in two dimensions*. Philosophical Transactions of the Royal Society of London. Series A, Mathematical and Physical Sciences., 1992. **340**(1659): p. 503-529.

88.   Lewis, P.A., Temple, J.A.G., Walker, E. J., and Wickham, G.R., *Calculation of diffraction coefficients for a semi-infinite crack embedded in an infinite anisotropic linearly elastic body*. Proceedings of the Royal Society of London. Series A, Mathematical and Physical Sciences, 1998. **454**: p. 1781-1803.

89.   Kraut, E.A., *Review of Theories of Scattering of Elastic Waves by Cracks*. IEEE Transactions on Sonics and Ultrasonics, 1976. **SU-23**(3): p. 162-167.

90.   Hackman, R.H., *Acoustic scattering from elastic solids*, in *Physical Acoustics*, A.D. Pierce and R.N. Thurston, Editors. Vol. XXII. 1993, Academic Press Inc: New York.

91.   Domany, E., Krumhansl, J.A., and Teitel, S., *Quasistatic approximation to the scattering of elastic waves by a circular crack*. Journal of Applied Physics, 1978. **49**(5): p. 2599-2604.

92.   Gubernatis, J.E., *et al.*, *The Born approximation in the theory of the scattering of elastic waves by flaws.* Journal of Applied Physics, 1977. **48**(7): p. 2812-2819.

93.   Gubernatis, J.E. and E. Domany, *Rayleigh scattering of elastic waves from cracks.* Journal of Applied Physics, 1979. **50**(2): p. 818 - 824.

94.   Gubernatis, J.E., *Long-wave approximations for the scattering of elastic waves from flaws with applications to ellipsoidal voids and inclusions.* Journal of Applied Physics, 1979. **50**(6): p. 4046-4058.

95.   Coussy, O., *Scattering of SH waves by a rigid elliptic fiber partially debonded from its surrounding matrix.* Mechanics Research and Communications, 1986. **13**(1): p. 39-45.

96.   Jain, D.L., and Kanwal, R.P., *The Born approximation for the scattering theory of elastic waves by two-dimensional flaws.* Journal of Applied Physics, 1982. **53**(6): p. 4208-4217.

97.   Eshelby, J.D., *The determination of the elastic field of an ellipsoidal inclusion, and related problems.* Proceedings of the Royal Society of London. Series A, Mathematical and Physical Sciences, 1957. **241**(1226): p. 376-396.

98.   Eshelby, J.D., *The elastic field outside an ellipsoidal inclusion.* Proceedings of the Royal Society of London. Series A, Mathematical and Physical Sciences, 1959. **252**(1271): p. 561-569.

99.   Tada, H., Paris, P., Irwin, G., *The stress analysis of cracks handbook.* 1973: Del Research Co., St. Louis.

100.   Rose, J.H., and Krumhansl, J.A., *Determination of flaw characteristics from ultrasonic scattering data.* Journal of Applied Physics, 1979. **50**(4): p. 2951-2952.

101.   Rose, J.H., *Elastic wave inverse scattering in nondestructive evaluation.* Pure and Applied Geophysics, 1989. **131**(4): p. 715 - 739.

102. Wu, R., and Aki, K., *Scattering characteristics of elastic waves by an elastic heterogeneity.* Geophysics, 1985. **50**(4): p. 582-595.

103. Yamada, M., *et al.*, *Three dimensional Born and Kirchhoff inversions for shape reconstruction of defects*, in *Review of Progress in Quantitative Nondestructive Evaluation*, D.O. Thompson and D.E. Chimenti, Editors. Vol. 22. 2003, American Institute of Physics: Melville, New York. p. 734-741.

104. Rose, J.H., and Richardson, J.M., *Time domain Born approximation.* Journal of Nondestructive Evaluation, 1982. **3**(1): p. 45-53.

105. Baik, J.M. and R.B. Thompson, *Ultrasonic scattering from imperfect interfaces : a quasi-static model.* Journal of Nondestructive Evaluation, 1984. **4**(3/4): p. 177-196.

106. Margetan, F.J., Thompson, R. B., and Gray, T. A., *Interfacial spring model for ultrasonic interactions with imperfect interfaces: Theory of oblique incidence and application to diffusion-bonded butt joints.* Journal of Nondestructive Evaluation, 1988. **7**(3-4): p. 131 - 152.

107. Karal Jr, F.C., and Keller, Joseph B., *Elastic wave propagation in homogeneous and inhomogeneous media.* Journal of the Acoustical Society of America, 1959. **31**(6): p. 694-705.

108. Keller, J.B., and Karal Jr, Frank C., *Geometrical theory of elastic surface-wave excitation and propagation.* Journal of the Acoustical Society of America, 1964. **36**(1): p. 32-40.

109. Brind, R.J., J.D. Achenbach, and J.E. Gubernatis, *High-frequency scattering of elastic waves from cylindrical cavities.* Wave Motion, 1984. **6**: p. 41-60.

110. Auld, B.A., Ayter, S., and Tan, M. *Theory of scattering of Rayleigh waves by surface breaking cracks*. in *IEEE Ultrasonics Symposium*. 1978.

111. Schmerr Jr, L.W., A. Sedov, and C.-P. Chiou, *A unified constrained inversion model for ultrasonic flaw sizing.* Research in Nondestructive Evaluation, 1989. **1**: p. 77-97.

112. Keller, J.B., *Geometrical Theory of Diffraction.* Journal of the Optical Society of America, 1962. **52**(2): p. 116-130.

113. Achenbach, J.D., *et al.*, *Diffraction of ultrasonic waves by penny-shaped cracks in metals : theory and experiment.* Journal of the Acoustical Society of America, 1979. **66**(6): p. 1848-1856.

114. Chapman, R.K., *Ultrasonic reflection from smooth flat cracks: Exact solution for the semi-infinite crack*, in *CEGB Report NW/SSD/RR/14/81*. 1981, N.D.T Applications Centre, Scientific Services Department, Central Electricity Board, U.K., North Western Region.

115. Schmerr Jr, L.W., Song, Sung-Jin., and Sedov, Alexander, *Ultrasonic flaw inverse sizing problems.* Inverse Problems, 2002. **18**: p. 1775-1793.

116. Podil'chuk, Y.N., Y.K. Rubtsov, and P.N. Soroka, *Geometrical theory of diffraction in the scattering of harmonic elastic waves by smooth convex cavities.* International Applied Mechanics, 1991. **27**(2): p. 131-140 (Translated from Prikladnaya Mekhanika, Vol. 27, No. 2, pp. 26–35, February, 1991).

117. Harker, A., *Numerical modelling of the scattering of elastic waves in plates.* Journal of Nondestructive Evaluation, 1984. **4**(2): p. 89-106.

118. Harumi, K., Okada, Hiaso., Saito, Tetsuo., and Fujimori, Toshiaki., *Numerical experiments of reflection of elastic waves by a crack or an elliptic cylinder.* IEEE Ultrasonics Symposium, 1982: p. 1064-1069.

119. Datta, S.K., Fortunko, C.M., and King, R.B., *Sizing of surface cracks in a plate using SH waves.* IEEE Ultrasonics Symposium, 1981: p. 863-867.

120. Datta, S.K., A.H. Shah, and C.M. Fortunko, *Diffraction of medium and long wavelength horizontally polarized shear waves by edge cracks.* Journal of Applied Physics, 1982. **53**(4): p. 2895 - 2903.

121. Abduljabbar, Z., S.K. Datta, and A.H. Shah, *Diffraction of horizontally polarized shear waves by normal edge cracks in a plate.* Journal of Applied Physics, 1983. **54**(2): p. 461 - 472.

122. Hackman, R.H., and Todoroff, Douglas G., *An application of the spheroidal-coordinate-based transition matrix: The acoustic scattering from high aspect ratio solids.* Journal of the Acoustical Society of America, 1985. **78**(3): p. 1058-1071.

123. Varatharajulu, V., and Pao, Yih-Hsing., *Scattering matrix for elastic waves. I. Theory.* Journal of the Acoustical Society of America, 1976. **60**(3): p. 556-566.

124. Visscher, W.M., *A new way to calculate scattering of acoustic and elastic waves I. Theory illustrated for scalar waves.* Journal of Applied Physics, 1980. **51**(2): p. 825-834.

125. Visscher, W.M., *A new way to calculate scattering of acoustic and elastic waves II. Applications to elastic waves scattered from voids and fixed rigid obstacles.* Journal of Applied Physics, 1980. **51**(2): p. 835-845.

126. Harumi, K., and Uchida, M., *Computer simulation of ultrasonics and its applications.* Journal of Nondestructive Evaluation, 1990. **9**(2/3): p. 81-99.

127. Grahn, T., *Lamb wave scattering from a circular partly through-thickness hole in a plate.* Wave Motion, 2003. **37**: p. 63 - 80.

128. Castaings, M., E. Le Clezio, and B. Hosten, *Modal decomposition method for modeling the interaction of Lamb waves with cracks.* Journal of the Acoustical Society of America, 2002. **112**(6): p. 2567-2582.

129. Wang, X.-M., C.F. Ying, and M.-X. Li, *Scattering of antiplane shear waves by a circular cylinder in a traction-free plate.* Journal of the Acoustical Society of America, 2000. **108**(3): p. 913-923.

130. Wang, X. and C.F. Ying, *Scattering of Lamb waves by a circular cylinder.* Journal of the Acoustical Society of America, 2001. **110**(4): p. 1752 - 1763.

131. Tan, M. and B. Auld, *Normal mode variational method for two - and three-dimensional.* IEE Ultrasonics Symposium, 1980: p. 857-861.

132. Fortunko, C.M., *Ultrasonic detection and sizing of two-dimensional defects at long wavelengths.* Applied Physics Letters, 1981. **38**(12): p. 980-982.

133. Fortunko, C.M., R.B. King, and M. Tan, *Nondestructive evaluation of planar defects in plates using low-frequency sheer horizontal waves.* Journal of Applied Physics, 1982. **53**(5): p. 3450 - 3458.

134. King, R.B. and C.M. Fortunko, *Extended variational solution for scattering from flaws in plates.* Journal of Applied Physics, 1982. **53**(5): p. 3459 - 3460.

135. Ditri, J.J., *Utilization of guided elastic waves for the characterization of circumferential cracks in hollow cylinders.* Journal of the Acoustical Society of America, 1994. **96**(6): p. 3769-3775.

136. Tien, J.J.W., Khuri-Yakub, B. T., Kino, G. S. , Marshall, D. B., and Evans, A. G., *Surface acoustic wave measurements of surface cracks in ceramics.* Journal of Nondestructive Evaluation, 1981. **2**(3-4): p. 219 - 229.

137. Rokhlin, S., *Diffraction of Lamb waves by a finite crack in an elastic layer.* Journal of the Acoustical Society of America, 1980. **67**(4): p. 1157-1165.

138. Norris, A.N. and C. Vemula, *Scattering of flexural waves on thin plates.* Journal of Sound and Vibration, 1995. **181**(1): p. 115-125.

139. Vemula, C. and A.N. Norris, *Flexural wave propagation and scattering on thin plates using Mindlin theory.* Wave Motion, 1997. **26**: p. 1-12.

140. Andronov, I.V., and Belinskii, B.P., *Scattering of a flexural wave by a finite straight crack in an finite straight crack in an elastic plate.* Journal of Sound and Vibration, 1995. **180**(1): p. 1-16.

141. Mckeon, J.C.P., and Hinders, M. K., *Lamb wave scattering from a through hole.* Journal of Sound and Vibration, 1999. **224**(5): p. 843 - 862.

142. Fromme, P., and Sayir, Mahir B., *Measurement of the scattering of a Lamb wave by a through hole in plate.* Journal of the Acoustical Society of America, 2002. **111**(3): p. 1165-1170.

143. Wang, C.H. and F.-K. Chang, *Scattering of plate waves by a cylindrical inhomogeneity.* Journal of Sound and Vibration, 2005. **282**: p. 429-451.

144. Rose, L.R.F., and Wang, C.H., *Mindlin plate theory for damage detection: Source solutions.* Journal of the Acoustical Society of America, 2004. **116**(1): p. 154-171.

145. Alleyne, D.N. and P. Cawley, *The quantitative measurement of Lamb wave interaction with defects*, in *Ultrasonics International.* 1991. p. 491-494.

146. Alleyne, D.N. and P. Cawley, *The interaction of Lamb waves with defects.* IEEE Transactions on Ultrasonics, Ferroelectrics and Frequency control, 1992. **39**(3): p. 381-397.

147. Rose, J.L., *A Baseline and vision of ultrasonic guided wave inspection potential.* Journal of Pressure Vessel Technology, 2002. **124**: p. 273 - 282.

148. Huang, R., *et al*., *Kirchhoff Approximation Revisited - Some New Results for Scattering in Isotropic and Anisotropic Elastic Solids.* Research in Nondestructive Evaluation, 2006. **17**(3): p. 137-160.

149. *ABAQUS v6.6 Analysis User's Manual*. 2005: http://www.simulia.com/.

150. Pavlakovic, B., *et al*., *Simulation of lamb wave propagation using pure mode excitation*, in *Review of Progress in Quantitative NDE*, D.O. Thompson and D.E. Chimenti, Editors. Vol. 17. 1998, Plenum: New York. p. 1003 - 1010.

151. Alleyne, D. and P. Cawley, *A two-dimensional Fourier transform method for the measurement of propagating multimode signals.* Journal of the Acoustical Society of America, 1991. **89**(3): p. 1159-1168.

152. Hitchings, D., *FE77 User Manual*, in *Technical report, Imperial College*. 1994: London, U.K.

153. Lowe, M., *Characteristics of the reflection of lamb waves from defects in plates and pipes*, in *Review of Progress in Quantitative NDE*, D.O. Thompson and D.E. Chimenti, Editors. Vol. 17A. 1998, Plenum: New York. p. 113 - 120.

154. Song, W., *et al*., *Ultrasonic guided wave scattering in a plate overlap.* IEEE Transactions on Ultrasonics, Ferroelectrics and Frequency control, 2005. **52**(5): p. 892-903.

155. Davies, J. and P. Cawley, *The application of synthetically focused imaging techniques for high resolution guided wave pipe inspection*, in *Review of Progress in Quantitative NDE*, D.O. Thompson and D.E. Chimenti, Editors. Vol. 26. 2007, American Institute of Physics: Melville, New York. p. 681-688.

156. Achenbach, J.D. and A.K. Gautesen, *Geometrical theory of diffraction for three-D elastodynamics.* Journal of the Acoustical Society of America, 1977. **61**(2): p. 413 - 421.

157. Datta, S.K., *Diffraction of plane elastic waves by ellipsoidal inclusions.* Journal of the Acoustical Society of America, 1977. **61**(6): p. 1432 - 1437.

158. Paffenholz, J., *et al.*, *Experimental and theoretical study of Rayleigh-Lamb waves in a plate containing a surface-breaking crack.* Research in Nondestructive Evaluation, 1990. **1**: p. 197-217.

159. Liu, S.W. and S.K. Datta, *Scattering of ultrasonic wave by cracks in a plate.* Journal of Applied Mechanics, 1993. **60**: p. 352-357.

160. Wang, X.-M. and C.F. Ying, *Scattering of Lamb waves by a circular cylinder.* Journal of the Acoustical Society of America, 2001. **110**(4): p. 1752-1763.

161. Cho, Y. and J.L. Rose, *An elastodynamic hybrid boundary element study for elastic guided wave interactions with a surface breaking defect.* International Journal for Solids and Structures, 2000. **37**: p. 4103 - 4124.

162. Cho, Y., D.D. Hongerholt, and J.L. Rose, *Lamb wave scattering analysis for reflector characterization.* IEEE Transactions on Ultrasonics, Ferroelectrics and Frequency control, 1997. **44**(1): p. 44-52.

163. Ditri, J.J., *Phase and energy velocities of cylindrically crested guided waves.* Journal of the Acoustical Society of America, 1995. **97**(1): p. 98-107.

164. Kinra, V.K. and B.Q. Vu, *Diffraction of Rayleigh waves in a half-space. I. Normal edge crack.* Journal of the Acoustical Society of America, 1985. **77**(4): p. 1425-1430.

165. Kinra, V.K. and B.Q. Vu, *Diffraction of Rayleigh waves in a half-space. II. Inclined edge crack.* Journal of the Acoustical Society of America, 1986. **118**(6): p. 3585-3594.

166. Masserey, B. and E. Mazza, *Analysis of the near-field ultrasonic scattering at a surface crack.* Journal of the Acoustical Society of America, 2005. **118**(6): p. 3585-3594.

167. Norris, A.N. and Z. Wang, *Bending-wave diffraction from strips and cracks on thin plates.* Quarterly Journal of Mechanics and Applied Mathematics, 1994. **47**(4): p. 607-628.

168. Wilcox, P., *Modeling the Excitation of Lamb and SH waves by point and line sources*, in *Review of Progress in Quantitative NDE*, D.O. Thompson and D.E. Chimenti, Editors. Vol. 23. 2004, American Institute of Physics: Melville, New York. p. 206-213.

169.   Drozdz, M., *et al.*, *Modeling bulk and guided wave propagation in unbounded elastic media using absorbing layers in commercial FE packages*, in *Review of Progress in Quantitative NDE*, D.O. Thompson and D.E. Chimenti, Editors. Vol. 26. 2007, American Institute of Physics: Melville, New York. p. 87-94.

170.   Castaings, M. and C. Bacon, *Finite element modeling of torsional wave modes along pipes with absorbing materials.* Journal of the Acoustical Society of America, 2006. **119**(6): p. 3741–3751.

171.   Castaings, M., *et al.*, *Finite element predictions for the dynamic response of thermo-viscoelastic material structures.* Journal of the Acoustical Society of America, 2004. **115**(3): p. 1125-1133.

172.   Demma, A., P. Cawley, and M. Lowe, *Scattering of the fundamental shear horizontal mode from steps and notches in plates.* Journal of the Acoustical Society of America, 2003. **113**(4): p. 1880-1891.

173.   Vogt, T., M. Lowe, and P. Cawley, *Measurement of the material properties of viscous liquids using ultrasonic guided waves.* IEEE Transactions on Ultrasonics, Ferroelectrics and Frequency control, 2004. **51**(6): p. 737-747.

174.   Chapman, R.K., *A system model for the ultrasonic inspection of smooth planar cracks.* Journal of Nondestructive Evaluation, 1990. **9**(2): p. 197-210.

175.   Scruby, C.B., K.R. Jones, and L. Antoniazzi, *Diffraction of elastic waves by defects in plates: Calculated arrival strengths for point force and thermoelastic sources of ultrasound.* Journal of Nondestructive Evaluation, 1986. **5**(3-4): p. 145 - 156.

176.   Ogilvy, J.A. and J.A.G. Temple, *Diffraction of elastic wave by cracks: Application to time-of-flight inspection.* Ultrasonics, 1983. **21**(6): p. 259-269.

177.   Ravenscroft, F.A., K. Newton, and C.B. Scruby, *Diffraction of ultrasound by cracks: comparison of experiment with theory.* Ultrasonics, 1991. **29**: p. 29-37.

178.   Baskaran, G., Balasubramaniam, K., Krishnamurthy, CV., Lakshmana Rao, C., *Ray based model for the ultrasonic time-of-flight diffraction simulation of thin walled structure inspection.* ASME Journal of Pressure Vessel Technology, 2005. **127**: p. 262-268.

179.   Oliner, A.A., *Waveguides for acoustic surface waves: A review.* Proceedings of the IEEE, 1976. **64**(5): p. 615-627.

180.   Lagasse, P.E., I.M. Mason, and E.A. Ash, *Acoustic Surface Waveguides - Analysis and Assessment.* IEEE Transactions on Microwave Theory and Techniques, 1973. **21**(4): p. 225-236.

181.   Sinha, B.K., *Some remarks on propagation characteristics of ridge guides for acoustic surface waves at low frequencies.* Journal of the Acoustical Society of America, 1974. **56**(1): p. 16-18.

182.   Danilov, V.N., *Scattering of transverse waves by strip-shaped cracks.* Russian Journal of Nondestructive Testing, 2002. **38**(8): p. 582-592 (Translated from Defektoskopiya, No. 8, 2002, pp. 31-43).

183.   Caleap, M., C. Aristégui, and Y.C. Angel, *Further results for antiplane scattering by a thin strip.* Journal of the Acoustical Society of America, 2007. **122**(4): p. 1876-1879.

184.   Velichko, A. and P.D. Wilcox, *Excitation and scattering of guided waves – relationships between solutions for plates and pipes*, in *Review of Progress in Quantitative NDE*, D.O. Thompson and D.E. Chimenti, Editors. Vol. 27, in press. 2008, American Institute of Physics: Melville, New York.

List of publications arising from this thesis

1.	Rajagopal, P. and M.J.S. Lowe, *Interaction of the fundamental shear horizontal mode with a through thickness crack in an isotropic plate*, in *Review of Progress in Quantitative NDE*, D.O. Thompson and D.E. Chimenti, Editors. Vol. 25. 2006, American Institute of Physics: Melville, New York. p. 157-164.

2.	Rajagopal, P. and M.J.S. Lowe, *Scattering of the fundamental shear horizontal guided wave mode incident at an arbitrary angle on finite slits in an isotropic plate*, in *Review of Progress in Quantitative NDE*, D.O. Thompson and D.E. Chimenti, Editors. Vol. 26. 2007, American Institute of Physics: Melville, New York. p. 47-54.

3.	Rajagopal, P. and M.J.S. Lowe, *Short range scattering of the fundamental shear horizontal guided wave mode normally incident at a through-thickness crack in an isotropic plate.* Journal of the Acoustical Society of America, 2007. **122**(3): p. 1527-1538.

4.	Rajagopal, P. and M.J.S. Lowe, *Scattering of the fundamental shear horizontal mode incident at an oblique angle on a through-thickness crack in an isotropic plate.* Journal of the Acoustical Society of America, 2007. **submitted for publication**.

5.	Rajagopal, P. and M.J.S. Lowe, *Scattering of the fundamental shear horizontal mode by part-thickness surface-breaking cracks in an isotropic plate*, in *Review of Progress in Quantitative NDE*, D.O. Thompson and D.E. Chimenti, Editors. Vol. 27, in press. 2008, American Institute of Physics: Melville, New York.

6.	Rajagopal, P. and M.J.S. Lowe, *Scattering of the fundamental shear horizontal mode by part-thickness cracks in an isotropic plate.* Journal of the Acoustical Society of America, 2007. **submitted for publication**.